# Fast control and decoherence in superconducting quantum circuits

by

Chunqing Deng

A thesis
presented to the University of Waterloo
in fulfillment of the
thesis requirement for the degree of
Doctor of Philosophy
in
Physics

Waterloo, Ontario, Canada, 2015

© Chunqing Deng 2015

This thesis consists of material all of which I authored or co-authored: see Statement of Contributions included in the thesis. This is a true copy of the thesis, including any required final revisions, as accepted by my examiners.

I understand that my thesis may be made electronically available to the public.

## Statement of Contributions

Most of the material in Chapter 5 is submitted to be considered for publication in the following:

**Reference:** Chunqing Deng, Jean-Luc Orgiazzi, Feiruo Shen, Sahel Ashhab, and Adrian Lupascu, Observation of Floquet states in a strongly driven artificial atom, submitted to Phys. Rev. Lett.

**Contributions:** I conducted the experiments. FS and I worked on the analysis of the experimental data and the comparison of experiments with numerical simulations. JLO fabricated the device. SA worked on the theoretical analysis of the results. AL supervised the experimental work.

Most of the material in Chapter 7 is published in the following:

**Reference:** Chunqing Deng, Martin Otto, and Adrian Lupascu, An analysis method for transmission measurements of superconducting resonators with applications to quantum-regime dielectric-loss measurements, J. Appl. Phys. 114, 054504 (2013).

Chunqing Deng, Martin Otto, and Adrian Lupascu, Characterization of low-temperature microwave loss of thin aluminum oxide formed by plasma oxidation, Appl. Phys. Lett. 104, 043506 (2014).

**Contributions:** I conducted the experiments. MO and I fabricated the devices. AL and I worked on the analytical method for the transmission measurements of resonators. AL supervised the theoretical and experimental work.

## Abstract

This thesis discusses a series of experimental and theoretical studies on fast control and decoherence in superconducting quantum circuits. These two subjects are complementary aspects of the problem of improving the gate fidelities in quantum information processing devices based on superconducting circuits.

In the first part of this thesis, we present experiments on fast control of a superconducting flux qubit using strong driving. We explore driving with short pulses and a driving strength significantly exceeding the transition frequency. The observed dynamics is described in terms of quasienergies and quasienergy states, in agreement with Floquet theory. We observe the role of pulse shaping in the dynamics, as determined by non-adiabatic transitions between Floquet states. In addition, based on adiabatic perturbation theory in the Floquet picture, we propose a control scheme for fast and high-fidelity single-qubit operations with strong driving. These results pave the way to quantum control with a fidelity beyond the threshold of fault-tolerant quantum computation.

In the second part of this thesis, we discuss experimental methods and present the characterization of decoherence in superconducting resonators and superconducting qubits. Firstly, we present an analysis method on the measurements of photon loss in superconducting resonators. We use this method to characterize the microwave loss of aluminum oxide, an important material in superconducting circuits. The power and temperature dependence of the measured loss is consistent with loss due to two-level defects in amorphous materials. Secondly, we present experimental results on decoherence and noise spectroscopy of a superconducting flux qubit. Using the qubit as a noise spectrometer, we perform detailed measurements on the power spectral density of the flux noise in superconducting circuits over a wide range of frequencies, from $10^{-3}$ to $10^{8}$ Hz, and over a temperature range from 35 to 130 mK. We also present measurements of frequency and temperature dependence of the qubit energy relaxation.

**Acknowledgements**

First, I would like to thank my supervisor Adrian Lupascu for giving me the opportunity to work in the exciting field of superconducting quantum computing. From long nights working in the lab to intensive discussions in front of a white board, he has taught me all the essential qualities needed to become a scientist. His passion and dedication to research always surprise and encourage me.

Then, I want to thank all members of the SQD group for the hard works that makes difficult experiments possible. I am extremely grateful to Jean-Luc Orgiazzi who had contributed to almost all the major setup in the lab. I really enjoy the time working with Feiruo Shen who can always come up with great ideas. With Marty Otto, our collaborated work had been always very fruitful thanks to his persistence and patience in both the lab and the cleanroom.

I feel extremely lucky for having been working with a number of amazing senior researchers in IQC. Among them, I want to thank Jay Gambetta who taught me quantum theories in my early years here. I am grateful to Mustafal Bal who shared me his magic in microfabrication. I also thank Florian Ong who taught me the essence of low-temperature experiments. In addition, I want to thank Sahel Ashhab from Qatar Foundation, who has been consistently providing us timely help in understanding the data in experiments.

From the University of Waterloo, I am grateful to all the technical staffs who provided supports to various experiments throughout my PhD. My special thanks goes to Brian Goddard, Rodello Salandanan, Nathan Nelson-Fitzpatrick and Vito Logiudice in the Quantum NanoFab Facility for their helps on the device fabrication. I also want to express my gratitude to Zhenwen Wang and Harmen Vander Heide in the Science Technical Services for their helps with electronics and machining.

In the end, I would like to express my appreciation to Marty Otto and Sahel Ashhab again for their useful comments on this thesis.

## Dedication

I dedicate this work to my beloved wife Qin Feng whose unconditional encouragement and support made it possible.

# Table of Contents

**List of Tables** xi

**List of Figures** xii

**1 Introduction** 1

1.1 Quantum computing with superconducting devices . . . . . 2

1.2 Outline of the thesis . . . . . 3

**2 Theoretical base and experimental setup** 5

2.1 Josephson junctions . . . . . 5

2.1.1 The Josephson effect . . . . . 5

2.1.2 Quantization of a Josephson junction . . . . . 7

2.2 Superconducting flux qubits . . . . . 8

2.3 Superconducting resonators . . . . . 11

2.3.1 Lumped-element resonators . . . . . 12

2.3.2 Transmission-line resonators . . . . . 13

2.4 Flux qubits in circuit quantum electrodynamics . . . . . 16

2.4.1 Energy level spectrum . . . . . 19

2.4.2 Dispersive regime . . . . . 20

2.5 Experimental setup . . . . . 20

2.5.1 Cryogenic setup . . . . . 20

2.5.2 Magnetic field shielding . . . 23
2.5.3 Pulse synthesis, demodulation and DC bias . . . 23

**3 Driven evolution of a qubit 26**
3.1 Rotating frame and rotating wave approximation . . . 26
3.1.1 Rotating frame transformation . . . 27
3.1.2 Rotating wave approximation . . . 28
3.2 Floquet theory . . . 30
3.3 Quasienergies and Floquet states of a harmonically driven qubit . . . 31

**4 Decoherence and noise characterization methods 36**
4.1 Theoretical description of decoherence . . . 36
4.1.1 Born-Markov master equation . . . 37
4.1.2 Non-Markovian processes . . . 42
4.2 Characterization methods for decoherence of a qubit . . . 43
4.2.1 Energy relaxation: $T_1$ . . . 44
4.2.2 Ramsey experiment: $T_2$ . . . 45
4.2.3 Noise spectroscopy with dynamical decoupling . . . 46
4.3 Decoherence of resonators . . . 48

**I Fast control of a superconducting qubit with strong driving 52**

**5 Observation of Floquet states in a strongly driven superconducting qubit 53**
5.1 Experimental platform . . . 54
5.2 Rabi oscillations in strong driving regime: a measurement of quasienergies 56
5.3 Quantum state tomography for Floquet dynamics . . . 59
5.4 Turn-on/-off effects of the pules . . . 59
5.5 Fast quantum operations . . . 63
5.6 Conclusions . . . 63

**6 Optimization of single-qubit operations in the strong driving regime 64**
6.1 Adiabatic perturbation theory in the Floquet picture . . . . . 65
6.2 Nonadiabatic transitions between Floquet states in a pulse-driven qubit . . 68
6.3 Optimized pulses for single-qubit operations . . . . . 76
6.3.1 Quantum process characterization . . . . . 76
6.3.2 Simulations of strong driving gates . . . . . 77
6.4 Conclusion . . . . . 80

**II Decoherence in superconducting resonators and superconducting qubits 81**

**7 Decoherence in superconducting resonators 82**
7.1 An analysis method for transmission measurements of superconducting resonators . . . . . 83
7.1.1 Derivation of resonator transmission . . . . . 85
7.1.2 Voltage on lumped element capacitor . . . . . 92
7.1.3 Explanation of asymmetric transmission . . . . . 95
7.1.4 Generalization to other resonance circuits . . . . . 100
7.1.5 Summary . . . . . 103
7.2 Characterization of microwave loss of thin aluminum oxide formed by plasma oxidation using superconducting resonators . . . . . 104
7.2.1 Experimental methods . . . . . 106
7.2.2 Power dependence of dielectric loss . . . . . 107
7.2.3 Temperature dependence of dielectric loss . . . . . 108
7.2.4 Summary . . . . . 110

**8 Decoherence and noise spectroscopy in superconducting flux qubits 111**
8.1 Experimental parameters and methods . . . . . 112
8.1.1 Characterizations of qubit parameters . . . . . 112

8.1.2 Thermal photons in the resonator and shot noise . . . . . 114
8.1.3 Noise spectroscopy through dynamical decoupling . . . . . 118
8.1.4 Low-frequency noise spectroscopy through Ramsey sampling . . . . 119
8.2 Low-to-intermediate-frequency noise spectroscopy . . . . . 124
8.2.1 Noise spectroscopy at 35 mK . . . . . 124
8.2.2 Temperature dependence of the $\epsilon$ flux noise . . . . . 127
8.3 Qubit energy relaxation: a probe of high-frequency effective noise . . . . . 128
8.3.1 Energy relaxation at different operation points . . . . . 130
8.3.2 Temperature dependence of the energy relaxation . . . . . 131
8.4 Summary . . . . . 132

**APPENDICES** **134**

**A Fabrication of qubit devices** **135**

**B Pulse calibration for quantum state tomography** **136**

**C Quantum state preparation with strong pulse** **137**

**D Choice of quasienergies and quasienergy states** **139**

**E Notations and approximations used the Closest Pole and Zero Method** **140**

**F Statistical-sampling noise in the Ramsey sampling measurements** **144**

**References** **146**

# List of Tables

7.1 Circuit parameters of the LC resonator . . . . . 88
7.2 Reduced parameters of the LC resonator . . . . . 88
7.3 Measurement results of resonators at 54 mK . . . . . 108

# List of Figures


2.1 Schematic diagram of Josephson junction . . . . . 6
2.2 Energy levels and the potential of a Josephson junction . . . . . 8
2.3 Schematic diagram of the flux qubit . . . . . 9
2.4 Potential energy of the flux qubit . . . . . 10
2.5 Energy level structure of the flux qubit . . . . . 12
2.6 Transmission line resonator and its schematic circuit model . . . . . 14
2.7 Schematic layout of circuit QED using a superconducting flux qubit . . . . 17
2.8 Energy level structure of the flux qubit in circuit QED . . . . . 19
2.9 Schematic diagram of the wiring setup . . . . . 21
2.10 Photograph of sample PCB and bottom part of the sample box . . . . . 23
2.11 Schematic of the room temperature control electronics . . . . . 24

3.1 Bloch sphere representations of qubit evolution with weak and strong driving 29
3.2 Quasienergies of a harmonically driven qubit . . . . . 35

4.1 Pulse sequences for decoherence measurement and noise spectroscopy . . . 44
4.2 Filter functions of the CP pulse sequence . . . . . 47
4.3 Transmission measurements of a resonator . . . . . 49

5.1 Qubit control, readout, and spectroscopy . . . . . 55
5.2 Coherent oscillations versus driving amplitude . . . . . 57
5.3 Oscillation frequencies of the qubit population versus driving amplitude . . 58

5.4 Quantum state tomography of the time-resolved Floquet state dynamics . 60
5.5 Coherent oscillations versus the pulse turn-on and turn-off times . . . . . 61
5.6 (Non)adiabaticity in the Floquet picture . . . . . 62

6.1 Nonadiabatic transitions between Floquet states during the rising edge . . 71
6.2 Verification of adiabatic perturbation theory during the rising edge . . . . 73
6.3 Nonadiabatic transitions between Floquet states during the falling edge . . 74
6.4 Verification of adiabatic perturbation theory during the falling edge . . . . 75
6.5 Gate fidelity of optimized pulses for $R_x(\theta)$ and $R_y(\theta)$ . . . . . 79

7.1 Image of an LC resonator device and its circuit model . . . . . 86
7.2 Equivalent circuit of a resonator coupled to a transmission line . . . . . 87
7.3 Exact and reduced $S_{21}$ of a resonator . . . . . 89
7.4 Exact and reduced $V/V_{\text{in}}^{+}$ of a resonator . . . . . 93
7.5 Experimentally measured loss dependence on $V_{\text{in}}^{+}$ and on $V$ . . . . . 94
7.6 Measured transmission curves with different types of asymmetries . . . . . 96
7.7 Circuit model of a LC resonator coupled to a non-ideal transmission line . 97
7.8 Asymmetric resonance due to reflections in the transmission line . . . . . 99
7.9 Asymmetric and symmetric response functions . . . . . 102
7.10 Optical microscope images and circuit schematics of overlap-capacitor resonators . . . . . 105
7.11 Loss tangent versus voltage on capacitor . . . . . 107
7.12 Temperature dependent of dielectric loss and frequency shift of a resonator 109

8.1 Qubit pictures, spectroscopy, and readout histogram . . . . . 113
8.2 Energy relaxation and dephasing rates around symmetry point . . . . . 115
8.3 Measurement of thermal photons in the resonator . . . . . 116
8.4 Coherence decay with a CPMG pulse sequence and the calculated noise spectrum . . . . . 118

8.5 Ensemble-averaged scheme of Ramsey sampling . . . . . 121
8.6 Single-shot scheme of Ramsey sampling . . . . . 125
8.7 A summary of the $\Delta$ and $\epsilon$ noise at 35 mK . . . . . 126
8.8 Temperature dependence of the $\epsilon$ flux noise . . . . . 129
8.9 Energy relaxation, Purcell effect, and effective high-frequency noise . . . . 130
8.10 Temperature dependence of the energy relaxation . . . . . 131

# Chapter 1

# Introduction

Transistors are arguably the most important invention in the 20th century as they form the physical base of logic gates and memories in a modern computer. In the past few decades, smaller and smaller transistors have been developed in an effort to make computers more powerful and smaller in size. However, transistors cannot be made infinitely small. As they approach the size of an atom, the macroscopic laws describing their design and principle of operation begin to break down. As the semiconductor industry is advancing the size of transistors towards this ultimate limit, a natural question arises: how can one make faster computers when transistors cannot be made any smaller?

Building a quantum computer is one of the answers to the above question. A quantum computer is different from a digital computer based on transistors. Instead of using classical bits with deterministic classical states, commonly labeled as 0 and 1, to store and process information, a quantum computer employs quantum bits or qubits which can be in a superposition of quantum states $|0\rangle$ and $|1\rangle$. The quantum nature of information gives a quantum computer unique advantages over its classical counterpart in applications such as quantum system simulation[1, 2], integer prime factorization[3], and database searching[4]. However, manipulating and preserving quantum information is extremely difficult. Unlike controlling a classical bit which involves only the bit-flip operation, the universal control of a quantum bit requires operations to prepare the qubit in an arbitrary superposition of states with high accuracy. In addition, due to the decoherence effect, where a quantum state lose its quantumness through interactions with its environment, qubits normally have a short lifetime and require extra effort to protect their states. In the past two decades, enormous efforts have been invested into the two above problems by means of various quantum system which could serve as qubits. This thesis focuses on the implementation of qubit control and the studies of decoherence in superconducting quantum devices.

## 1.1 Quantum computing with superconducting devices

Building a quantum computer is extremely challenging as a physical qubit has a set of very strong criteria to fulfill [5, 6]. To date, many quantum systems, including optical photons, trapped atoms, nuclear and electron spins, quantum dots, and superconducting circuits [6], have been developed as potential qubit candidates. Unlike most of the other implementations which employ microscopic systems, superconducting circuits are unique in that they are macroscopic in size with generic quantum properties.

The reason why superconductors enable quantum mechanical phenomena to be observed at the macroscopic level is explained by the theory of Bardeen, Cooper and Schrieffer [7, 8]. In a superconductor, all of the Cooper pairs of electrons are condensed into a single macroscopic state described by a wavefunction known as the superconducting ground state. In circuits involving coherent tunneling of Cooper pairs between superconductors, the center-of-mass motion of all the Cooper pairs in the system can be seen as a superposition of the superconducting ground states. Such macroscopic quantum states have been observed as quantized flux [9] and charge [10] states in experiments, and they can thereby be used as states for quantum information processing.

Qubits based on macroscopic superconducting states have a huge advantage over other quantum systems. Since each individual state corresponds to the behavior of millions of electrons, strong interactions between qubits and electromagnetic fields [11, 12, 13] can be achieved. This property opens new possibilities to demonstrate atomic physics and quantum optics on a chip [14], and it also allows for fast and high-fidelity quantum operations on superconducting qubits [15].

However, using macroscopic quantum states usually comes with the price of relatively short coherence times, as these states inevitably couple to more random processes in the environment. In the past decade, enormous efforts in decoupling superconducting qubits from the decoherence sources, including the improvement of the qubit design, the engineering of the microwave environment, and the introduction of new materials, have led to an increase of the coherence times by five orders of magnitude [15].

Despite the fast progress in the control and preservation of coherence in superconducting quantum circuits, a large scale quantum computer capable of running complicated algorithms remains a significant scientific and engineering challenge. At this level of complexity, error-correction codes [16] must be implemented to protect the coherence of the whole system. The key figure of merit for the implementation of quantum error-correction is the fidelity of the quantum gates. As the gate fidelities are ultimately limited by the number of operations that can be performed within the coherence time, it is equally im-

portant to keep improving the speed of the quantum gates and at the same time reducing the decoherence of each individual qubit.

## 1.2 Outline of the thesis

This thesis focuses on experimental and theoretical studies on fast control and decoherence in a superconducting qubit. These two subjects are complementary aspects of the problem of improving the gate fidelities in superconducting circuits. In this thesis, we explore experimentally fast control of a superconducting qubit using strong driving. The dynamics of the qubit is analyzed in the framework of the Floquet theory. Based on the adiabatic perturbation theory in the Floquet picture, we propose a control scheme for fast and high-fidelity quantum operations on a single qubit. We also present experimental methods and characterizations of decoherence of superconducting resonators and superconducting qubits. These studies are useful in understanding the fundamental physical processes related to the superconducting environment and in developing future designs of high-coherence superconducting qubits. This thesis is structured as follows:

In Chapter 2, we introduce Josephson junctions, superconducting flux qubits, and circuit quantum electrodynamics systems, which are the basic building blocks of a superconducting quantum processor. We also introduce the main details of the setup used in the experiments covered in this thesis. In Chapter 3, we introduce theoretical methods to used to analyze the evolution of a qubit under periodic driving for quantum control. In Chapter 4, we discuss the theoretical basis for describing quantum decoherence in qubits and resonators.

In Chapter 5, we present experiments on the driven dynamics of a superconducting flux qubit. We reach a driving strength significantly exceeding the transition frequency of the qubit. The observed dynamics is described in terms of quasienergies and quasienergy states, in agreement with Floquet theory. In addition, we observe the role of pulse shaping in the dynamics, as determined by non-adiabatic transitions between Floquet states, and we implement subnanosecond single-qubit operations.

In Chapter 6, we discuss the adiabatic perturbation theory in the Floquet picture and its application to a strongly-driven qubit. Based on the nonadiabatic transitions between Floquet states, we propose a driving scheme to implement fast and high-fidelity single-qubit operations.

In Chapter 7, we present a new method and experiments on the measurements of photon loss in superconducting resonators. The photon loss of the superconducting resonator is

related to the decoherence of the qubit via Purcell effect and photon fluctuations in a circuit QED system. We also present characterization of the microwave loss of aluminum oxide which is an important material in superconducting circuits and very relevant to the decoherence of superconducting qubits.

In Chapter 8, we present experimental results on decoherence and noise spectroscopy of a superconducting flux qubit. Using the qubit as a noise spectrometer, we study the low-to-intermediate-frequency noise which is responsible for dephasing processes. We perform detailed measurements on the power spectral density of the flux noise in superconducting circuits over a wide range of frequencies at various temperatures. We also measure frequency and temperature dependence of the qubit energy relaxation.

# Chapter 2

# Theoretical base and experimental setup

In this chapter, we will introduce the theoretical background and the setup used in the experiments covered in this thesis. In the first three sections, we will introduce the fundamental building blocks of a superconducting quantum information processor, including Josephson junctions, superconducting qubits, and superconducting resonators. In the fourth section, we will introduce a flexible implementation for quantum computing with superconducting circuits, namely circuit quantum electrodynamics. In the last section, we will introduce the experimental setup for the work in this thesis.

## 2.1 Josephson junctions

### 2.1.1 The Josephson effect

The basic element required to build superconducting quantum devices with applications in quantum information is the Josephson junction. A Josephson junction consists of two superconductors coupled by a weak link. The weak link can consist of a thin insulating barrier known as a superconductor-insulator-superconductor junction, or S-I-S junction. In 1962, Brian Josephson predicted that coherent tunneling of Cooper pairs can occur between the two superconductors without inducing any dissipation [17]. According to the BCS theory [7, 8], all the Cooper pairs in a superconductor can be described by a wave function, $\Psi = |A|e^{i\varphi}$ with $|A|$ an amplitude and $\varphi$ the superconducting phase. With $\varphi_{1,2}$

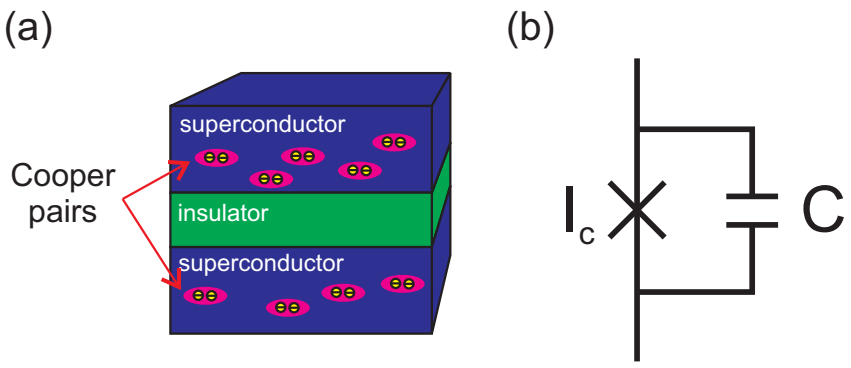



Figure 2.1: **Schematic diagram of Josephson junction.** (a) Physical structure of a Josephson junction. It contains two superconductors separated by a thin insulator layer. (b) Realistic circuit model for a Josephson junction.

the phases of the superconductors forming the junction (see Figure 2.1(a)), the current and voltage between the two superconductors can be related to their phase difference $\varphi = \varphi_1 - \varphi_2$ by the Josephson relations:

$$I = I_c \sin \varphi, \tag{2.1}$$

$$V = \frac{\Phi_0}{2\pi} \frac{d\varphi}{dt}, \tag{2.2}$$

where $I_c$ is the maximum superconducting current that the junction can support, known as the critical current, and $\Phi_0 \equiv \frac{h}{2e}$ is the superconducting flux quantum. The phase difference is related to the flux across the junction by $\Phi = \varphi \frac{\Phi_0}{2\pi}$.

Combining Eq. (2.1) and (2.2), we find inductive behavior $V = L_J \dot{I}$ of the Josephson junction with

$$L_J = \frac{\Phi_0}{2\pi I_c \cos \varphi}, \tag{2.3}$$

known as the Josephson inductance, a nonlinear phase-dependent inductance. For realistic implementations, a lossless Josephson junction can be modeled by an inductive tunneling element shunted by an electrical capacitance, inherently formed by the isolating barrier (see Figure 2.1(b)).

### 2.1.2 Quantization of a Josephson junction

Here we apply the canonical quantization procedure, developed by Dirac [18], to a Josephson junction. In the Josephson junction model with a capacitor shunt, energies of the junction can be written as the charging energy $T = C\varphi_0^2\dot{\varphi}^2/2$ and the magnetic energy of the Josephson inductance $U = -\varphi_0 I_c \cos\varphi$ with $C$ the capacitance of the shunt capacitor and $\varphi_0 = \Phi_0/(2\pi)$ the reduced flux quantum. Therefore, the Lagrangian of the system is given by

$$\mathcal{L}(\varphi, \dot{\varphi}) = T - U = \frac{C\varphi_0^2\dot{\varphi}^2}{2} + \varphi_0 I_c \cos\varphi. \tag{2.4}$$

The conjugate momentum of the phase $\varphi$ is defined as

$$p = \frac{\partial \mathcal{L}}{\partial \dot{\varphi}} = C\varphi_0^2\dot{\varphi}. \tag{2.5}$$

Using the Legendre transformation $H = \dot{\varphi}p - \mathcal{L}$, we obtain the Hamiltonian of the Josephson junction

$$H = \frac{p^2}{2C\varphi_0^2} - \varphi_0 I_c \cos\varphi. \tag{2.6}$$

The above Hamiltonian can also be written as

$$H = E_C p^2/\hbar^2 - E_J \cos\varphi, \tag{2.7}$$

where $E_C = (2e)^2/(2C)$ is the single cooper pair charging energy and $E_J = I_c\varphi_0$ is known as the Josephson energy.

So far, the system is described in the language of classical Hamiltonian mechanics. The passage from the classical to quantum description is described as follows: the classical variables are replaced by corresponding operators and the Hamiltonian is replaced by a function of operators, *i.e.*

$$\varphi \to \hat{\varphi}, \quad p \to \hat{p}, \quad H \to \hat{H}. \tag{2.8}$$

The commutation relationship is imposed on pairs of operators corresponding to the conjugate variables. We have

$$[\hat{\varphi}, \hat{p}] = i\hbar. \tag{2.9}$$

The quantum behavior of the Hamiltonian in Eq. (2.6) is formally the same as a mechanical oscillator of effective mass $C\varphi_0^2$ within a cosine shape potential. Quantum mechanics allows only a few discrete values for the energy of the oscillator (see Figure 2.2). Due to the anharmonic potential of the Josephson junction, the energy differences between nearby

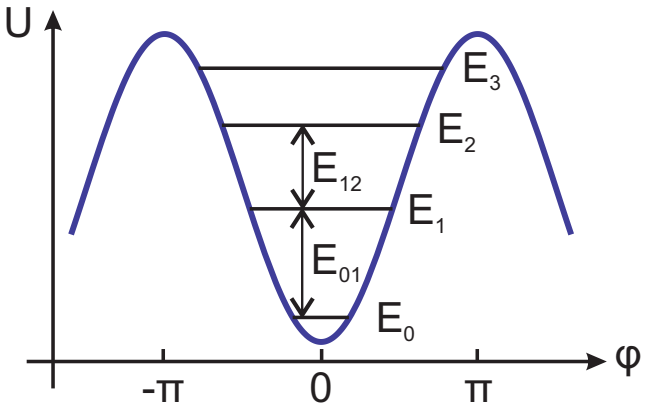



Figure 2.2: **Energy levels and the potential of a Josephson junction.** The blue line is the potential and the horizontal lines represent the corresponding energy levels. Due to the anharmonicity of the potential, we have $E_{01} \neq E_{12}$.

levels are not the same. This is qualitatively different from the case of a quantum harmonic oscillator. The nondegeneracy of energy differences in Josephson junction circuits allows the transitions between each individual level being addressed by frequency selection, which is essential to making a superconducting qubit.

## 2.2 Superconducting flux qubits

There are several designs of superconducting qubits including the phase qubit [19], the Cooper pair box [20], the transmon [21], and the persistent current qubit [22]. A critical difference between the different qubit types is the ratio $E_{\mathrm{J}}/E_{\mathrm{C}}$. This ratio alters the nature of the wavefunctions and their sensitivity to charge and flux fluctuations. Among these qubit designs, the persistent current qubit, also known as the flux qubit, is designed in the $E_{\mathrm{J}} \gg E_{\mathrm{C}}$ regime. It has a large level of anharmonicity in the qubit potential, which enables ideal two-level system behavior in the qubit control experiments.

The flux qubit consists of a superconducting loop with at least three Josephson junctions. While a particular design could have more junctions, the basic feature of the qubit potential remains similar. Figure 2.3 is a schematic drawing of a qubit circuit with three junctions where one of them is $\alpha$ times smaller than the other two. If the geometric inductance of the loop is considered negligible, the potential energy of the system is the sum of

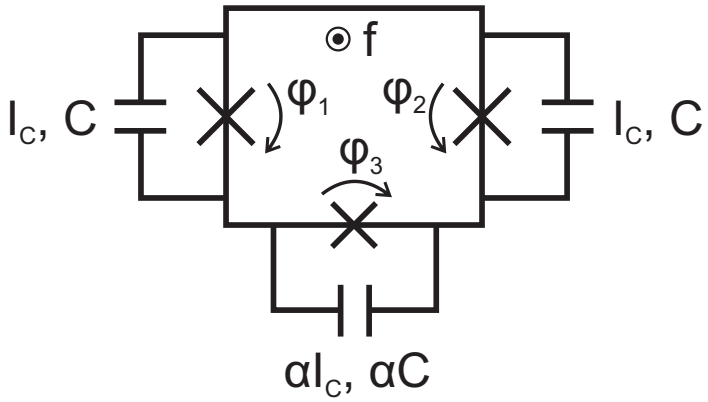



Figure 2.3: **Schematic diagram of the flux qubit.** The flux qubit consists of a superconducting loop interrupted by three Josephson junctions. The third junction is smaller in the critical current as well as the capacitance than the other two by a factor of $\alpha$ ($\alpha > 0.5$). An external magnetic flux $f$ in units of $\Phi_0$ is imposed into the qubit loop.

the inductive energy of each junction:

$$U = -E_{\mathrm{J}}(\cos\varphi_1 + \cos\varphi_2 + \alpha\cos\varphi_3) \tag{2.10}$$

where $E_{\mathrm{J}} = \varphi_0 I_{\mathrm{c}}$ is defined as the Josephson energy and $\varphi_i$ ($i = 1, 2, 3$) is the phase difference across junction $i$. The macroscopic wave function of the superconductor must be single-valued around the qubit ring. This imposes the phase quantization condition

$$\sum_i \varphi_i + 2\pi f = 2\pi N, \tag{2.11}$$

where $f = \Phi/\Phi_0$ is the external magnetic frustration in the qubit loop and $N$ is an integer. Under the phase quantization condition, the Lagrangian of the flux qubit only depends on two variables which we choose to be the phase across the larger junctions $\varphi_1$ and $\varphi_2$. With $\varphi_p = (\varphi_1 + \varphi_2)/2$ and $\varphi_m = (\varphi_1 - \varphi_2)/2$, the quantum Hamiltonian of the flux qubit can be written as

$$H = \frac{p_p^2}{2m_p} + \frac{p_m^2}{2m_m} + E_{\mathrm{J}}\left(-2\cos\varphi_p\cos\varphi_m - \alpha\cos(2\pi f + 2\varphi_m)\right) \tag{2.12}$$

where $p_p$ and $p_m$ are the conjugate momenta of $\varphi_p$ and $\varphi_m$, $m_p = 2C\varphi_0^2$, and $m_m = 2C(1+2\alpha)\varphi_0^2$. By defining $E_{\mathrm{C}} = (2e)^2/(2C)$ as the charging energy, the Hamiltonian

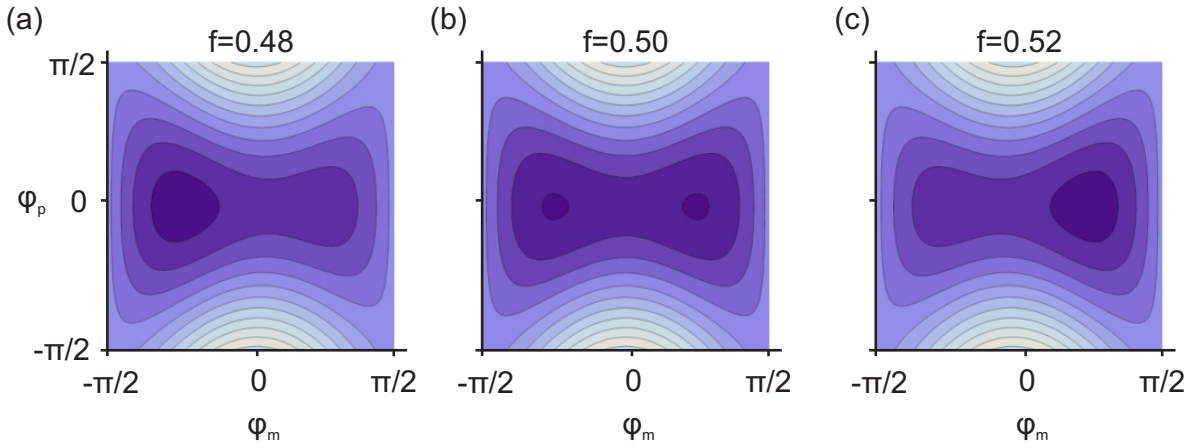



Figure 2.4: **Potential energy of the flux qubit.** The potential of the flux qubit is plotted as a function of phases $\varphi_p$ and $\varphi_m$ for three externally magnetic frustration: $f = 0.48$ (a), $f = 0.5$ (b), and $f = 0.52$ (c). The calculations are performed with $\alpha = 0.7$.

above can be expressed in terms of the energies $E_{\mathrm{C}}$ and $E_{\mathrm{J}}$ as

$$H = \frac{E_{\mathrm{C}}}{2}\left(\frac{\partial^2}{\partial\varphi_p^2} + \frac{1}{1+2\alpha}\frac{\partial^2}{\partial\varphi_m^2}\right) + E_{\mathrm{J}}\left(-2\cos\varphi_p\cos\varphi_m - \alpha\cos(2\pi f + 2\varphi_m)\right). \tag{2.13}$$

We can understand the energy level structure of the qubit by first considering the shape of the potential in Eq. (2.12). Figure 2.4 shows the potential landscape versus the two degrees of freedom $\varphi_p$ and $\varphi_m$ for $\alpha = 0.7$. When the external frustration $f$ is close to 0.5, the potential has two minima, located around $\varphi_p = 0$ and $\varphi_m = \pm\arccos(1/(2\alpha))$. In the regime where $E_{\mathrm{J}} > E_{\mathrm{C}}$, the wave functions of the two states with the lowest energy levels are approximately localized in each minima respectively. We can use a tight-binding model [23] to calculate the energies of the eigenstates.

We let $|L\rangle$ and $|R\rangle$ denote the wave functions of the state localized on the left and right side of the double-well potential. The Hamiltonian in Eq. (2.12) can be projected to the basis consisting of $|L\rangle$ and $|R\rangle$ as

$$H = \frac{1}{2}\begin{pmatrix} -\epsilon & \Delta \\ \Delta & \epsilon \end{pmatrix}, \tag{2.14}$$

The energy difference between the two localized states is given by

$$\epsilon = \frac{2\partial U}{\partial f}\left(f - \frac{1}{2}\right) = 2I_{\mathrm{p}}\Phi_0\left(f - \frac{1}{2}\right) \tag{2.15}$$

with $I_p$ defined as the persistent current. The tunneling matrix element between the two states is defined as $\Delta$. The parameter $\Delta$ depends on the ratio of $E_J/E_C$ and the ratio of the junction sizes $\alpha$. Since the wave function localized on either side of the double-well corresponds to an average circulating current in the opposite direction of the other, $|L\rangle$ and $|R\rangle$ are also known as the circulating current states, written as $|\circlearrowleft\rangle$ and $|\circlearrowright\rangle$. The Hamiltonian of the qubit in the Pauli matrix basis formed by the circulating current states is given by

$$H = -\frac{\epsilon}{2}\sigma_z + \frac{\Delta}{2}\sigma_x. \tag{2.16}$$

The energy eigenvalues of the qubit are

$$E_{0,1} = \pm\frac{1}{2}\sqrt{\epsilon^2 + \Delta^2} \tag{2.17}$$

with eigenstates given by

$$|0\rangle = \sin\frac{\theta}{2}|\circlearrowleft\rangle - \cos\frac{\theta}{2}|\circlearrowright\rangle, \tag{2.18}$$

$$|1\rangle = \cos\frac{\theta}{2}|\circlearrowleft\rangle + \sin\frac{\theta}{2}|\circlearrowright\rangle, \tag{2.19}$$

where $\theta = \tan^{-1}(\Delta/\epsilon)$. The operator representing the persistent current in the qubit loop is defined as

$$I_{pc} = I_p(|\circlearrowleft\rangle\langle\circlearrowleft| - |\circlearrowright\rangle\langle\circlearrowright|) = I_p\sigma_z. \tag{2.20}$$

In Figure 2.5, we show the energy levels of the flux qubit versus the external frustration $f$. As we bias the qubit very far away from the symmetry point ($\epsilon \gg \Delta$), the energy level difference of the qubit is approximately $\epsilon$ and the eigenstates are just the circulating current states $|\circlearrowleft\rangle$ and $|\circlearrowright\rangle$. At the symmetry point ($\epsilon = 0$), the energy level difference of the qubit has its minimum, $\Delta$. The energy eigenstates are the symmetric and anti-symmetric combinations of the circulating current state, *i.e.* $|0\rangle = (|\circlearrowleft\rangle + |\circlearrowright\rangle)/\sqrt{2}$ and $|1\rangle = (|\circlearrowleft\rangle - |\circlearrowright\rangle)/\sqrt{2}$. As the flux qubit is commonly operated at the symmetry point in experiments, it is more convenient to express the Hamiltonian in the basis of the energy eigenstates $|0\rangle$ and $|1\rangle$ as

$$H = -\frac{\Delta}{2}\sigma_z + \frac{\epsilon}{2}\sigma_x. \tag{2.21}$$

## 2.3 Superconducting resonators

Superconducting resonators are another important element in superconducting circuits. They serve as containers of stationary microwave photons which can be used as quantum

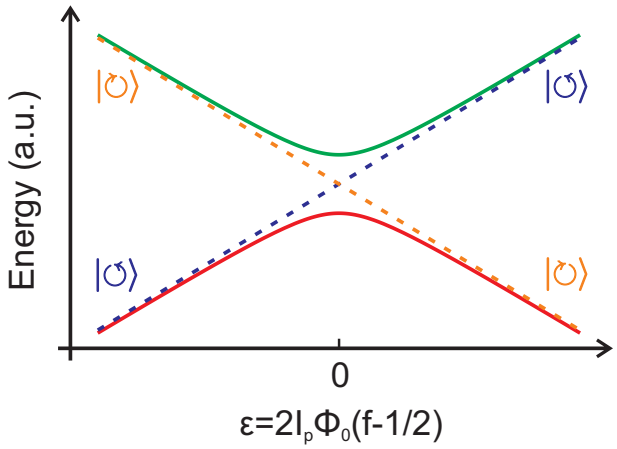



Figure 2.5: **Energy level structure of the flux qubit.** The energies of the ground and excited state of the flux qubit (solid line) are plotted versus the external frustration $f$. The dashed lines are the energies of the circulating current state, $|\circlearrowleft\rangle$ and $|\circlearrowright\rangle$, which become the energy eigenstates while the qubit is biased away from the symmetry point.

memories for information storage, quantum buses to couple superconducting qubits, or measurement apparatuses for qubit-state readout. In this section, we will introduce two types of superconducting resonators, the lumped-element LC resonator and the transmission-line resonator. We will then describe these resonators using the language of quantum mechanics.

### 2.3.1 Lumped-element resonators

The simplest harmonic oscillator that can be built with superconducting circuits is the LC resonator, which comprises an inductance $L$ in parallel with a capacitor $C$. The quantization procedure of a LC resonator is similar to that of a Josephson junction which has been discussed in Section 2.1.2. The Hamiltonian of the system is given by

$$H = \frac{p^2}{2C\varphi_0^2} + \frac{\varphi_0^2\varphi^2}{2L} \tag{2.22}$$

with $\varphi$ the superconducting phase across the inductor and $p$ the conjugate momentum, which satisfy $[\varphi, p] = i\hbar$.

We introduce the creation and annihilation operators:

$$a^\dagger = \sqrt{\frac{C\varphi_0^2\omega_\mathrm{r}}{2\hbar}}\left(\varphi - \frac{i}{C\varphi_0^2\omega_\mathrm{r}}p\right),$$
$$a = \sqrt{\frac{C\varphi_0^2\omega_\mathrm{r}}{2\hbar}}\left(\varphi + \frac{i}{C\varphi_0^2\omega_\mathrm{r}}p\right), \tag{2.23}$$

with $\omega_\mathrm{r} = 1/\sqrt{LC}$ the resonance frequency. We obtain a Hamiltonian

$$H = \hbar\omega_\mathrm{r}(a^\dagger a + 1/2) \tag{2.24}$$

diagonal in a basis formed by Fock states $|n\rangle$ where

$$a^\dagger|n\rangle = \sqrt{n+1}|n+1\rangle,$$
$$a|n\rangle = \sqrt{n}|n-1\rangle. \tag{2.25}$$

The Fock state $|n\rangle$ is the photon number state with $n$ the number of photons stored in the resonator.

The operators corresponding to the voltage $V$ across the capacitor and the current $I$ through the inductor can be expressed in terms of the creation and annihilation operators:

$$V = \varphi_0\dot{\varphi} = i\sqrt{\frac{\hbar\omega_\mathrm{r}}{2C}}(a^\dagger - a), \tag{2.26}$$

$$I = \frac{\varphi_0\varphi}{L} = \sqrt{\frac{\hbar\omega_\mathrm{r}}{2L}}(a^\dagger + a). \tag{2.27}$$

### 2.3.2 Transmission-line resonators

A transmission line is a longitudinal structure which supports the propagation of electromagnetic modes. With boundary conditions, only some certain modes are allowed and the propagations and reflections of these modes lead to resonant behaviors. Just as a Fabry-Perot resonator, a segment of superconducting transmission line with reflective boundaries can be treated as a set of harmonic oscillators.

Different from lumped circuits, where the physical dimensions are much smaller than the wavelength, the dimension of a transmission line may be comparable with the wavelength. A transmission line resonator should be modeled as a distributed network, where voltages and currents can vary over its length [24]. Each infinitesimal segment of a transmission

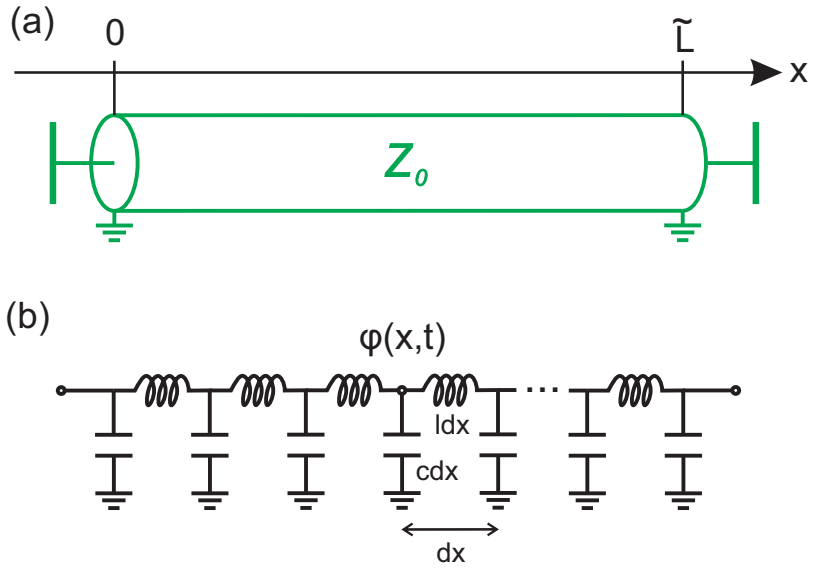



Figure 2.6: **Transmission line resonator and its schematic circuit model.** (a) A section of length $\tilde{L}$ of a transmission line ended in open circuit constitutes a resonator. (b) A lumped circuit model for the transmission line. Each infinitesimal segment of the transmission line is modeled by an inline inductor and a capacitor to the ground.

line can be modeled by the elementary circuit shown in Figure 2.6 where $l$ and $c$ are the inductance and capacitance per unit length.

We define the superconducting phase on the island in each infinitesimal segment of the transmission line as $\varphi(x,t)$. Therefore, the voltage between the island and the ground is given by $V(x,t) = \varphi_0\dot{\varphi}(x,t)$ and the current flowing through the center island is given by $I(x,t) = \varphi_0\partial_x\varphi(x,t)/l$. The Lagrangian of the system is given by

$$\mathcal{L} = \varphi_0^2 \int_0^{\tilde{L}} dx \left[ \frac{c(\partial_t\varphi(x,t))^2}{2} - \frac{(\partial_x\varphi(x,t))^2}{2l} \right] \tag{2.28}$$

with $\tilde{L}$ the total length of the transmission line. The Euler-Lagrange equation of the system is the wave equation:

$$v^2 \frac{\partial^2\varphi(x,t)}{\partial t^2} = \frac{\partial^2\varphi(x,t)}{\partial x^2} \tag{2.29}$$

where $v = 1/\sqrt{lc}$ is the speed of light in the transmission line. The boundary conditions for a transmission line resonator with an open circuit on both ends are given by $I(0,t) = I(\tilde{L},t) = 0$. With the boundary conditions above, the spatial configuration of $\varphi(x,t)$ in the transmission line resonator can be written as

$$\varphi(x,t) = \sqrt{\frac{2}{\pi k}} \sum_k \varphi_k(t) \cos\left(\frac{k\pi x}{\tilde{L}}\right) \tag{2.30}$$

where each $k$ term corresponds to an allowed resonance mode. Since Eq. (2.30) is a canonical transformation from variables $\varphi(x,t)$ to $\varphi_k(t)$, the equation of motion is invariant for the Lagrangian under such a transformation. The new Lagrangian after the transformation is given by

$$\mathcal{L} = \varphi_0^2 \sum_k \frac{\pi k}{\tilde{L}} \left[ \left(\frac{\tilde{L}}{\pi k}\right)^2 \frac{c(\partial_t\varphi_k(t))^2}{2} - \frac{\varphi_k^2(t)}{2l} \right]. \tag{2.31}$$

With the conjugate variable defined as $p_k = c\tilde{L}\dot{\varphi}/(\pi k)$, we obtain the Hamiltonian from the Legendre transformation as

$$H = \sum_k \frac{\pi k}{\tilde{L}} \left( \frac{p_k^2}{2c\varphi_0^2} + \frac{\varphi_0^2\varphi_k^2}{2l} \right). \tag{2.32}$$

This is the Hamiltonian of a number of independent LC resonators. For each $k$, the equivalent LC resonator has effective capacitance $C = c\tilde{L}/(\pi k)$, inductance $L = l\tilde{L}/(\pi k)$, and resonance frequency

$$\omega_k = \frac{\pi k}{\tilde{L}\sqrt{lc}}. \tag{2.33}$$

The Hamiltonian can be further written as

$$H = \sum_k \hbar\omega_k (a_k^\dagger a_k + 1/2), \tag{2.34}$$

where the annihilation operator of each resonance mode is given by

$$a_k = \sqrt{\frac{\varphi_0^2}{2\hbar Z_0}} \left( \varphi_k + \frac{iZ_0}{\varphi_0^2} p_k \right) \tag{2.35}$$

with $Z_0 = \sqrt{l/c}$ the characteristic impedance of the transmission line.

The voltage and current operators in the transmission line resonator can be expressed in terms of the creation and annihilation operators:

$$V(x) = \varphi_0 \dot{\varphi}(x,t) = \sum_k i\omega_k \sqrt{\frac{\hbar Z_0}{\pi k}} \cos\left(\frac{k\pi x}{\tilde{L}}\right) (a_k^\dagger - a_k), \tag{2.36}$$

$$I(x) = \varphi_0 \frac{\partial_x \varphi(x,t)}{l} = -\sum_k \omega_k \sqrt{\frac{\hbar}{Z_0 \pi k}} \sin\left(\frac{k\pi x}{\tilde{L}}\right) (a_k^\dagger + a_k). \tag{2.37}$$

## 2.4 Flux qubits in circuit quantum electrodynamics

Atoms coupled to discrete photon modes in optical cavities are the object of cavity quantum electrodynamics (cavity QED). Such systems are of great interest in the study of fundamental quantum optics and have been proposed as a possible architecture for quantum information processing [25, 26]. In the last decade, the circuit version of cavity QED, known as circuit quantum electrodynamics (circuit QED) [27, 28], has become increasingly popular. Circuit QED involves superconducting qubits as the artificial atoms and superconducting resonators as the cavities. In circuit QED, resonators provide a controlled electromagnetic environment protecting qubits from energy relaxation. In addition, resonators are used for qubit state measurement [29] and as quantum buses for qubit-qubit interaction [30].

The geometry of circuit QED under consideration is shown in Figure 2.7. It consists of a transmission line resonator, with its two ends capacitively coupled to transmission lines which allow measurements of the resonator transmission. A flux qubit is coupled to the resonator, via the mutual inductance of a shared line. The Hamiltonian of the system is given by

$$H = H_{\text{qb}} + H_{\text{r}} + H_{\text{int}} \tag{2.38}$$

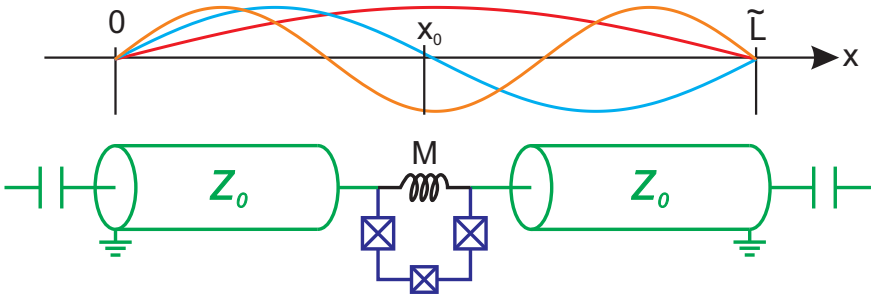



Figure 2.7: **Schematic layout of circuit QED using a superconducting flux qubit.** The 1D transmission line resonator consists of a section of superconducting coplanar waveguide. The flux qubit is directly connected to the center conductor of the waveguide. The solid line curves are current amplitudes of the first three modes of the resonator.

where $H_{\rm qb} = -\epsilon\sigma_z/2 + \Delta\sigma_x/2$ is the Hamiltonian of the qubit, $H_{\rm r} = \sum_k \hbar\omega_k(a^\dagger a + 1/2)$ is the Hamiltonian of the resonator, and $H_{\rm int}$ is the Hamiltonian corresponding to the magnetic dipole interaction between the qubit and the resonator. The form of the first two terms are derived in Section 2.2 and 2.3.2, while the interaction Hamiltonian $H_{\rm int}$ can be written as the magnetic energy stored in the mutual inductance which couples the qubit to the resonator. It is written as

$$H_{\rm int} = M I_{\rm pc} I(x_0), \tag{2.39}$$

where $M$ is the mutual inductance, $\hat{I}_{\rm pc}$ is the persistent current operator of the flux qubit, and $\hat{I}(x_0)$ is the current operator of the transmission line resonator at the qubit position $x_0$. Using Eq. (2.20) and (2.37) to express the current operators in the forms of Pauli operators and creation and annihilation operations, the interaction Hamiltonian is also written as

$$H_{\rm int} = \sum_k g_k(a_k^\dagger + a_k)\sigma_z \tag{2.40}$$

with

$$g_k = M I_{\rm p}\omega_k\sqrt{\hbar/(Z_0\pi k)}\sin(k\pi x_0/\tilde{L}). \tag{2.41}$$

We note that the above qubit Hamiltonian is in the basis consisting of the clockwise and anticlockwise circulating current states. If we use the energy eigenstates of the qubit at the symmetry point as basis states and only consider one mode of the resonator which is close to being in resonance with the qubit, the Hamiltonian of the system can be written

as

$$H = \hbar\omega_{\mathrm{r}}\left(a^{\dagger}a + \frac{1}{2}\right) + \frac{1}{2}\left(-\Delta\sigma_z + \epsilon\sigma_x\right) - g'(a^{\dagger} + a)\sigma_x, \tag{2.42}$$

where $\omega_{\mathrm{r}}$ is the resonance frequency of the resonator mode under consideration and $g'$ is the coupling to this mode.

Transforming Eq. (2.42) to the eigenbasis of the qubit (see Section 2.2), we obtain

$$H = \hbar\omega\left(a^{\dagger}a + \frac{1}{2}\right) - \frac{\nu}{2}\sigma_z - g'(a^{\dagger} + a)(\sin\theta\sigma_z - \cos\theta\sigma_x) \tag{2.43}$$

with $\nu = \sqrt{\epsilon^2 + \Delta^2}$ the energy level difference of the qubit and $\theta = \tan^{-1}(\epsilon/\Delta)$. Upon applying the rotating wave approximation (in a rotating frame with $U = \exp\left(\frac{i}{\hbar}(\hbar\omega a^{\dagger}a - \frac{\nu}{2}\sigma_z)t\right)$), we ignore the fast oscillatory terms in the above Hamiltonian and obtain:

$$H_{\mathrm{JC}} = \hbar\omega\left(a^{\dagger}a + \frac{1}{2}\right) - \frac{\nu}{2}\sigma_z + g(a^{\dagger}\sigma^{-} + a\sigma^{+}). \tag{2.44}$$

with $g = g'\cos\theta$. This is the well-known Jaynes-Cummings (JC) Hamiltonian [31] for a two-level system coupled to a resonator.

The JC Hamiltonian can be exactly diagonalized [26], which yields the dressed states as the energy eigenstates:

$$|\overline{+,n}\rangle = \cos\theta_n|e,n\rangle + \sin\theta_n|g,n+1\rangle, \tag{2.45}$$

$$|\overline{-,n}\rangle = -\sin\theta_n|e,n\rangle + \cos\theta_n|g,n+1\rangle \tag{2.46}$$

and ground state $|g,0\rangle$. The corresponding eigenenergies are given by

$$E_{\pm,n} = (n+1)\hbar\omega_{\mathrm{r}} \pm \frac{1}{2}\sqrt{4g^2(n+1) + \delta^2}, \tag{2.47}$$

$$E_{g,0} = -\frac{\delta}{2}. \tag{2.48}$$

In these expressions, we have

$$\theta_n = \frac{1}{2}\tan^{-1}\left(\frac{2g\sqrt{n+1}}{\delta}\right) \tag{2.49}$$

with $\delta = \nu - \hbar\omega_r$ the qubit-resonator detuning.

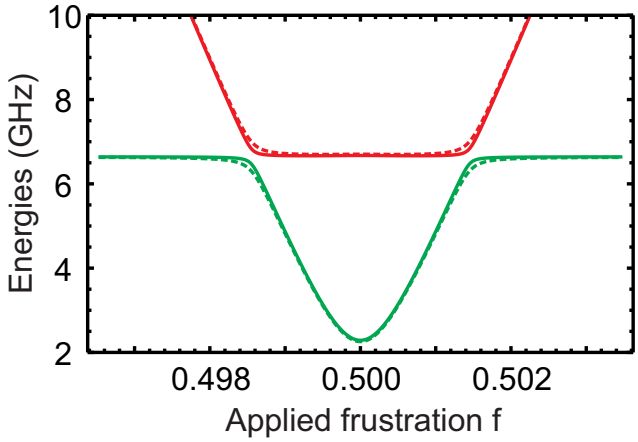



Figure 2.8: **Energy level structure of the flux qubit in circuit QED.** The energy differences between the ground state and the one-excitation manifold states are plotted versus the frustration applied to the flux qubit. The parameters used are $\omega_{\rm r} = 2\pi \times 6.641$ GHz, $\Delta/h = 2.320$ GHz, $I_{\rm p} = 691$ nA, and $g'/h = 523$ MHz. The solid lines are calculated based on the exact model while the dashed lines are calculated with the JC model.

### 2.4.1 Energy level spectrum

The computational basis of a qubit in circuit QED is usually chosen to be the basis consisting of the two lowest energy eigenstates $|g,0\rangle$ and $|\overline{+,0}\rangle$. However, due to the proximity of the energy of the other dressed states, especially $|\overline{-,0}\rangle$, we must take more states into account in practice. In Figure 2.8, we show the energy level structure of a flux qubit coupled to a resonator calculated using the exact model (Eq. (2.42)) and the JC model (Eq. (2.44)) respectively. By tuning qubit energy $\nu$ to $\hbar\omega_{\rm r}$, we expect vacuum Rabi splitting, *i.e.* the anticrossings between the resonator single-photon state $|g,1\rangle$ and the qubit first excited state $|e,0\rangle$. We note that the JC model, which is based on the rotating wave approximation, is a good approximation in the weak coupling limit where $g \ll \nu, \hbar\omega_{\rm r}$. With strong coupling, an analysis based on the exact model is required.

### 2.4.2 Dispersive regime

For large detuning, $g \ll \delta$, expansion of Eq. (2.47) yields the dispersive spectrum. In this situation, the eigenstates of the one-excitation manifold take the form

$$|\overline{+,0}\rangle \approx -|e,0\rangle + \frac{g}{\delta}|g,1\rangle, \tag{2.50}$$

$$|\overline{-,0}\rangle \approx \frac{g}{\delta}|e,0\rangle + |g,1\rangle. \tag{2.51}$$

It is easy to find from the above equation that the dressed state $|\overline{+,0}\rangle$ consists mainly of the bare excited state of the qubit and $|\overline{+,0}\rangle$ consists mainly the single-photon state of the resonator in this regime. To view this more explicitly, the JC Hamiltonian (Eq. (2.44)) can be diagonalized by applying a transformation $U = \exp\left[\frac{g}{\delta}(a\sigma^+ - a^\dagger\sigma^-)\right]$. The new Hamiltonian after the transformation up to the second order in $g$ is written as

$$H = \left(\hbar\omega_\mathrm{r} - \frac{g^2}{\delta}\sigma_z\right)a^\dagger a - \frac{1}{2}\left(\nu + \frac{g^2}{\delta}\right)\sigma_z. \tag{2.52}$$

The first term describes the dependence of the resonator frequency on the qubit dressed state via the operator $\sigma_z$. Thus, the dressed state of the qubit can be inferred from a measurement of the dressed resonator frequency, which is normally performed by measuring transmitted microwave signals through the resonator. The energy difference of the dressed qubit state is given by $\nu + 2ng^2/\delta + g^2/\delta$ which depends on the number of photons in the resonator. The second term which is proportional to $n$ corresponds to the ac-Zeeman effect, and the last term corresponds to the Lamb shift.

## 2.5 Experimental setup

### 2.5.1 Cryogenic setup

Experiments are performed in a Leiden Cryogenics dilution refrigerator, model CF-650. We use a custom design top loading probe for microwave transmission measurements [32]. The primary cryogenic design concern is to minimize the amount of heat and noise that reaches the sample from thermal sources or electronics.

#### Cryostat wiring

The schematic diagram of the wiring in the dilution refrigerator is shown in Figure 2.9. There are three types of pathways, the RF input, the RF output, and the DC lines.

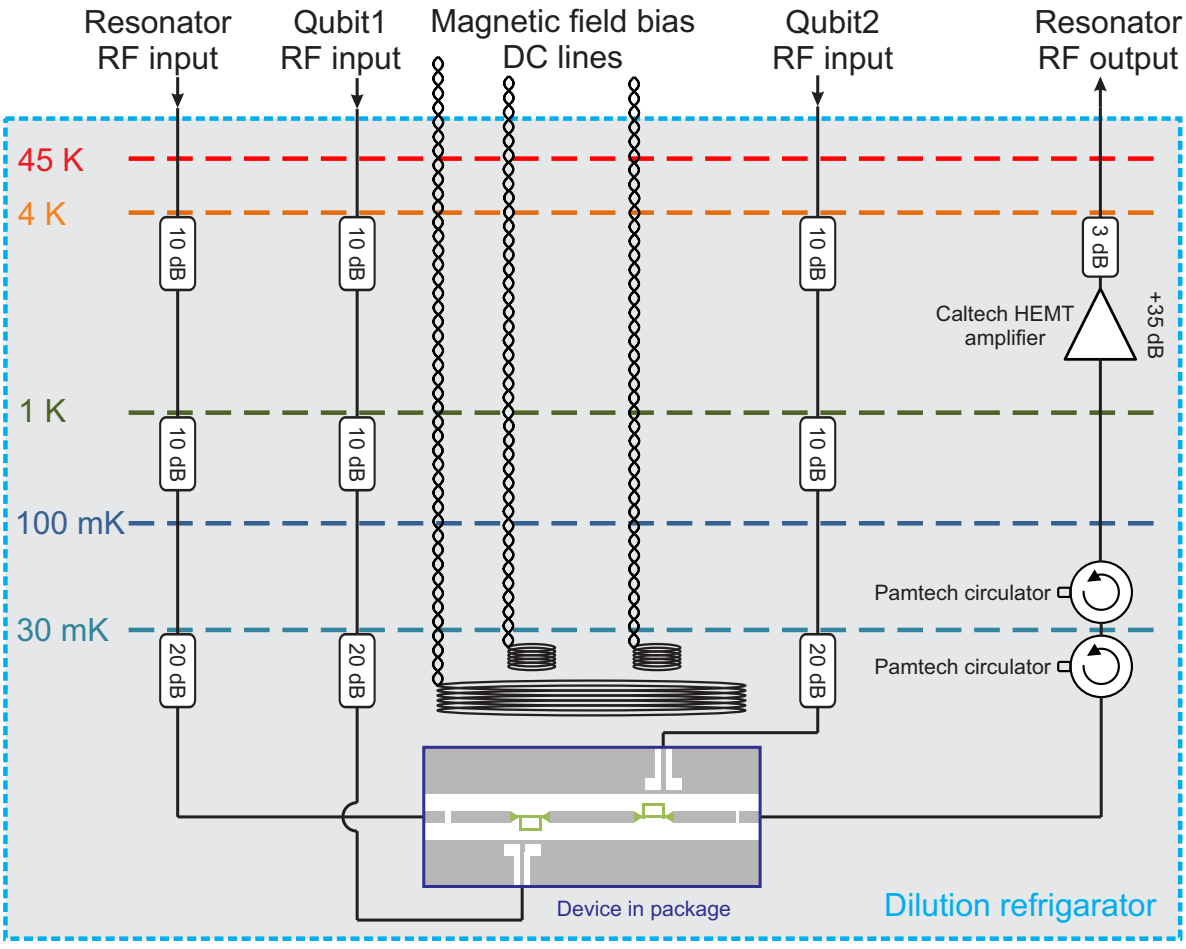



Figure 2.9: **Schematic diagram of the wiring setup.** See text for explanations.

The RF input lines are designed for delivering broadband signals to drive the qubits and the resonators. Since these lines are coupled to the high temperature electronics directly, the Johnson-Nyquist noise is transmitted through these lines and affects the coherence time of the qubits. In order to reduce this noise, we place microwave attenuators at different temperature stages. In each input line, attenuators of 10, 10, and 20 dB are mounted and thermally anchored on the 3 K, still (or 1 K), and mixing chamber stages respectively.

The RF output line is used for transferring transmitted microwaves from the device to the room temperature setup for measurements. On the RF output line, we use NbTi superconducting coaxial cables to reduce signal loss. The signal in this line is amplified by a high-electron mobility transistor (HEMT) amplifier, made by Caltech Microwave Research Group, Model Numbers CITCRY01-12, with a low temperature gain of about 33 - 36 dB in a bandwidth of 1-12 GHz. The amplifier is mounted on the 3K-stage of the dilution refrigerator and has a noise temperature of 4 K at 4-8 GHz. Two Pamtech CWJ1019-K414 isolators are placed in the output line on the mixing chamber stage to isolate the device from reflected microwaves and broad band noise from the HEMT amplifier.

The DC lines are used to supply DC currents to the superconducting coils to provide independent magnetic flux biases to the qubits. These lines are made of superconducting cryogenic wires which are thermally anchored on both the 3K and mixing chamber stages.

### Device box

Devices are wire-bonded with aluminum wires to a custom made microwave printed circuit board (PCB). The PCB is made from a Rogers TMM 10i panel and gold plated in a non-magnetic process with a thickness of 1 $\mu$m. The sample fits into a window cut-out in the center of the circular PCB and fastened to a bottom copper plate with cryogenic varnish. The PCB is fastened to the copper plate by brass screws. A photograph of the sample mounted to the PCB is shown in Figure 2.10. The PCB has coplanar waveguides (CPWs) with a 500 $\mu$m center trace width and a 250 $\mu$m gap and has a characteristic impedance of 50 $\Omega$. The traces are soldered to SMP connectors which mate with SMP bullets embedded in the top copper package. The complete package is then mounted on an insertable probe. The microwave connection mechanism between the sample box and the coaxial lines wired in the main insert of the refrigerator is described in detail in Ref. [32]. There are three superconducting coils (one main-coil and two mini-coils) mounted on the top of the sample box. The DC lines connected to the coils are wired on the probe.

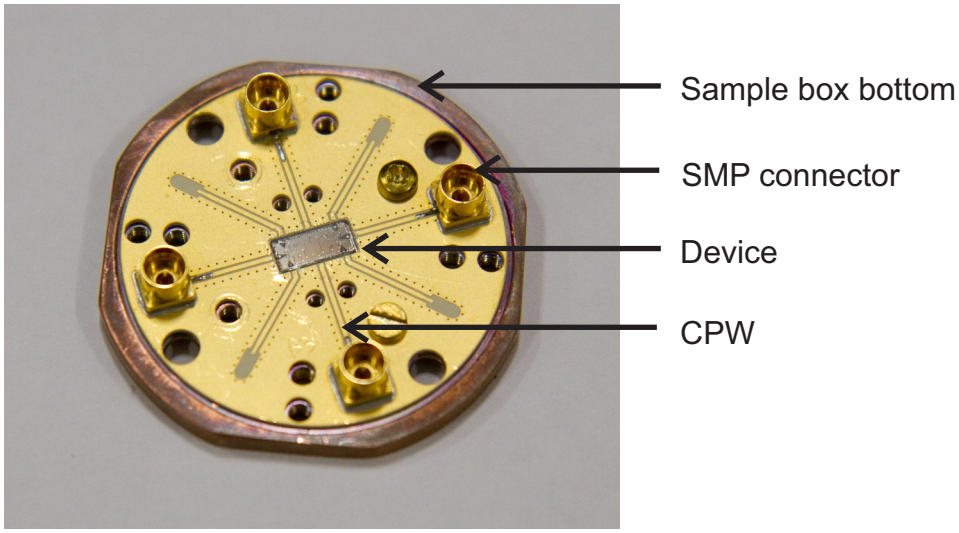



Figure 2.10: **Photograph of sample PCB and bottom part of the sample box.** See text for explanations.

### 2.5.2 Magnetic field shielding

The flux qubit is extremely sensitive to magnetic field fluctuations. To isolate the qubit from the noisy magnetic environment, we take extra cares in designing shielding systems for the magnetic fields.

Inside the cryostat, a three-layer high permeability metal shield is placed on the mixing chamber stage around the sample box. An active magnetic field compensation system placed outside the cryostat is used to further reduce slow drifts of the ambient magnetic field.

### 2.5.3 Pulse synthesis, demodulation and DC bias

The electronics for the synthesis and demodulation of microwave pulses as well as the generation of DC bias currents are placed outside of the cryostat. A detailed schematic is given in Figure 2.11.

For the decoherence and noise spectroscopy experiments, each qubit is controlled using shaped microwave pulses that are generated using a microwave synthesizer Agilent PSG

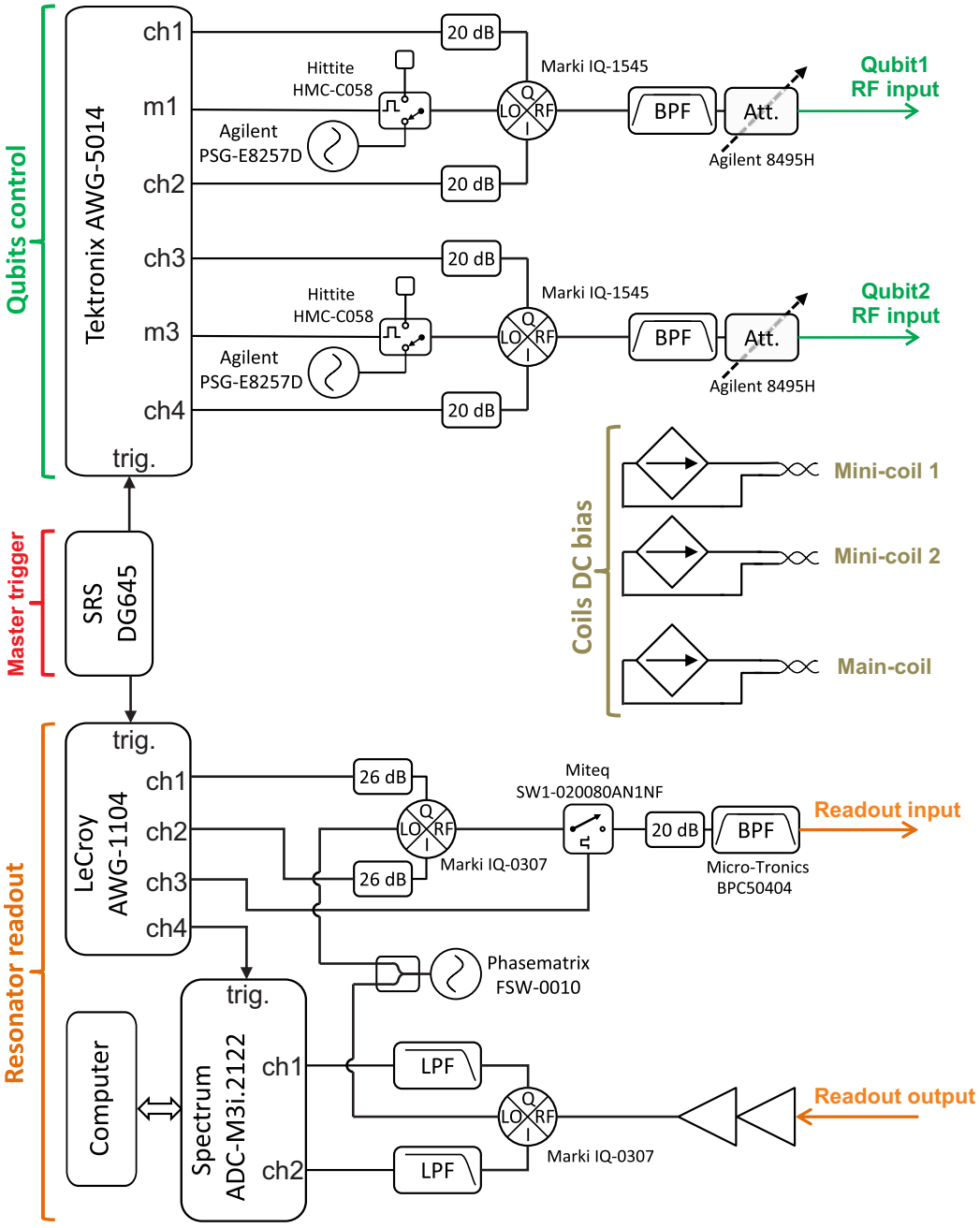



Figure 2.11: **Schematic of the room temperature control electronics.** See text for explanations.

E8257D, an arbitrary waveform generator Tektronix AWG5014, and a Marki IQ-0318 (IQ-1545) mixer. To further reduce microwave leakage to the qubit during coherent state evolution or qubit ground state initialization, each microwave synthesizer is isolated from the corresponding mixer by a Hittite HMC-C058 switch which provides an isolation $>$ 65 dB up to 6 GHz. Agilent 8495H Programmable step attenuators are used to adjust the pulse amplitude over a wide range. A band pass filter (BPF) in each control line is used to suppress low-frequency noise and spurious harmonics, which are detrimental to qubit coherence, and to prevent cavity excitation.

For experiments which requires fast time-domain control, the qubit control pulses are directly synthesized by an arbitrary waveform generator Tektronix AWG70002A at a sampling rate of 25 GSample/s (not shown in Figure 2.11). The AWG has an analog bandwidth of 13.5 GHz and an intrinsic rise/fall time of less than 22 ps. To generate pulses with a large bandwidth, the output of the AWG is connected to the Agilent 8495H Programmable step attenuators without passing through any filter. The output of the step attenuators are connected to the RF input lines which deliver the generated pulses to the qubits.

The readout pulses are generated in a similar fashion to the qubit control pulses, using a Phase Matrix QuickSyn FSW-0010 microwave synthesizer, a LeCroy AWG-1104 arbitrary waveform generator, a Marki IQ-0307 mixer, and a Miteq switch model SW1-020080AN1NF. The readout input line is filtered by a $6 - 10$ GHz band pass filter from Micro-Tronics, model BPC50404. The readout output signal is amplified using cryogenic and room temperature amplifiers. After demodulation, done with another Marki IQ-0307 mixer, the quadratures of the readout output pulse are sampled using a Spectrum M3i.2122 digitizer. A Stanford Research Systems digital delay generator DG645 controls the synchronization of the arbitrary waveform generators and the digitizer.

The DC bias are supplied by custom designed ultra-stable voltage to current converters, each controlled by a Yokogawa 7651 voltage source. Three current converters are used to bias one main-coil and two mini-coils independently.

# Chapter 3

# Driven evolution of a qubit

Periodic driving is the most widely used method to manipulate the states of quantum systems. In various qubit systems such as NMR, quantum dots, and superconducting devices, harmonic driving is used to induce transitions between different energy eigenstates, which forms the basis of single qubit operations. In this chapter, we will introduce methods for analyzing dynamics of a harmonically driven qubit. We will start with the well-known rotating wave approximation which is applicable to weak driving. We then introduce Floquet theory, a more natural and general method to treat periodic-driven systems. Finally, we show methods on calculating the quaienergies and Floquet states of a harmonically driven qubit using Floquet theory.

## 3.1 Rotating frame and rotating wave approximation

We start with a general model for a two-level system with Hamiltonian

$$H_{\mathrm{TLS}} = -\frac{\Delta}{2}\sigma_z + \frac{\epsilon}{2}\sigma_x, \tag{3.1}$$

where $\Delta$ and $\epsilon$ are parameters determined by the physical quantities of the system. In this model, we usually have control of at least one parameter, which we assume to be $\epsilon$ here without loss of generality. Commonly, the control parameter $\epsilon$ is given by the sum of DC and AC modulation: $\epsilon = \epsilon_0 + 2A\cos(\omega t + \phi)$. Thus the Hamiltonian becomes

$$H(t) = -\frac{\Delta}{2}\sigma_z + \frac{\epsilon_0}{2}\sigma_x + A\cos(\omega t + \phi)\sigma_x. \tag{3.2}$$

For a superconducting flux qubit (see Section 2.2 and Ref. [23]), $\Delta$ is the constant qubit gap, $\epsilon_0$ is controlled by the DC magnetic field biased onto the qubit, and $A$ is controlled by the amplitude of the AC modulation to the flux in the qubit loop. The Pauli matrices $\sigma_i$ are in a basis consisting of the states $|+\rangle = \frac{1}{\sqrt{2}}(|\circlearrowleft\rangle + |\circlearrowright\rangle)$ and $|-\rangle = \frac{1}{\sqrt{2}}(|\circlearrowleft\rangle - |\circlearrowright\rangle)$ which correspond to clockwise and counter-clockwise persistent current in the qubit. In the energy eigenstate basis of the qubit without AC modulation, the Hamiltonian in Eq. (3.2) is written as

$$\tilde{H}(t) = -\frac{\nu}{2}\tilde{\sigma}_z + A\cos(\omega t + \phi)\left(\frac{\Delta}{\nu}\tilde{\sigma}_x - \frac{\epsilon_0}{\nu}\tilde{\sigma}_z\right), \tag{3.3}$$

where $\tilde{\sigma}_i$ is in basis with $|0\rangle = \frac{\epsilon_0}{\chi}|+\rangle - \frac{\Delta+\nu}{\chi}|-\rangle$, $|1\rangle = \frac{\epsilon_0}{\chi}|+\rangle - \frac{\Delta-\nu}{\chi}|-\rangle$, $\nu = \sqrt{\Delta^2+\epsilon_0^2}$, and $\chi = \sqrt{\epsilon_0^2 + (\Delta+\nu)^2}$. The second term in the above Hamiltonian can be turned on/off by controlling the amplitude modulation factor $A$, which provides on-demand transitions between energy eigenstates. In the following sections of this chapter, we will focus on analyzing the dynamics of this Hamiltonian.

### 3.1.1 Rotating frame transformation

The dynamics of a time-dependent Hamiltonian system is usually complicated. In order to conveniently describe the dynamics, we perform a transformation by moving into another reference frame which evolves with a unitary transformation $U(t)$. With the state after a frame transformation given by $|\tilde{\psi}(t)\rangle = U(t)|\psi(t)\rangle$, the Hamiltonian in the new frame is written as

$$H_{\mathrm{RF}}(t) = U(t)^\dagger H(t) U(t) - U(t)^\dagger \dot{U}(t), \tag{3.4}$$

where $H(t)$ is the Hamiltonian before the frame transformation. For the driven qubit problem, we commonly define the rotating frame by performing a basis transformation given by

$$U(t) = e^{-i\frac{\omega}{2}\tilde{\sigma}_z t}. \tag{3.5}$$

As a result, the Hamiltonian in Eq. (3.3) in the rotating frame is written as

$$H_{\mathrm{RF}}(t) = -\frac{\nu-\omega}{2}\tilde{\sigma}_z + A\cos(\omega t + \phi)\left(\frac{\Delta}{\nu}\cos(\omega t)\tilde{\sigma}_x + \frac{\Delta}{\nu}\sin(\omega t)\tilde{\sigma}_y - \frac{\epsilon_0}{\nu}\tilde{\sigma}_z\right). \tag{3.6}$$

By using the trigonometric identities, the rotating frame Hamiltonian above can be explicitly expressed as

$$\begin{aligned} H_{\mathrm{RF}}(t) = -\frac{\delta}{2}\tilde{\sigma}_z + \frac{A\Delta}{2\nu}\left(\cos\phi\,\tilde{\sigma}_x + \sin\phi\,\tilde{\sigma}_y\right) \\ + \frac{A\Delta}{2\nu}\left(\cos(-2\omega t-\phi)\tilde{\sigma}_x + \sin(-2\omega t-\phi)\tilde{\sigma}_y\right) \\ + \frac{A\epsilon_0}{\nu}\cos(\omega t+\phi)\tilde{\sigma}_z, \end{aligned} \tag{3.7}$$

with $\delta = \nu - \omega$ being the detuning factor.

### 3.1.2 Rotating wave approximation

In the weak driving limit ($A \ll \omega$), the terms in Eq. (3.7) oscillating at frequencies $\omega$ and $2\omega$ can be ignored since the fast oscillating components average to zero in time scale much longer than $1/\omega$. This is known as the rotating wave approximation (RWA) [31]. The Hamiltonian after this approximation is given by

$$\tilde{H}_{\mathrm{RF}} = -\frac{\delta}{2}\tilde{\sigma}_z + \frac{A\Delta}{2\nu}\left(\cos\phi\,\tilde{\sigma}_x + \sin\phi\,\tilde{\sigma}_y\right). \tag{3.8}$$

This is a time-independent Hamiltonian representing a spin-1/2 particle precessing under a constant fictitious field $\vec{R} = (\frac{A\Delta}{2\nu}\cos\phi, \frac{A\Delta}{2\nu}\sin\phi, -\frac{\delta}{2})$. The precession frequency is known as the Rabi frequency given by

$$\Omega_{\mathrm{R}} = \sqrt{\delta^2 + A^2\left(\frac{\Delta}{\nu}\right)^2}. \tag{3.9}$$

With the amplitude $A$, frequency $\delta$, and phase $\phi$ all controlled by the AC modulation, we access arbitrary control of the amplitude and direction of the field $\vec{R}$, which enables arbitrary operations on a single qubit.

However, this simple picture under RWA is only valid in the weak driving regime ($A \ll \omega$). With strong driving, we have to take the fast-rotating terms in the exact Hamiltonian (Eq. (3.7)) into account, which results in time-dependent oscillations of the fictitious field. The dynamics of the qubit ends up being quite complicated. In Figure 3.1, we show the qubit evolution in the Bloch sphere [33] under different driving amplitude $A$. We consider the case of resonant driving ($\omega = \nu$) with phase $\phi = 0$ and the qubit biased at

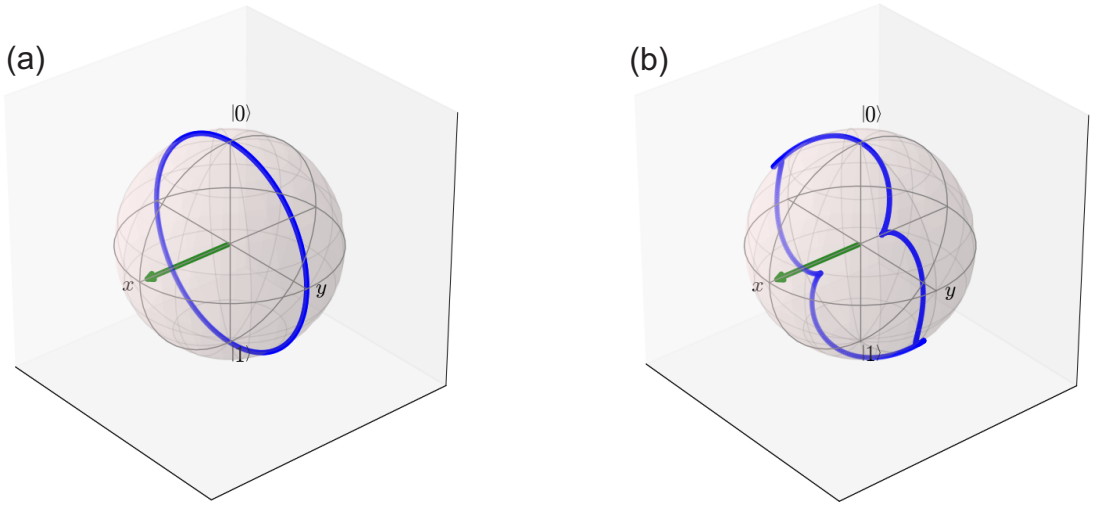



Figure 3.1: **Bloch sphere representations of the qubit evolution under various driving amplitude.** (a) Weak driving with $A = \omega/100$. (b) Strong driving with $A = \omega/2$. The qubit state evolutions are represented by the trajectories of the Bloch vector (blue lines).

its symmetry point ($\epsilon_0 = 0$). The calculation is performed by simulating the dynamics of Eq. (3.7) using a numerical solver [34]. With weak driving, the Bloch vector representing the qubit state undergoes Rabi oscillation around the $x$-axis. As the driving amplitude increase, fast oscillatory dynamics are observed in addition to the Rabi precession.

## 3.2 Floquet theory

To understand the complex dynamics beyond the RWA, we would like to have a more general method. The driven quantum system problem we have been working on can be naturally fit into the framework of the Floquet theory [35] which is a general treatment of the problems with periodic Hamiltonians.

We consider the Schrödinger equation with a time-dependent Hamiltonian $H(t)$ given by

$$i\frac{d}{dt}|\psi(t)\rangle = H(t)|\psi(t)\rangle, \tag{3.10}$$

where the Hamiltonian satisfies $H(t) = H(t+T)$ with $T$ the period. According to the Floquet theorem, there exist solutions to the Schrödinger equation of the form

$$|\Psi_\alpha(t)\rangle = e^{-i\varepsilon_\alpha t}|u_\alpha(t)\rangle, \tag{3.11}$$

where we call $|\Psi_\alpha(t)\rangle$ the Floquet states. In the above expression, $\varepsilon_\alpha$ are known as the quasienergies and $|u_\alpha(t)\rangle$ are known as the quasienergy states which also have a period $T$. The quasienergies are only uniquely defined up the multiples of $2\pi/T$, as the same Floquet state $|\Psi_\alpha(t)\rangle$ in Eq. (3.11) can be represented by quasienergies $\varepsilon_\alpha + 2\pi n/T$ and the corresponding quasienergy states $e^{-i2\pi nt/T}|u_\alpha(t)\rangle$, with $n$ any integer.

By substituting Eq. (3.11) into the Schrödinger equation Eq. (3.10), we obtain an eigenvalue equation

$$H_{\mathrm{F}}|u_\alpha(t)\rangle = \varepsilon_\alpha|u_\alpha(t)\rangle \tag{3.12}$$

where $H_{\mathrm{F}} = H(t) - i\partial_t$ is called the Floquet Hamiltonian. The quasienergies $\varepsilon_\alpha$ and quasienergy states $|u_\alpha(t)\rangle$ are the eigenvalues and eigenstates of the Floquet Hamiltonian respectively.

The solution of the Schrödinger equation for any time $t$ is a superposition of the Floquet states

$$|\psi(t)\rangle = \sum_\alpha c_\alpha|\Psi_\alpha(t)\rangle = \sum_\alpha c_\alpha e^{-i\varepsilon_\alpha t}|u_\alpha(t)\rangle, \tag{3.13}$$

where the coefficients $c_\alpha$ are determined by the initial wavefunction $|\psi(0)\rangle = \sum_\alpha c_\alpha |\Psi_\alpha(0)\rangle$. As a result, in the framework of Floquet theory, the problem of state evolution under a time-dependent Hamiltonian is turned into an eigenvalue problem. In some cases, this eigenvalue problem might be easier to solve and possibly provides more physical insight into the dynamics of the system.

## 3.3 Quasienergies and Floquet states of a harmonically driven qubit

In this section, we will discuss a method for solving the eigenvalues and eigenstates of the Floquet Hamiltonian and its applications to solving the dynamics of a harmonically driven qubit.

We start by representing the Floquet Hamiltonian operator $H_{\mathrm{F}} = H(t) - i\partial_t$ in a convenient basis. Since both $H(t)$ and $|u_\alpha(t)\rangle$ are periodic functions with period $T$, it is convenient to move to a discrete Fourier basis:

$$|u_\alpha(t)\rangle = \sum_{n=-\infty}^{\infty} a_{\alpha,n} |e^{in\omega t}\rangle, \tag{3.14}$$

where $\langle t|e^{in\omega t}\rangle = e^{in\omega t}$ and $\omega = 2\pi/T$. Thus the coefficients $a_{\alpha,n}$ are given by

$$a_{\alpha,n} = \langle e^{in\omega t}|u_\alpha(t)\rangle = \frac{1}{T}\int_0^T u_\alpha(t) e^{-in\omega t} dt, \tag{3.15}$$

where the inner product is defined in a Hilbert space spanning on the variable $t$:

$$\langle u_\beta(t)|u_\alpha(t)\rangle = \frac{1}{T}\int_0^T u_\beta^*(t) u_\alpha(t) dt. \tag{3.16}$$

In this new basis, the states $|u_\alpha(t)\rangle$ are expressed in a vector form:

$$|u_\alpha(t)\rangle = \begin{pmatrix} \vdots \\ a_{\alpha,n-1} \\ a_{\alpha,n} \\ a_{\alpha,n+1} \\ \vdots \end{pmatrix} \tag{3.17}$$

and the operators are in matrix forms:

$$-i\frac{\partial}{\partial t} = \omega \times \begin{pmatrix} \ddots & & & & \\ & n-1 & 0 & 0 & \\ & 0 & n & 0 & \\ & 0 & 0 & n+1 & \\ & & & & \ddots \end{pmatrix} = \omega \times M_N, \tag{3.18}$$

$$e^{i\omega t} = \begin{pmatrix} \ddots & & & & \\ & 0 & 1 & 0 & \\ & 0 & 0 & 1 & \\ & 0 & 0 & 0 & \\ & & & & \ddots \end{pmatrix} = M_P, \tag{3.19}$$

$$e^{-i\omega t} = \begin{pmatrix} \ddots & & & & \\ & 0 & 0 & 0 & \\ & 1 & 0 & 0 & \\ & 0 & 1 & 0 & \\ & & & & \ddots \end{pmatrix} = M_M. \tag{3.20}$$

Next, we consider the rotating frame Hamiltonian of a qubit driven by harmonic fields at its symmetry point:

$$H_{\mathrm{RF}}(t) = -\frac{\Delta-\omega}{2}\sigma_z + A\cos(\omega t+\phi)(\cos(\omega t)\sigma_x + \sin(\omega t)\sigma_y), \tag{3.21}$$

where the rotating frame is at the driving frequency $\omega$ and $\phi$ is the phase of the harmonic driving field. The Floquet Hamiltonian $H_{\mathrm{F}} = H_{\mathrm{RF}}(t) - i\partial_t$ in the Fourier basis is written as

$$\begin{aligned} H_{\mathrm{F}} = \omega(\mathbb{1}\otimes M_N) - \frac{\Delta-\omega}{2}(\sigma_z\otimes\mathbb{1}) + A\left(\sigma_x \otimes \frac{(M_P e^{i\phi} + M_M e^{-i\phi})(M_P + M_M)}{4}\right) \\ + A\left(\sigma_y \otimes \frac{(M_P e^{i\phi} + M_M e^{-i\phi})(M_P - M_M)}{4i}\right). \end{aligned} \tag{3.22}$$

We next evaluate the Kronecker products above and obtain a full matrix form for the

Floquet Hamiltonian:

$$H_{\mathrm{F}} = \begin{pmatrix} \ddots & & & & & & & & & \\ & \frac{-3\omega-\Delta}{2} & 0 & 0 & 0 & 0 & \frac{Ae^{-i\phi}}{2} & 0 & 0 & \\ & 0 & \frac{-\omega-\Delta}{2} & 0 & 0 & \frac{Ae^{i\phi}}{2} & 0 & \frac{Ae^{-i\phi}}{2} & 0 & \\ & 0 & 0 & \frac{\omega-\Delta}{2} & 0 & 0 & \frac{Ae^{i\phi}}{2} & 0 & \frac{Ae^{-i\phi}}{2} & \\ & 0 & 0 & 0 & \frac{3\omega-\Delta}{2} & 0 & 0 & \frac{Ae^{i\phi}}{2} & 0 & \\ & & & & & \ddots & & & & \\ & 0 & \frac{Ae^{-i\phi}}{2} & 0 & 0 & \frac{-3\omega+\Delta}{2} & 0 & 0 & 0 & \\ & \frac{Ae^{i\phi}}{2} & 0 & \frac{Ae^{-i\phi}}{2} & 0 & 0 & \frac{-\omega+\Delta}{2} & 0 & 0 & \\ & 0 & \frac{Ae^{i\phi}}{2} & 0 & \frac{Ae^{-i\phi}}{2} & 0 & 0 & \frac{\omega+\Delta}{2} & 0 & \\ & 0 & 0 & \frac{Ae^{i\phi}}{2} & 0 & 0 & 0 & 0 & \frac{3\omega+\Delta}{2} & \\ & & & & & & & & & \ddots \end{pmatrix}. \tag{3.23}$$

This matrix has a dimension of $2N \times 2N$ if we consider a total of $N$ Fourier basis states. We further perform a basis transformation $H'_{\mathrm{F}} = S^{\dagger} H_{\mathrm{F}} S$ with

$$S = \begin{pmatrix} \ddots & & & & & & & & & \\ & 1 & 0 & 0 & 0 & 0 & 0 & 0 & 0 & \\ & 0 & 0 & 0 & 0 & 0 & 1 & 0 & 0 & \\ & 0 & 0 & 1 & 0 & 0 & 0 & 0 & 0 & \\ & 0 & 0 & 0 & 0 & 0 & 0 & 0 & 1 & \\ & & & & & \ddots & & & & \\ & 0 & 0 & 0 & 0 & 1 & 0 & 0 & 0 & \\ & 0 & 1 & 0 & 0 & 0 & 0 & 0 & 0 & \\ & 0 & 0 & 0 & 0 & 0 & 0 & 1 & 0 & \\ & 0 & 0 & 0 & 1 & 0 & 0 & 0 & 0 & \\ & & & & & & & & & \ddots \end{pmatrix}. \tag{3.24}$$

This is equivalent to swapping all the $2n$-th rows with the $(2n + N)$-th rows of the state vector with $n$ any integer and $N$ the total number of Fourier basis used in the calculation.

After the change of basis, we finally obtain a block diagonal matrix

$$H'_{\mathrm{F}} = \begin{pmatrix} \ddots & & & & & & & & \\ & \frac{-3\omega-\Delta}{2} & \frac{Ae^{-i\phi}}{2} & 0 & 0 & 0 & 0 & 0 & 0 \\ & \frac{Ae^{i\phi}}{2} & \frac{-\omega+\Delta}{2} & \frac{Ae^{-i\phi}}{2} & 0 & 0 & 0 & 0 & 0 \\ & 0 & \frac{Ae^{i\phi}}{2} & \frac{\omega-\Delta}{2} & \frac{Ae^{-i\phi}}{2} & 0 & 0 & 0 & 0 \\ & 0 & 0 & \frac{Ae^{i\phi}}{2} & \frac{3\omega+\Delta}{2} & 0 & 0 & 0 & 0 \\ & & & & \ddots & & & & \\ & 0 & 0 & 0 & 0 & \frac{-3\omega+\Delta}{2} & \frac{Ae^{-i\phi}}{2} & 0 & 0 \\ & 0 & 0 & 0 & 0 & \frac{Ae^{i\phi}}{2} & \frac{-\omega-\Delta}{2} & \frac{Ae^{-i\phi}}{2} & 0 \\ & 0 & 0 & 0 & 0 & 0 & \frac{Ae^{i\phi}}{2} & \frac{\omega+\Delta}{2} & \frac{Ae^{-i\phi}}{2} \\ & 0 & 0 & 0 & 0 & 0 & 0 & \frac{Ae^{i\phi}}{2} & \frac{3\omega-\Delta}{2} \\ & & & & & & & & \ddots \end{pmatrix}. \tag{3.25}$$

We note that either block matrix above can be obtained from the other by adding an identity matrix $\pm\omega \times \mathbb{1}$. If we define two sets of basis associated with the above two block matrices, the transformation from one block matrix to the other is equivalent to a basis transformation where we multiplied the state vector of either block matrix by $e^{\pm i\omega t}$. Therefore, the quasienergies and quasienergy states given by either block matrix are the redundant copies of those given by the other one different by a shift of $\pm\omega$ in the quasienergies and a multiplication factor of $e^{\pm i\omega t}$ on the quasienergy states. Moreover, either block matrix is decoupled from the other, which means that the sub-space defined by either block matrix is isolated from the other. In our further calculations, we can only consider one block matrix such as

$$H''_{\mathrm{F}} = \begin{pmatrix} \ddots & & & & \\ & \frac{-3\omega-\Delta}{2} & \frac{Ae^{-i\phi}}{2} & 0 & 0 \\ & \frac{Ae^{i\phi}}{2} & \frac{-\omega+\Delta}{2} & \frac{Ae^{-i\phi}}{2} & 0 \\ & 0 & \frac{Ae^{i\phi}}{2} & \frac{\omega-\Delta}{2} & \frac{Ae^{-i\phi}}{2} \\ & 0 & 0 & \frac{Ae^{i\phi}}{2} & \frac{3\omega+\Delta}{2} \\ & & & & \ddots \end{pmatrix} \tag{3.26}$$

which contains all the physics relevant to our problem.

We obtain quasienergies by numerical diagonalization of $H''_{\mathrm{F}}$ using a numerical computing software [36]. In our calculations, we truncate the matrix $H''_{\mathrm{F}}$ with $n$ ranging from -50 to 50. Although the eigenvalue problem has 101 solutions, there are only two inequivalent

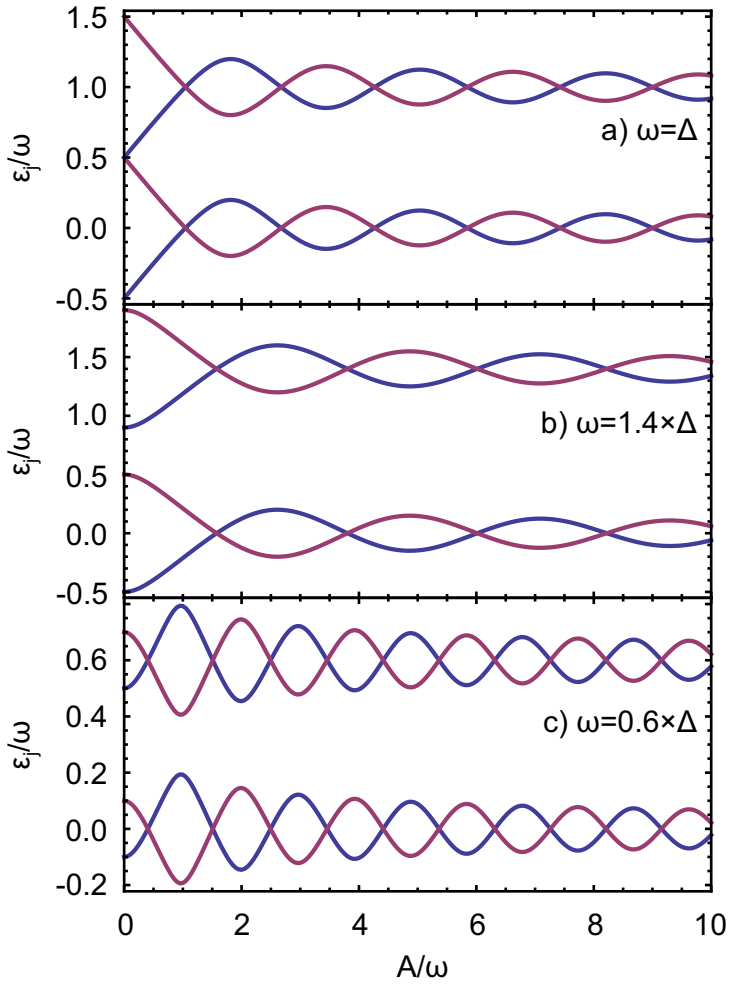



Figure 3.2: **Quasienergies of a harmonically driven qubit.** Quasienergies $\varepsilon_j$ versus the driving amplitude $A$ for on-resonance driving, $\omega = \Delta$ (a), and off-resonance driving, $\omega = 1.4\Delta$ (b) and $\omega = 0.6\Delta$ (c). The two inequivalent quasienergies are shown as red and blue lines respectively.

solutions and all the others are copies obtained by shifting an integer number of quanta $n$ between the quasienergy and the periodic part of the Floquet states. In Figure 3.2, we show quasienergies $\varepsilon_\alpha$ versus the driving amplitude $A$ at different driving frequencies. The two inequivalent quasienergies are drawn with different colors.

# Chapter 4

# Decoherence and noise characterization methods

Decoherence of quantum states is an important figure of merit in quantum information processing, as it limits the number of quantum operations that can be performed without error. There are two processes of different nature that can lead to decoherence. First, if there are resonances in the neighborhood of a quantum system with frequencies close to its level splitting, the system can emit or absorb energy and "jump" to another energy state. This is known as energy relaxation or longitudinal relaxation process. Second, low-frequency fluctuations in the environment perturb the parameters of the Hamiltonian and produce fluctuations in its energy splitting. These fluctuations lead to random evolution of the phase of a superposition state. This process is known as dephasing or transverse depolarization.

In this chapter, we will first discuss the theoretical description of decoherence by introducing the master equation and its relation to stochastic processes. Then, we will discuss characterization methods for decoherence and noise spectroscopy measurements with a single qubit. In the last section, we will discuss decoherence in a resonator.

## 4.1 Theoretical description of decoherence

The evolution of a quantum system is deterministic given that all the entities of the system are included in the Hamiltonian. Such a system, also known as a closed quantum system, can be described by the Schrödinger equation. While the description of a closed quantum

system is usually impossible due to the lack of knowledge to some of its parts, an open system approach [37] can be used in more practical applications. In the open system view of quantum mechanics, the system of interest is coupled to another quantum mechanical system called the environment, about which one has only partial knowledge. Although the combined system is closed and follows the dynamics of the Schrödinger equation, the time evolution of the open subsystem which only consists of the system of interest is not unitary. The interaction between the system of interest and the environment generates a certain correlation between them which is responsible for the nondeterministic character.

Decoherence can be viewed as loss of information from a system to its environment. The effect of information loss is to induce stochastic transitions between energy levels, and to introduce uncertainty in the phase difference between states of the system. The state of an open quantum system is described in terms of ensemble averaged states using the density matrix formalism. A density matrix $\rho$ describes a probability distribution of quantum states $|\psi_n\rangle$, in a matrix representation $\rho = \sum_n p_n |\psi_n\rangle\langle\psi_n|$, where $p_n$ is the classical probability that the system is in the quantum state $|\psi_n\rangle$. The time evolution of a density matrix $\rho$ is described by a master equation.

### 4.1.1 Born-Markov master equation

We will now derive the master equation under the Born-Markov approximation following the treatment by Carmichael [37]. We start from a closed system including both the system of interest and its environment. The evolution is governed by the Schrödinger equation $i\hbar\dot{\rho} = [H, \rho]$. The Hamiltonian under consideration is given by

$$H = H_{\mathrm{S}} + H_{\mathrm{SE}} + H_{\mathrm{E}}, \tag{4.1}$$

where $H_{\mathrm{S}}$, $H_{\mathrm{E}}$ and $H_{\mathrm{SE}}$ are the Hamiltonian corresponding to the system, environment, and coupling of between the system and the environment respectively.

We assume the system to be a multilevel system with energy eigenstates $|i\rangle$ and energy levels $\hbar\omega_i$. The coupling between the system and the environment is assumed to be an operator $A$, defined only in the Hilbert space of the system, multiplied by an operator $f$, defined in the space of the environment. The Hamiltonian of the system and the coupling can be written as

$$H_{\mathrm{S}} = \hbar \sum_i \omega_i |i\rangle\langle i|, \tag{4.2}$$

$$H_{\mathrm{SE}} = Af. \tag{4.3}$$

In the interaction picture, we have the density matrix $\tilde{\rho}$ and the Hamiltonian $\tilde{H}$ given by

$$\tilde{\rho} = e^{\frac{i}{\hbar}(H_{\mathrm{S}}+H_{\mathrm{E}})t}\rho e^{-\frac{i}{\hbar}(H_{\mathrm{S}}+H_{\mathrm{E}})t}, \tag{4.4}$$

$$\tilde{H} = e^{\frac{i}{\hbar}(H_{\mathrm{S}}+H_{\mathrm{E}})t}H_{\mathrm{SE}}e^{-\frac{i}{\hbar}(H_{\mathrm{S}}+H_{\mathrm{E}})t}. \tag{4.5}$$

Using the fact that $[f, H_{\mathrm{S}}] = 0$ and $[A, H_{\mathrm{E}}] = 0$, we obatain

$$\tilde{H}(t) = \sum_{j,k} |j\rangle\langle k|A_{jk}e^{i(\omega_j-\omega_k)t}\tilde{f}(t), \tag{4.6}$$

where $\tilde{f}(t) = e^{\frac{i}{\hbar}H_{\mathrm{E}}t}fe^{-\frac{i}{\hbar}H_{\mathrm{E}}t}$.

The Schrödinger equation in the interaction picture is given by

$$\dot{\tilde{\rho}} = -\frac{i}{\hbar}[\tilde{H}, \tilde{\rho}]. \tag{4.7}$$

We integrate the above equation to obtain

$$\tilde{\rho}(t) = -\frac{i}{\hbar}\int_0^t [\tilde{H}(t'), \tilde{\rho}(t')]dt' + \tilde{\rho}(0) \tag{4.8}$$

and substitute for $\tilde{\rho}$ inside the commutator in Eq. (4.7). We obtain

$$\dot{\tilde{\rho}}(t) = -\frac{i}{\hbar}[\tilde{H}(t), \tilde{\rho}(0)] - \frac{1}{\hbar^2}\int_0^t [\tilde{H}(t), [\tilde{H}(t'), \tilde{\rho}(t')]]dt'. \tag{4.9}$$

We next assume that the interaction is turned on at $t = 0$ and that no correlation exists between the system and the environment at this initial time. We then factorize $\tilde{\rho}$ as $\tilde{\rho}(0) = \tilde{\rho}_{\mathrm{S}}(0) \otimes \tilde{\rho}_{\mathrm{E}}(0)$. We note that the density matrix of the system is given by partially tracing over the environment part of the density matrix:

$$\tilde{\rho}_{\mathrm{S}} = \mathrm{Tr}_{\mathrm{E}}(\tilde{\rho}) = e^{\frac{i}{\hbar}H_{\mathrm{S}}t}\rho_{\mathrm{S}}e^{-\frac{i}{\hbar}H_{\mathrm{S}}t}. \tag{4.10}$$

After tracing over the environment in Eq. (4.9), we obtain

$$\dot{\tilde{\rho}}_{\mathrm{S}}(t) = -\frac{i}{\hbar}\mathrm{Tr}_{\mathrm{E}}[\tilde{H}(t), \tilde{\rho}(0)] - \frac{1}{\hbar^2}\int_0^t \mathrm{Tr}_{\mathrm{E}}[\tilde{H}(t), [\tilde{H}(t'), \tilde{\rho}(t')]]dt'. \tag{4.11}$$

For simplicity, we can eliminate the first term on the RHS of the equation above with the assumption $\mathrm{Tr}_{\mathrm{E}}[\tilde{H}(t), \tilde{\rho}_{\mathrm{E}}(0)] = 0$. This is guaranteed if the environment operator $\tilde{f}$ has zero mean in the state $\rho_{\mathrm{E}}(0)$. If this is not the case, this component can be introduced as an additional term to the system Hamiltonian.

### Born-Markov approximation

To simplify Eq. (4.11) further, two major approximations are usually made. The first major approximation, known as the *Born approximation* contains the following assumptions: first, the coupling between the system and the environment is very weak so that the composite state $\tilde{\rho}$ can be factorized. Second, the environment is a large system whose state should be unchanged by the coupling. Formally, we can write the density matrix in the following form:

$$\tilde{\rho}(t) = \tilde{\rho}_{\mathrm{S}}(t) \otimes \tilde{\rho}_{\mathrm{E}}(0). \tag{4.12}$$

The second major approximation we will make is the *Markov approximation*. In the Markov approximation, we assume that the current state of the system $\tilde{\rho}(t)$ does not depend on its history $\tilde{\rho}(t')$. As a result, we can replace the historical state $\tilde{\rho}(t')$ in the integral of Eq. (4.11) by the current state $\tilde{\rho}(t)$.

Finally, we reach a differential equation describing only the dynamics of the system:

$$\dot{\tilde{\rho}}_{\mathrm{S}}(t) = -\frac{1}{\hbar^2}\int_0^t \mathrm{Tr}_{\mathrm{E}}[\tilde{H}(t), [\tilde{H}(t'), \tilde{\rho}_{\mathrm{S}}(t) \otimes \tilde{\rho}_{\mathrm{E}}(0)]]dt' \tag{4.13}$$

$$\begin{aligned} = -\frac{1}{\hbar^2}\int_0^t \mathrm{Tr}_{\mathrm{E}}[&\tilde{H}(t)\tilde{H}(t')\tilde{\rho}(t) - \tilde{H}(t)\tilde{\rho}(t)\tilde{H}(t') \\ &-\tilde{H}(t')\tilde{\rho}(t)\tilde{H}(t) + \tilde{\rho}(t)\tilde{H}(t')\tilde{H}(t)]dt'. \end{aligned} \tag{4.14}$$

This equation is known as the Born-Markov master equation.

We can evaluate the integral of Eq. (4.14) to further understand the dynamics of the system. The first term in the integral is given by

$$\begin{aligned} &\frac{1}{\hbar^2}\int_0^t \mathrm{Tr}_{\mathrm{E}}[\tilde{H}(t)\tilde{H}(t')\tilde{\rho}(t)] \\ &\quad = \frac{1}{\hbar^2}\sum_{jkk'} A_{jk}A_{kk'}|j\rangle\langle k'|\tilde{\rho}_{\mathrm{S}}(t)\int_0^t e^{i\omega_{jk}t - i\omega_{k'k}t'}\langle \tilde{f}(t)\tilde{f}(t')\rangle dt', \end{aligned} \tag{4.15}$$

with $\omega_{jk} = \omega_j - \omega_k$.

If the operator associated with the environment can be described as a stationary process, *i.e.*

$$\langle \tilde{f}(t)\tilde{f}(t')\rangle = \langle \tilde{f}(t-t')\tilde{f}(0)\rangle, \tag{4.16}$$

we can relate the time correlation function in Eq. (4.15) to its power spectral density (PSD) by

$$S(\omega) = \int_{-\infty}^{\infty} d\tau e^{i\omega\tau} \langle \tilde{f}(\tau)\tilde{f}(0)\rangle, \tag{4.17}$$

$$\langle \tilde{f}(\tau)\tilde{f}(0)\rangle = \frac{1}{2\pi}\int_{-\infty}^{\infty} d\omega e^{-i\omega\tau} S(\omega). \tag{4.18}$$

Under the Markov approximation, the process $\tilde{f}(t)$ is assumed to have a short correlation time, where the time correlation function $\langle \tilde{f}(\tau)\tilde{f}(0)\rangle$ can be seen as a delta function. As a result, the lower limit of the time integral in Eq. (4.15) can be extended from 0 to $-\infty$. We rewrite Eq. (4.15) as

$$\begin{aligned}
&\frac{1}{\hbar^2}\int_0^t \mathrm{Tr}_\mathrm{E}[\tilde{H}(t)\tilde{H}(t')\tilde{\rho}(t)] \\
&\quad\approx \frac{1}{2\pi\hbar^2}\sum_{jkk'} A_{jk}A_{kk'}|j\rangle\langle k'|\rho(t)\int_{-\infty}^{t} dt' e^{i\omega_{jk}t - i\omega_{k'k}t'}\int_{-\infty}^{\infty} d\omega e^{-i\omega(t-t')}S(\omega) \\
&\quad\approx \frac{1}{2\pi\hbar^2}\sum_{jkk'} A_{jk}A_{kk'}|j\rangle\langle k'|\rho(t)\int_{-\infty}^{\infty} d\omega S(\omega) e^{i(\omega_{jk}-\omega_{k'k})t}\int_{-\infty}^{t} dt' e^{i(\omega-\omega_{k'k})(t'-t)} \\
&\quad\approx \frac{1}{2\hbar^2}\sum_{jkk'} A_{jk}A_{kk'}|j\rangle\langle k'|\rho(t)e^{i(\omega_{jk}-\omega_{k'k})t}\int_{-\infty}^{\infty} d\omega S(\omega)\delta(\omega-\omega_{k'k}) \\
&\quad\approx \frac{1}{2\hbar^2}\sum_{jkk'} A_{jk}A_{kk'}|j\rangle\langle k'|\rho(t)e^{i(\omega_{jk}-\omega_{k'k})t}S(\omega_{k'k}) \\
&\quad\approx \frac{1}{2\hbar^2}\sum_{jk} |A_{jk}|^2|j\rangle\langle j|\rho(t)S(\omega_{jk}),
\end{aligned} \tag{4.19}$$

with

$$\frac{1}{2\pi}\int_{-\infty}^{t} e^{i(\omega-\omega_{k'k})(t'-t)}dt' = \frac{1}{2}\delta(\omega-\omega_{k'k}), \tag{4.20}$$

and the rotating wave approximation is applied to eliminate the fast rotating terms $e^{i(\omega_{jk}-\omega_{k'k})t}$ for $k' \neq j$.

The other terms in the integral of Eq. (4.14) can be calculated in a similar way. The second term is written as

$$\frac{1}{\hbar^2}\int_0^t \mathrm{Tr}_\mathrm{E}[\tilde{H}(t)\tilde{\rho}(t)\tilde{H}(t')] \approx \frac{1}{2\hbar^2}\sum_{jk}|j\rangle\langle k|\rho(t)|k\rangle\langle j||A_{jk}|^2 S(-\omega_{jk}). \tag{4.21}$$

The third term $\frac{1}{\hbar^2}\int_0^t \mathrm{Tr}_\mathrm{E}[\tilde{H}(t')\tilde{\rho}(t)\tilde{H}(t)]$ has the same form as Eq. (4.21). The fourth term is given by

$$\frac{1}{\hbar^2}\int_0^t \mathrm{Tr}_\mathrm{E}[\tilde{\rho}(t)\tilde{H}(t')\tilde{H}(t)] \approx \frac{1}{2\hbar^2}\sum_{jk}\rho(t)|j\rangle\langle j||A_{jk}|^2 S(\omega_{jk}) \tag{4.22}$$

Altogether, the Born-Markov master equation Eq. (4.14) is given by

$$\dot{\rho}(t) = \frac{1}{2\hbar^2}\sum_{jk}|A_{jk}|^2 S(\omega_{jk})\left[2|k\rangle\langle j|\rho(t)|j\rangle\langle k| - \rho(t)|j\rangle\langle j| - |j\rangle\langle j|\rho(t)\right]. \tag{4.23}$$

**Application to a qubit**

In the case of a qubit, the dimension of the Hilbert space is two where we have $j, k = 0, 1$. The relaxation process is characterized by the Eq. (4.23) when $j \neq k$. We have

$$\begin{aligned}\dot{\rho}(t) = \Gamma_{1\to0}[\hat{\sigma}_-\rho(t)\hat{\sigma}_+ - \frac{1}{2}\hat{\sigma}_+\hat{\sigma}_-\rho(t) - \frac{1}{2}\rho(t)\hat{\sigma}_+\hat{\sigma}_-] \\ + \Gamma_{0\to1}[\hat{\sigma}_+\rho(t)\hat{\sigma}_- - \frac{1}{2}\hat{\sigma}_-\hat{\sigma}_+\rho(t) - \frac{1}{2}\rho(t)\hat{\sigma}_-\hat{\sigma}_+].\end{aligned} \tag{4.24}$$

We can write the above equation in a form using superoperators:

$$\dot{\rho}(t) = \Gamma_{1\to0}\mathcal{L}[\hat{\sigma}_-]\rho(t) + \Gamma_{0\to1}\mathcal{L}[\hat{\sigma}_+]\rho(t) \tag{4.25}$$

where $\mathcal{L}[\hat{\sigma}]\rho(t) = \hat{\sigma}\rho(t)\hat{\sigma}^\dagger - \frac{1}{2}\hat{\sigma}^\dagger\hat{\sigma}\rho(t) - \frac{1}{2}\rho(t)\hat{\sigma}^\dagger\hat{\sigma}$ is known as the Lindblad superoperator. The transition rate is given by

$$\Gamma_{1\to0} = \frac{1}{\hbar^2}|A_{10}|^2 S(\omega_{10}), \tag{4.26}$$

$$\Gamma_{0\to1} = \frac{1}{\hbar^2}|A_{10}|^2 S(-\omega_{10}). \tag{4.27}$$

The dephasing process of a qubit is characterized by Eq. (4.23) when $j = k$. The master equation for this process is given by

$$\dot{\rho}(t) = \Gamma_\varphi\mathcal{L}[\hat{\sigma}_z]\rho(t) \tag{4.28}$$

where the dephasing rate is

$$\Gamma_\varphi = \frac{1}{2\hbar^2}(|A_{11}|^2 + |A_{00}|^2)S(0). \tag{4.29}$$

With the relaxation and dephasing process together, the master equation is given by

$$\dot{\tilde{\rho}}(t) = \begin{pmatrix} -\Gamma_{0\to1}\tilde{\rho}_{00}(t) + \Gamma_{1\to0}\tilde{\rho}_{11}(t) & -\left((\Gamma_{0\to1}+\Gamma_{1\to0})/2 + \Gamma_\varphi\right)\tilde{\rho}_{01}(t) \\ -\left((\Gamma_{0\to1}+\Gamma_{1\to0})/2 + \Gamma_\varphi\right)\tilde{\rho}_{10}(t) & \Gamma_{0\to1}\tilde{\rho}_{00}(t) - \Gamma_{1\to0}\tilde{\rho}_{11}(t) \end{pmatrix}. \quad (4.30)$$

We can easily see that the relaxation process results in damping of the diagonal elements as well as the off-diagonal elements of the density matrix while the dephasing process only leads to damping of the off-diagonal elements. The total damping rate of the off-diagonal elements of the density matrix is known as the total dephasing rate which is given by

$$\Gamma_2 = \frac{\Gamma_{0\to1} + \Gamma_{1\to0}}{2} + \Gamma_\varphi. \quad (4.31)$$

We note that the damping rate is constant in the differential equation (Eq. (4.30)) and therefore the elements of the density matrix should decay exponentially in time domain with time constants as the inverse of the damping rates.

### 4.1.2 Non-Markovian processes

The Born-Markov master equation provides an elegant way to incorporate decoherence into the evolution of a quantum system. However, in many realistic situations the process for $\tilde{f}(t)$ is non-Markovian. As an example, the widely observed $1/f$ noise which exhibits a power spectral density $S(\omega) \propto 1/\omega$ is a non-Markovian process. In these cases, the Born-Markov approximation does not apply since the noise has a correlation to its historical values. In general, a non-Markovian process is very difficult to treat. Here, we will only discuss the dephasing process in a system coupled to classical non-Markovian noise.

We consider a system with longitudinal coupling to a random process $f(t)$ given by the interaction Hamiltonian

$$\tilde{H} = \sum_j |j\rangle\langle j| A_{jj} f(t). \quad (4.32)$$

We note that this is the same Hamiltonian as Eq. (4.6) under the condition $j = k$. Given that $f(t)$ is a classical process, the evolution of the system, from time 0 to $t$, can be described by the unitary transformation

$$U(t) = \sum_i \exp\left[-i\frac{A_{jj}}{\hbar}\int_0^t dt' f(t')\right] |j\rangle\langle j|. \quad (4.33)$$

The density matrix of the system at time $t$, $\tilde{\rho}(t) = U(t)\tilde{\rho}(0)U^\dagger(t)$, can be written as

$$\tilde{\rho}_{jk}(t) = \exp(i\varphi_{jk}(t))\tilde{\rho}_{jk}(0). \quad (4.34)$$

where

$$\varphi_{jk}(t) = \frac{A_{kk} - A_{jj}}{\hbar} \int_0^t dt' f(t'). \tag{4.35}$$

Since $f(t)$ is a random process, the density matrix should be given by the expectation value of all the possible realizations of this process, *i.e.*

$$\tilde{\rho}_{jk}(t) = \langle e^{i\varphi_{jk}(t)} \rangle \tilde{\rho}_{jk}(0). \tag{4.36}$$

To understand the dephasing which is characterized by the damping of the off-diagonal elements of the density matrix, it is required to calculate the quantity $\langle e^{i\varphi_{jk}(t)} \rangle$.

To calculate this quantity, we use an important result in the theory of random processes [38]. For a Gaussian process $f(t)$ with zero average, we have

$$\langle \exp\left[ i \frac{A_{kk} - A_{jj}}{\hbar} \int_0^t dt' f(t') \right] \rangle = \exp\left[ -\frac{|A_{kk} - A_{jj}|^2}{2\hbar^2} \int_0^t dt' \int_0^t dt" \langle f(t') f(t") \rangle \right]. \tag{4.37}$$

Using the property of stationary noise, mentioned earlier in Eq. (4.16), and the relation between the correlation function and the power spectral density (Eq. (4.18)), we derive

$$\langle e^{i\varphi_{jk}(t)} \rangle = \exp\left[ -\frac{|A_{kk} - A_{jj}|^2}{4\pi\hbar^2} t^2 \int d\omega S(\omega) \mathrm{sinc}^2(\omega t/2) \right]. \tag{4.38}$$

From the equation above, we find that the dephasing is in general a non-exponential decay in a non-Markovian process.

For a special case where the noise is a white noise ($S(\omega) = S(0)$), we can simplify Eq. (4.38) using the identity $\int dx \, \mathrm{sinc}^2 x = \pi$. We obtain an exponential decay

$$\langle e^{i\varphi_{jk}(t)} \rangle = \exp\left[ -\frac{|A_{kk} - A_{jj}|^2 S(0)}{2\hbar^2} t \right], \tag{4.39}$$

which is consistent with the results derived from the Born-Markov master equation.

## 4.2 Characterization methods for decoherence of a qubit

In this section, we will discuss characterization methods for the relaxation and dephasing processes of a single qubit. Measuring decoherence is also an effective way of probing

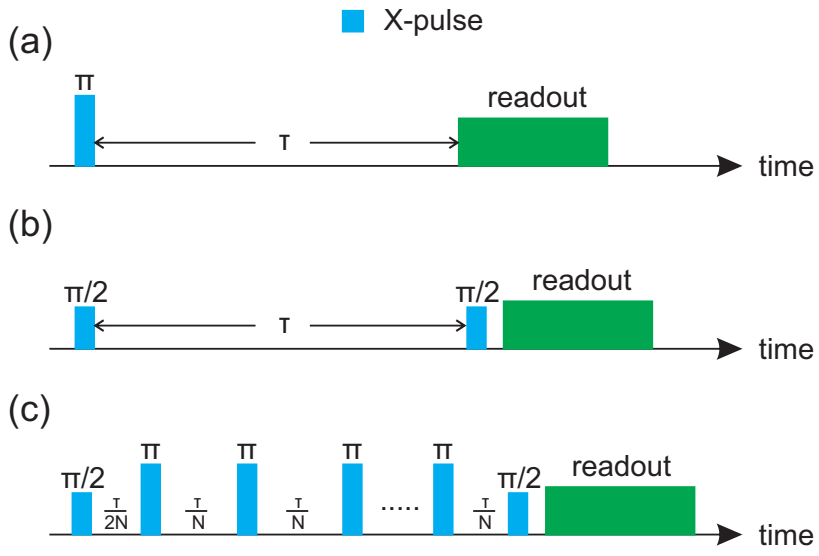



Figure 4.1: **Pulse sequences for decoherence measurement and noise spectroscopy.** Pulse sequences for measuring the energy relaxation time $T_1$ (a), the dephasing time $T_2$ (b), and the noise spectroscopy using dynamical decoupling (c). The blue bars represent the qubit control pulses which correspond to a $\pi$ or $\pi/2$ rotation around the $x$-axis in the Bloch sphere. The green bars represent the readout pulses for qubit state measurements.

the spectral density of the noise environment around the qubit. We will describe a noise spectroscopy method known as dynamical decoupling [39].

Throughout this section, we consider a single qubit coupled to a noisy environment described by Hamiltonian

$$H = -\frac{\nu}{2}\sigma_z + f_z(t)\sigma_z + f_x(t)\sigma_x, \tag{4.40}$$

where $f_z(t)$ and $f_x(t)$ are the random longitudinal and transversal process coupled to the qubit with power spectral density $S_z(\omega)$ and $S_x(\omega)$ respectively.

### 4.2.1 Energy relaxation: $T_1$

The energy relaxation experiment is a method for the longitudinal relaxation time, $T_1$. The value of $T_1$ provides information about the environmental modes at the qubit frequency.

The pulse sequence consists of a single $\pi$-pulse and a certain delay $\tau$ before readout (see Figure 4.1(a)). The $\pi$-pulse brings the qubit from the ground state to the excited state. During the delay, the qubit undergoes longitudinal relaxation until thermal equilibrium is reached. The polarization relaxes from $|1\rangle$ to $|0\rangle$ along the $z$-axis in the process. By measuring the qubit excited state probability at various $\tau$, we thereby record the relaxation dynamics of the qubit.

For the quantum noise [40], $S(\omega) \propto 2\hbar\omega / \left(1 - e^{-\frac{\hbar\omega}{k_B T}}\right)$ at an equilibrium temperature $T$. At low temperature, we have $S(-\omega) \approx 0$ thus the relaxation process is dominated by the rate $\Gamma_{1\to0}$ which will bring the qubit to its ground state. The excited state probability can be expressed as:

$$P_1(\tau) = \exp\left(-\frac{\tau}{T_1}\right), \tag{4.41}$$

where $T_1 = 1/\Gamma_1 = 1/\Gamma_{1\to0}$ is the energy relaxation time. The relaxation rate is related to the noise transversely coupled to the qubit at the qubit frequency $\nu$:

$$\Gamma_1 = \frac{1}{T_1} = \frac{1}{\hbar^2} S_x(\nu). \tag{4.42}$$

### 4.2.2 Ramsey experiment: $T_2$

The Ramsey experiment is a method for measuring the transverse depolarization or the dephasing time $T_2$, during free precession.

The pulse sequence consists of two $\pi/2$-pulses with a certain delay $\tau$ in between and a readout pulse immediately after the second $\pi/2$-pulse. The first $\pi/2$-pulse brings the qubit from the ground state to equatorial plane of the Bloch sphere (see Figure 4.1(b)). During the delay, the qubit undergoes both longitudinal relaxation and transverse depolarization. The second $\pi/2$-pulse brings the remaining polarization back onto the $z$-axis for projective measurement. By measuring the qubit excited state probability at various $\tau$, we thereby measure the decay of the coherence function $\langle e^{i\varphi_{01}(\tau)} \rangle$ thus recording how the qubit dephases.

The total dephasing process can be factorized into depolarization due to the $T_1$ process with an exponential decay and pure dephasing which in general is non-exponential. The excited state probability after the pulse sequence can be expressed as:

$$P_1(\tau) = \exp\left(-\frac{\tau}{2T_1}\right) \exp\left[-\frac{\tau^2}{\pi\hbar^2} \int d\omega S_z(\omega) \mathrm{sinc}^2(\omega\tau/2)\right]. \tag{4.43}$$

For white noise, we have an exponential decay for pure dephasing:

$$P_1(\tau) = \exp\left(-\frac{\tau}{2T_1}\right)\exp\left(-\frac{\tau}{T_\varphi}\right) \tag{4.44}$$

where

$$\Gamma_\varphi = \frac{1}{T_\varphi} = \frac{2}{\hbar^2}S_z(0). \tag{4.45}$$

We define $T_2$ as the total dephasing time by $1/T_2 = 1/(2T_1) + 1/T_\varphi$.

For $1/f$ noise with $S_z(\omega) = A/\omega$, the integral in Eq. (4.43) diverges. By imposing a low frequency cut-off at $\omega_c$, we find a Gaussian decay in the pure dephasing process given by [41]

$$P_1(\tau) = \exp\left(-\frac{\tau}{2T_1}\right)\exp\left(-\frac{\tau^2}{T_\varphi'^2}\right), \tag{4.46}$$

where $T_\varphi' = 1/\sqrt{A\ln(\frac{1}{\omega_c\tau})}$ is the pure dephasing time.

### 4.2.3 Noise spectroscopy with dynamical decoupling

Given the low-frequency noise coupled to the qubit is correlated, the dephasing during the free precession in the Ramsey experiments can be partially reversed by applying refocusing pulses [42, 43, 44]. This technique by means of increasing the dephasing time is known as dynamical decoupling and has been widely used in the NMR systems.

In Figure 4.1(c), we show one dynamical decoupling pulse scheme known as the CP pulse sequence which was proposed by Carr and Purcell in 1954 [45]. The pulse sequence is similar to the Ramsey pulse sequence. Besides, two $\pi/2$-pulses spaced by $\tau$, additional $N$ $\pi$-pulses are inserted to the free precession period with equal spacing. However, the $\pi$-pulse, also known as the refocusing pulse, makes the dynamics different from free precession. To understand the principle, we take the case for $N = 1$ which is originally known as the spin-echo pulse sequence [46]. After the first $\pi/2$-pulse, the qubit undergoes dephasing during the first half of the free precession period. The $\pi$-pulse reverses the sign of the noise seen by the qubit in the second half of the free precession. Using such a pulse sequence, noise with long correlation time will effectively cancel itself thus the pure dephasing time can be enhanced.

Moreover, the dynamical decoupling technique provides a means to measure the spectral density of the qubit's environment. The result can be derived by the filter function

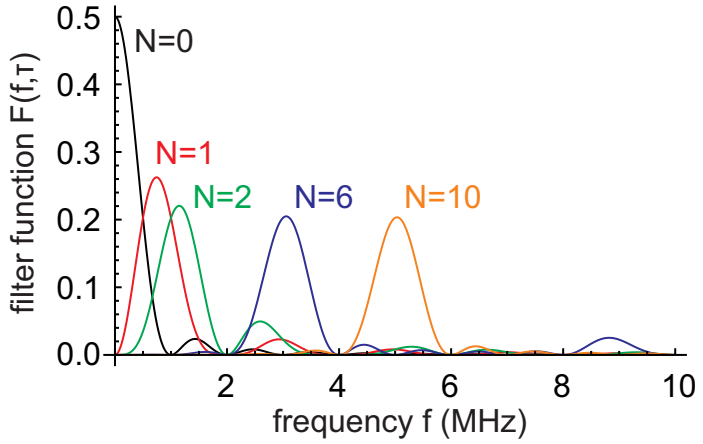



Figure 4.2: **Filter functions of the CP pulse sequence.** We show the filter functions with different numbers of $\pi$-pulse for equal precessing time $\tau = 1$ $\mu$s.

method [47, 48] in which the coherence function describing the pure dephasing process is a weighted integral over the noise spectrum:

$$\langle e^{i\varphi_{01}(\tau)} \rangle = \exp\left[ -\frac{\tau^2}{\pi\hbar^2} \int_0^\infty d\omega S_z(\omega) F_N(\omega, \tau) \right]. \tag{4.47}$$

The weighting function $F_N(\omega, \tau)$ is called the filter function, and is determined by the pulse sequence. For a CP pulse sequence, the filter function is given by [49]

$$F_N(\omega, \tau) = \frac{1}{(\omega\tau)^2} \left| 1 + (-1)^{1+N} \exp(i\omega\tau) + 2\sum_{j=1}^{N} (-1)^j \exp(i\omega\delta_j\tau) \cos(\omega\tau_\pi/2) \right|^2, \tag{4.48}$$

where $\tau$ is the total free precession time, $N$ is the number of $\pi$ pulses, and $\tau_\pi$ is the duration of each $\pi$-pulse. We note that these filter functions have a main peak around $\omega_0 \approx \pi N/\tau$ (see Figure 4.2). If the power spectral density $S_z(\omega)$ is relatively flat around the peak position of the filter function, Eq. (4.47) can be written as

$$S_z(\omega_0) = \frac{-\pi\hbar^2}{\tau^2 \int_0^\infty d\omega F_N(\omega, \tau)} \ln\langle e^{i\varphi_{01}(\tau)} \rangle. \tag{4.49}$$

Using this equation, we can infer the amplitude of the noise at a frequency $\omega_0$ from the measured coherence function of the qubit $\langle e^{i\varphi_{01}(\tau)} \rangle$. In principle, we can effectively sample the environmental noise $S_z(\omega)$ by varying the number of pulses $N$ and the total sequence time $\tau$.

## 4.3 Decoherence of resonators

The dominating decoherence channel for a quantum harmonic oscillator is found to be the energy relaxation, *e.g.* the photon loss in a microwave resonator [50]. We model this loss by assuming a coupling Hamiltonian between the resonator and its environment $H_{\mathrm{SE}} = (a^\dagger + a)f$, with $f$ a degree of freedom in the environment. With this assumption, the master equation under the Born-Markov approximation can be written as:

$$\dot{\rho}(t) = -\frac{i}{\hbar}[H, \rho(t)] + \Gamma_\downarrow \mathcal{L}[a]\rho(t) + \Gamma_\uparrow \mathcal{L}[a^\dagger]\rho(t), \tag{4.50}$$

where $H = \hbar\omega(a^\dagger a + 1/2)$ is the Hamiltonian of the resonator, $\mathcal{L}[a]$ is the Lindblad superoperator, and $\Gamma_\uparrow$ and $\Gamma_\downarrow$ are the rates of a photon "jumping" up and down the Fock state ladder respectively. In the thermal environment with a low equilibrium temperature, we usually have $\Gamma_\uparrow \approx 0$ thus the resonator will relax to the ground state at a rate $\kappa = \Gamma_\downarrow$. In this case, the population of the Fock state $|n\rangle$ decays at a rate $n\kappa$ which provides a way to measure the coherence time of a resonator.

However, preparing and measuring Fock states in a harmonic resonator are non-trivial tasks in experiments. In practice, the energy relaxation rate of a resonator can be obtained through probing its steady state response to continuous-wave photons in a coherent state. This measurement can be understood by the input-output theory for quantum fields [40]. This theory, based on the quantum Langevin equation is closely related to the master equation approach, however the former one focuses more on the dynamics of the quantum field interacting with the system, which provide grounds to analyze decoherence and quantum measurements.

Following the treatment in Ref. [51], we will now apply it to the case of a resonator coupled through both of its ports as shown in Figure 4.3(a). The field in a transmission line contains a continuum of modes, and thus is described as a environment with creation and annihilation operators which satisfy $[b_i^\dagger(\omega), b_i(\omega')] = \delta(\omega - \omega')$ with $i = 1, 2$ the port number. In the rotating wave approximation, the linear coupling between the internal modes and the external modes at port $i$ is described by a term in the Hamiltonian

$$H_{\mathrm{C}i} = \int d\omega \sqrt{\frac{\kappa_i}{2\pi}} \left[ b_i(\omega) a^\dagger - b_i^\dagger(\omega) a \right], \tag{4.51}$$

where $a^\dagger$ and $a$ are the creation and annihilation operators of the resonator mode and $\kappa_i$ is the coupling strength between the resonator and the environment modes at port $i$.

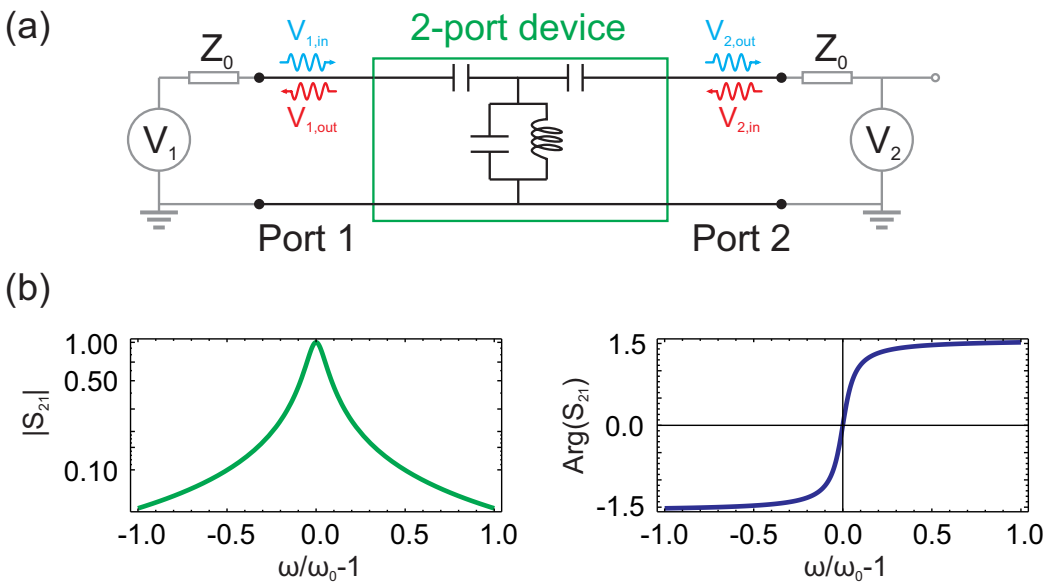



Figure 4.3: **Transmission measurements of a resonator.** (a) Schematic of transmission measurements of a two port resonator. (b) Amplitude and phase of the scattering matrix of the resonator.

The equation of motion for the environmental modes is given by

$$\dot{b}_i(\omega) = -i\omega b_i(\omega) + \sqrt{\frac{\kappa_i}{2\pi}} a. \tag{4.52}$$

The solution of this equation can be written into two ways depending on the boundary conditions. If we impose an initial condition $b_{i,\text{init}}(\omega)$ at time $t_0 < t$, a situation which corresponds to sending an incoming wave to the resonator, the solution is given by

$$b_i(\omega) = e^{-i\omega(t-t_0)} b_{i,\text{init}}(\omega) + \sqrt{\frac{\kappa_i}{2\pi}} \int_0^t dt' a(t') e^{-i\omega(t-t')}. \tag{4.53}$$

If we impose a final condition $b_{i,\text{final}}(\omega)$ at time $t_1 > t$, a situation which corresponds to getting an output wave from the resonator, the solution is given by

$$b_i(\omega) = e^{-i\omega(t-t_t)} b_{i,\text{final}}(\omega) - \sqrt{\frac{\kappa_i}{2\pi}} \int_t^{t_1} dt' a(t') e^{-i\omega(t-t')}. \tag{4.54}$$

The equation of motion for the resonator operator is given by

$$\dot{a} = -\frac{i}{\hbar}[H, a] - \sum_i \sqrt{\frac{\kappa_i}{2\pi}} \int d\omega b_i(\omega) - \frac{\kappa_0}{2} a, \tag{4.55}$$

where we add an extra damping term $-\kappa_0 a/2$ to include the intrinsic energy relaxation of the resonator. By defining the input and output field operators as

$$a_{\text{in},i}(t) = \frac{-1}{\sqrt{2\pi}} \int d\omega b_{i,\text{init}}(\omega) e^{-i\omega(t-t_0)}, \tag{4.56}$$

$$a_{\text{out},i}(t) = \frac{1}{\sqrt{2\pi}} \int d\omega b_{i,\text{final}}(\omega) e^{-i\omega(t-t_1)}, \tag{4.57}$$

we find the relations between the input, output, and intra-resonator fields (using Eq. (4.52) and (4.55)) to be

$$\dot{a}(t) = -\frac{i}{\hbar}[H, a(t)] + \sum_{i=1}^{2} \sqrt{\kappa_i} a_{\text{in},i}(t) - \left( \sum_{i=0}^{2} \frac{\kappa_i}{2} \right) a(t), \tag{4.58}$$

$$a_{\text{out},i}(t) + a_{\text{in},i}(t) = \sqrt{\kappa} a(t). \tag{4.59}$$

Physically these input and output fields are of the same nature as the forward propagating and backward propagating waves in the transmission lines. We can connect them to the scattering-matrices [24]

$$S_{ij} = \frac{a_{\text{out},i}}{a_{\text{in},j}}, \tag{4.60}$$

which can be directly measured using a vector network analyzer (VNA) in experiments.

For deriving the form of the scattering-matrices, we assume classical fields therefore we can replace the creation and annihilation operators by complex amplitudes of the coherent states $\alpha_{\text{in/out},i}$. For transmission measurements where the incoming signal is only on port 1, the equation for intra-resonator field derived from Eq. (4.58) is given by

$$\dot{\alpha}(t) = -i\omega_{\text{r}} \alpha(t) - \sum_{i=0}^{2} \frac{\kappa_i}{2} \alpha(t) + \sqrt{\kappa_1} \alpha_{\text{in},1}(t). \tag{4.61}$$

The steady state solution of this equation is

$$\alpha(\omega) = \frac{2\sqrt{\kappa_1}}{\sum_{i=0}^{2} \kappa_i - 2i(\omega - \omega_{\text{r}})} \alpha_{\text{in},1}(\omega). \tag{4.62}$$

Using Eq. (4.59) we calculate the transmission from one port to the other given by the scattering matrix $S_{21}$ as

$$S_{21}(\omega) = \frac{\alpha_{\mathrm{out},2}(\omega)}{\alpha_{\mathrm{in},1}(\omega)} = \frac{2\sqrt{\kappa_1\kappa_2}}{\sum_{i=0}^{2}\kappa_i - 2i(\omega - \omega_{\mathrm{r}})}. \tag{4.63}$$

In this case, the transmission signal of the resonator is a Lorentzian function (see Figure 4.3(b)). The total relaxation rate $\kappa = \sum_i \kappa_i$ is given by the 3 dB bandwidth of the Lorentzian peak on the amplitude of the scattering matrix. If the two ports of the resonator have the same coupling, *i.e.* $\kappa_1 = \kappa_2 = \kappa_{\mathrm{e}}/2$, we can obtain the external relaxation rate $\kappa_{\mathrm{e}}$ as well as the intrinsic relaxation rate $\kappa_0$ by measuring the height of the Lorentzian peak which is given by $\kappa_{\mathrm{e}}/(\kappa_{\mathrm{e}} + \kappa_0)$.

# Part I

# Fast control of a superconducting qubit with strong driving

# Chapter 5

# Observation of Floquet states in a strongly driven superconducting qubit

Monochromatic driving is the most common tool in quantum control, applicable to various physical systems including nuclear and electronic spins, atoms, ions, superconducting qubits, and quantum dots [52]. For driving that is weak compared to the relevant transition frequency, the dynamics can be described in terms of Rabi oscillations between energy eigenstates. In contrast, with strong driving the commonly used rotating wave approximation (RWA) [53] breaks down, resulting in complex evolution. Strong driving dynamics is most adequately described in the framework of Floquet theory [35], where the state of a driven system is expressed in terms of quasienergies and quasienergy states. Exploring this more general framework expands the field of quantum control, gaining increasing relevance as current experiments on the implementation of high-fidelity quantum gates [54] and protection against decoherence [55] are performed with a driving strength that is a significant fraction of the transition frequency. In addition, strong driving is relevant in the fields of quantum sensing, for phase measurements [56], and quantum simulations, for designing effective Hamiltonians in the emerging field of Floquet engineering [57].

In this chapter, we report experiments on the dynamics of an artificial atom, a superconducting quantum bit [58, 14], strongly driven by a microwave field. Strong driving has been studied in the field of atomic physics, using either optical [59] or radio-frequency

[1]The work described in this chapter has been submitted to Phys. Rev. Lett. to be considered for publication.

pulses [56]. In experiments with NV centers in diamond, time dynamics was observed for driving strength up to values comparable to the transition frequency [60]. Superconducting qubits display a naturally strong coupling to electromagnetic fields due to their mesoscopic character. Previous experiments on strong driving of superconducting qubits addressed the steady state response to continuous waves [61, 62, 11, 63, 64, 65, 66, 67, 68, 69, 70]. In our experiments, we explore driving with short pulses and a driving strength significantly exceeding the transition frequency. The observed system dynamics is well described in terms of quasienergies and quasienergy states, as predicted by Floquet theory. We find that the switching on and off of the driving pulse plays an important role in the qubit evolution, as determined by adiabaticity conditions in the Floquet picture [71]. We also used strong driving for fast, sub-nanosecond, preparation of qubit states.

## 5.1 Experimental platform

The artificial atom in our experiment is a superconducting flux qubit [22]. Among the different types of superconducting qubits, flux qubits have the advantage of high-level anharmonicity, leading to ideal two-level system behavior, and of strong coupling to electromagnetic fields [13, 12] which enable strong driving. Qubit state measurement is performed by probing microwave transmission through a resonator coupled to the qubit (see Fig. 5.1(a)), in the dispersive regime of circuit quantum electrodynamics [29].

The qubit Hamiltonian is given by $H(t) = -\frac{\hbar\Delta}{2}\sigma_z - \frac{\hbar\epsilon(t)}{2}\sigma_x$ in a basis formed by symmetric and antisymmetric combinations of clockwise and anticlockwise persistent current states in the qubit loop [22]. Here $\Delta$, the minimum energy level splitting, is a fixed parameter, and $\epsilon(t) = 2I_p(\Phi(t) - \Phi_0/2)$, with $\Phi(t)$ the magnetic flux applied to the loop dependent on the time $t$. The magnetic flux $\Phi(t) = \Phi_s + \Phi_d(t)$ with $\Phi_s$ a static flux generated by a superconducting coil and $\Phi_d(t)$ a time-varying magnetic flux coupled to the qubit through a waveguide terminated by an antenna (see Fig. 5.1(a)). The usual approach employed to generate control pulses is based on using a modulator to shape the quadratures of a continuous wave produced by a frequency synthesizer. Here we use instead a new generation of high-speed arbitrary waveform generator (AWG) to directly synthesize the microwave pulses (see Section 2.5), leading to the time accuracy required for control with subnanosecond resolution pulses.

A plot of the qubit transition frequency versus the static flux $\Phi_s$, obtained by spectroscopy with weak and long microwave pulses, is shown in Fig. 5.1(c). All the experiments reported in this Letter are performed at the symmetry point ($\Phi_s = \Phi_0/2$), where the qubit transition frequency $\omega_{01} = \Delta = 2\pi \times 2.288$ GHz. We use amplitude shaped pulses

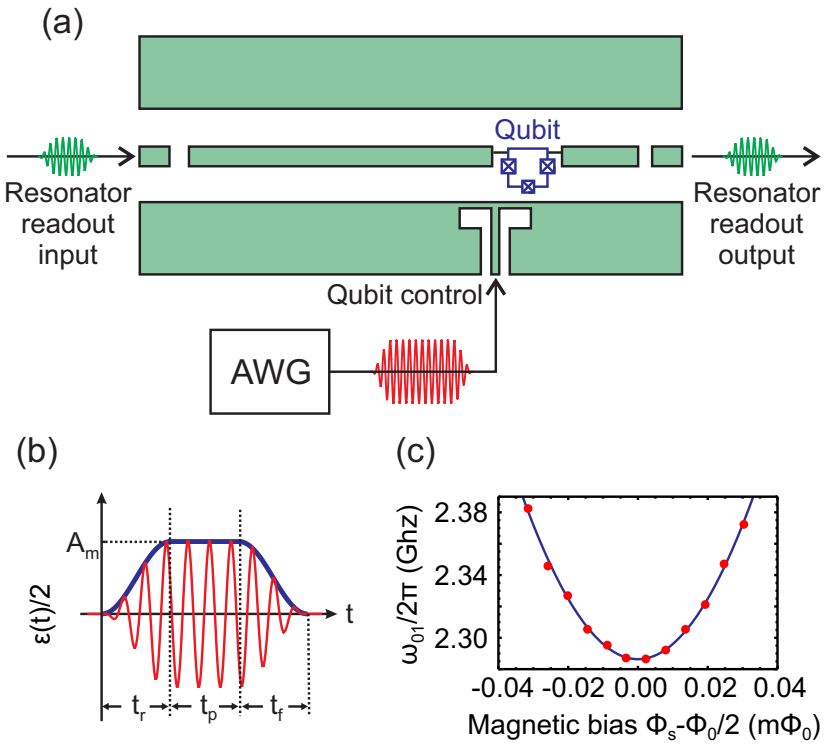



Figure 5.1: **Qubit control, readout, and spectroscopy.** (a) Schematic representation of the experimental setup. The qubit, formed by a superconducting loop interrupted by Josephson junctions (cross symbols), is coupled to a superconducting coplanar waveguide resonator. Readout is based on the transmission of a microwave pulse from the resonator input (left) to its output port (right). A waveguide (bottom) is used to couple microwave control pulses to the qubit. (b) Representation of qubit control pulses, with rise and fall times $t_\mathrm{r}$ and $t_\mathrm{f}$ respectively, and maximum amplitude duration $t_\mathrm{p}$. The thick line indicates the pulse envelope, which reaches a maximum $A_\mathrm{m}$. During rise and fall, the envelope is shaped as $\frac{A_\mathrm{m}}{2}\left(1-\cos\left(\pi t/t_\mathrm{r}\right)\right)$ and $\frac{A_\mathrm{m}}{2}\left(1+\cos\left(\pi(t-t_\mathrm{p}-t_\mathrm{r})/t_\mathrm{f}\right)\right)$. (c) Qubit transition frequency $\omega_{01}$ from spectroscopy measurements versus the static magnetic flux $\Phi_\mathrm{s}$. The continuous line is a fit of the transition frequency, yielding the parameters $\Delta = 2\pi \times 2.288$ GHz and $I_p = 690$ nA.

$\epsilon(t) = 2A(t)\cos(\omega t)$, with $A(t)$ characterized by a maximum amplitude $A_{\rm m}$ and rise and fall times denoted by $t_{\rm r}$ and $t_{\rm f}$ respectively (see Fig. 5.1(b)). At the symmetry point, the energy relaxation and pure dephasing times are given by $T_1 = 1.8$ $\mu$s and $T_{\rm Ramsey} = 0.3$ $\mu$s. These coherence times, currently limited by quasiparticle tunneling, microscopic two-level systems, and charge noise [72, 73], can be further improved by infrared shielding techniques and improved qubit design without impairing the ability to strongly drive the qubit.

## 5.2 Rabi oscillations in strong driving regime: a measurement of quasienergies

Experiments are performed by repeating, typically 16,384 times, a sequence formed of state reset, control using an applied pulse, and measurement in the energy eigenbasis. Figure 5.2(a) shows the qubit's average excited state probability versus the duration of the microwave pulse, with driving on resonance. The waveform is defined with zero rise and fall times, however, the actual rise and fall times are determined by the analog bandwidth of the AWG and are specified to be shorter than 22 ps (see Section 2.5). For weak driving (Fig. 5.2(a) top panel), sinusoidal oscillations are obtained, as predicted based on the rotating wave approximation. With a large Rabi driving strength (Fig. 5.2(a) bottom panel), large amplitude oscillations are accompanied by smaller amplitude faster oscillations, a signature of non-negligible counter-rotating term effects. The different frequency components are clearly visible in the Fourier transform of the signal (Fig. 5.2(b)). For a wide range of the driving strength $A_{\rm m}$, from $2\pi\times0.20$ GHz to $2\pi\times4.78$ GHz, the Fourier transformed data is shown in Fig. 5.3(a).

The presence of the various frequency components in the Rabi oscillations can be understood based on Floquet theory, which predicts that for a time-periodic Hamiltonian with period $T$ the quantum state is given by $|\psi(t)\rangle = \sum_{j=0,1} c_j e^{-i\epsilon_j t}|u_j(t)\rangle$ with $\epsilon_j$ the quasienergies and $|u_j(t)\rangle$ the quasienergy states, periodic in time with period $T$. As a result, the probability to find the system in its excited state is expected to show oscillatory behavior with frequency components $n\omega$ and $\pm\Delta\epsilon + n\omega$, with $\Delta\epsilon$ the quasienergy difference, $\omega = 2\pi/T$ the driving frequency, and $n$ any integer number. The harmonic drive signal used in our experiment has the additional symmetry $\epsilon(t + T/2) = -\epsilon(t)$, and as a result only components with even $n$ values are present [74]. Fig. 5.3(b) shows the extracted frequency components versus driving amplitude. We compare the experimental results with calculations of the quasienergies based on numerical simulations (solid lines) and an analytical expression (dashed lines). The latter, obtained based on approximate diagonalization after transformation to a rotating frame [75], gives a quasienergy difference

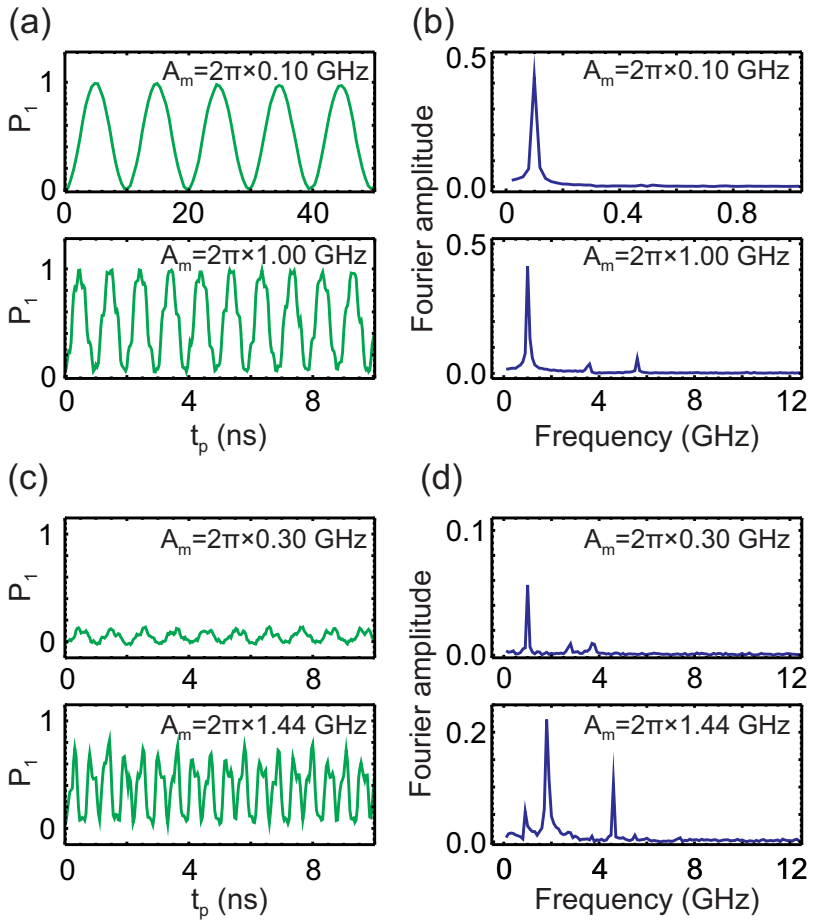



Figure 5.2: **Coherent oscillations versus driving amplitude for resonant driving ($\omega = \Delta$, (a-b)) and off-resonance driving ($\omega = 0.6 \times \Delta$, (c-d))**. (a,c) Qubit excited state probability $P_1$ versus control pulse duration $t_\mathrm{p}$ for $A_\mathrm{m} = 0.10$ and 1.00 GHz (a) and $A_\mathrm{m} = 0.30$ and 1.44 GHz (c). (b,d) Discrete Fourier transforms of the oscillations in (a) and (c) respectively.

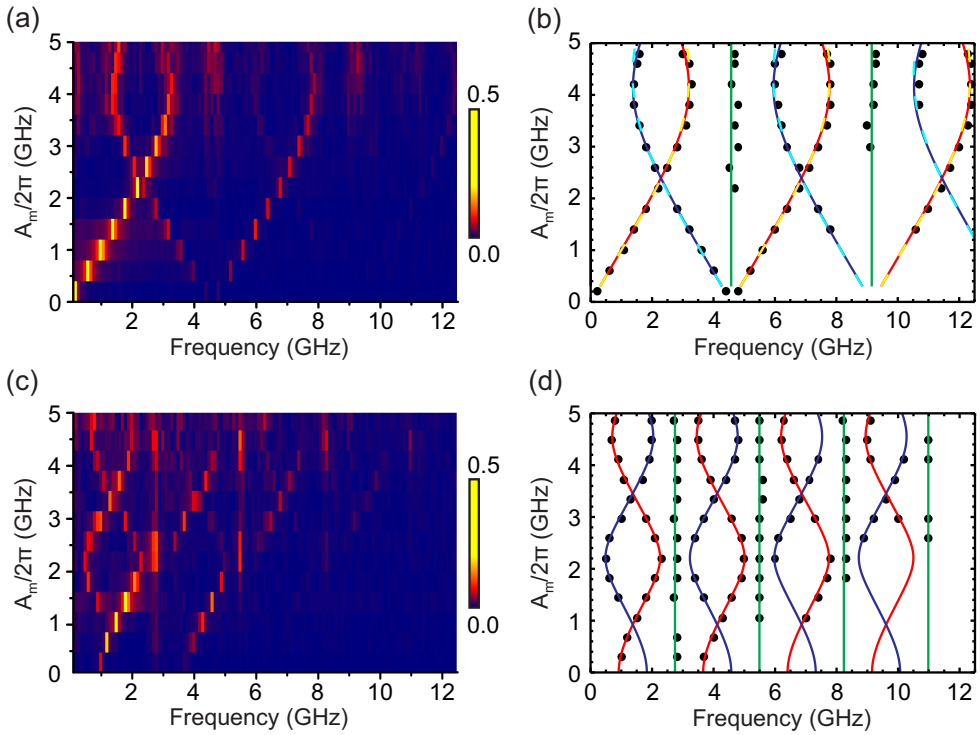



Figure 5.3: **Oscillation frequencies of the qubit population versus driving amplitude for resonant driving ($\omega = \Delta$, (a-b)) and off-resonance driving ($\omega = 0.6 \times \Delta$, (c-d))**. (a,c) Color plot of the Fourier transform of population oscillations versus frequency and driving pulse amplitude. (b,d) Positions of peaks in the Fourier transform of coherent oscillations versus driving amplitude extracted from the data in (a) and (c) (dots). The lines are plots of $n\omega$, $n\omega - \Delta\epsilon$, and $n\omega + \Delta\epsilon$ respectively, with the quasienergy difference $\Delta\epsilon$ determined numerically and $n$ an even integer. For the resonant driving case (b) we show in addition corresponding curves (dashed) based on the analytical approximation for $\Delta\epsilon$ discussed in the text.

$\Delta\epsilon = \omega\sqrt{\left(1 - J_0\left(\frac{2A}{\omega}\right)\right)^2 + J_1^2\left(\frac{2A}{\omega}\right)}$, with $J_{0/1}$ Bessel functions of the first kind and order 0/1. This formula provides a good approximation for the case of a two-level system biased at its symmetry point and driven on or near resonance with arbitrary strength, complementing previous theoretical work where the weak- and strong-driving limits of this formula had been derived [69, 70]. Additional experiments were performed with the qubit driven off-resonance, with a driving frequency $\omega = 2\pi \times 1.373$ GHz (see Fig. 5.2(c) and (d)). The Fourier transform of the qubit population signal and the identified frequency components are shown in Figs. 5.3(c) and (d) respectively. Good agreement with the predictions of numerical calculations is observed in this case as well (see Fig. 5.3(d)).

## 5.3 Quantum state tomography for Floquet dynamics

Tomography experiments confirm the role of the counter-rotating terms in the driven evolution of the qubit. Fig. 5.4 shows results of state tomography versus the duration of driving pulses for two values of the driving amplitude, $A_{\rm m} = 2\pi \times 0.10$ GHz and $A_{\rm m} = 2\pi \times 0.46$ GHz, and zero rise and fall times. For both values of the driving amplitude, high-amplitude oscillations are observed, with a period corresponding to the quasienergy difference. In the weak driving limit, these oscillations are the usual Rabi oscillations. High-frequency components are observed in addition, with a significant amplitude at strong driving, reflecting the presence of the non-negligible counter-rotating wave component. The results of tomography experiments are in very good agreement with predictions of numerical simulations of the Schrödinger equation (see Fig. 5.4).

## 5.4 Turn-on/-off effects of the pules

The presence of the fast oscillatory terms in the driven evolution depends not only on the pulse amplitude, but also on the pulse turn-on and turn-off times. Fig. 5.5(a) shows qubit state oscillations for a driving strength $A_{\rm m} = 2\pi \times 1.33$ GHz, and different rise and fall times. Fast oscillatory terms are gradually suppressed as the turn-on and -off times are increased. We emphasize that fast oscillatory components in the oscillations are completely suppressed for slow pulse turn-on and -off despite the fact that during most of the driven evolution the driving amplitude is comparable with the transition frequency. The absence of fast oscillations for slow turn-on and -off can be understood based on adiabaticity in the Floquet picture [71]. Indeed, the time-dependent qubit state can be written, up to an overall phase and a geometric phase, as $|\psi(t)\rangle = c_0(t)|u_0(A,t)\rangle + c_1(t)e^{-i\int_0^t \Delta\epsilon(t)\mathrm{d}t}|u_1(A,t)\rangle$, with

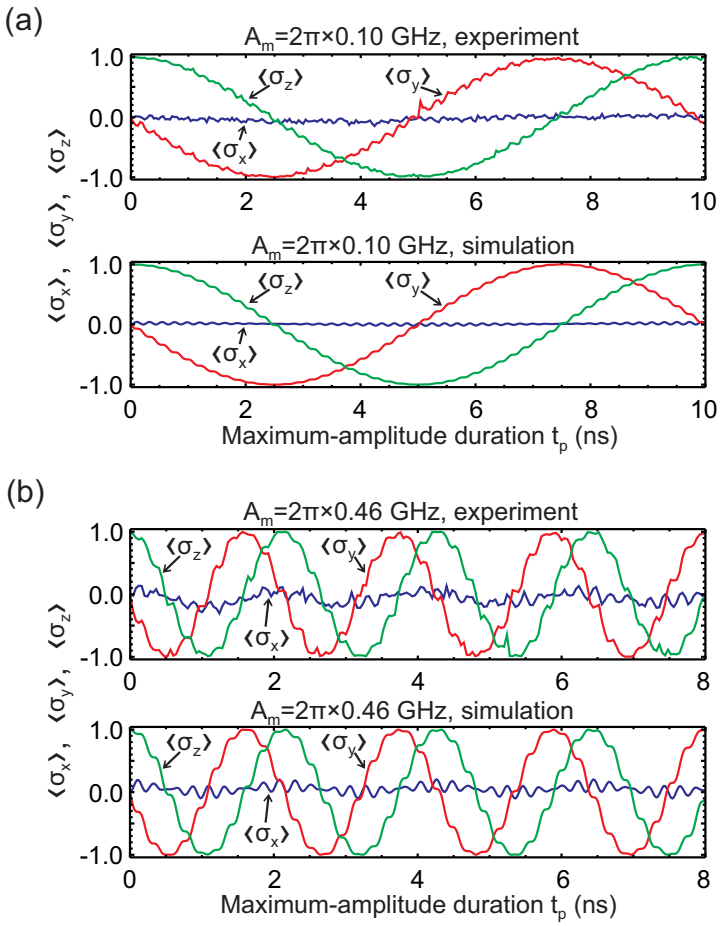



Figure 5.4: **Quantum state tomography of the time-resolved Floquet state dynamics.** Measurements and simulations of the evolution of the Bloch vector components, given by the average values of the Pauli $\sigma_\alpha$ ($\alpha = x, y, x$) operators, after a pulse defined on the AWG with zero rise and fall time, versus the length of the pulse for $A_\mathrm{m} = 2\pi{\times}0.10$ GHz (a) and $A_\mathrm{m} = 2\pi{\times}0.46$ GHz (b). The experimental results are in excellent agreement with the results of numerical simulations.

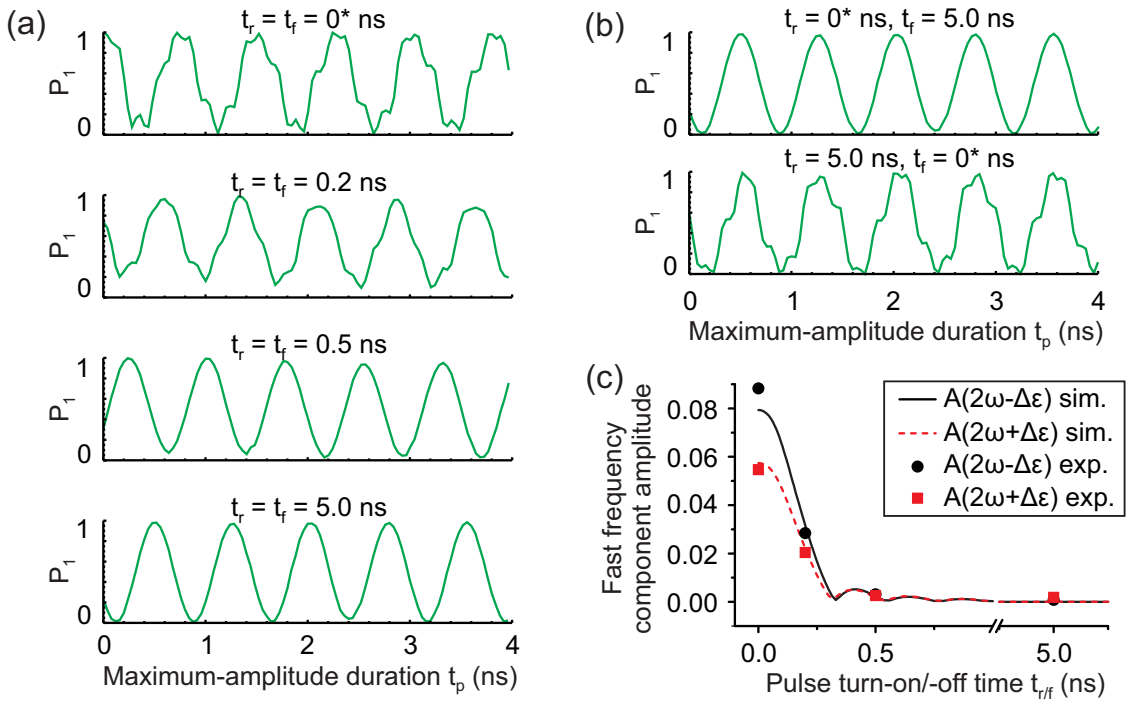



Figure 5.5: **Coherent oscillations versus the pulse turn-on and turn-off times.** (a,b) Qubit excited state probability $P_1$ versus pulse duration $t_\mathrm{p}$ for various rise (fall) times $t_\mathrm{r}$ ($t_\mathrm{f}$) and equal maximum amplitude $A_\mathrm{m} = 2\pi \times 1.33$ GHz. Panel (a)/(b) shows data with symmetric/asymmetric rise and fall. (c) The measured (dots and squares) and simulated (continuous and dashed lines) fast oscillation amplitudes, at frequencies $2\omega - \Delta\epsilon$ and $2\omega + \Delta\epsilon$ respectively. * The actual rise/fall time is around 20 ps, determined by the analog bandwidth of the AWG.

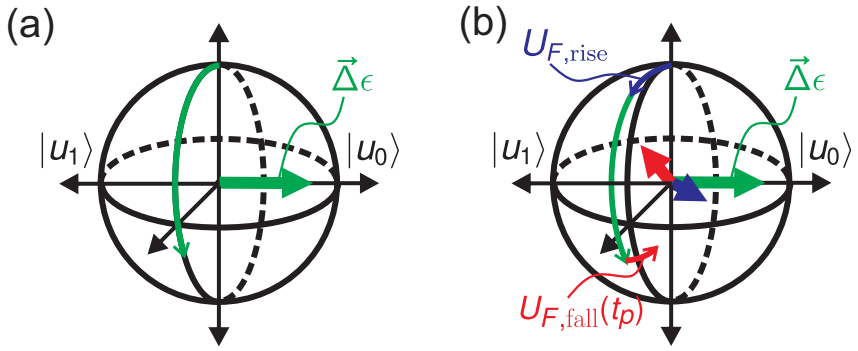



Figure 5.6: **Adiabatic (a) and nonadiabatic (b) evolution in the Floquet picture.** The state is represented on the Bloch sphere, with a basis chosen such that the instantaneous quasienergy states $|u_{0,1}\rangle$ are in the equatorial plane. The state vector evolution (thin arrows) is a rotation around a fictitious field (thick arrows). The initial qubit state is $(|u_0\rangle + |u_1\rangle)/\sqrt{2}$. In the adiabatic case (a), the state evolution is described by a phase $-\int_0^t \Delta\epsilon(t)\mathrm{d}t$ applied to $|u_1\rangle$, which is equivalent to rotation around the fictitious field $\vec{\Delta}\epsilon(t)$ aligned with $|u_0\rangle$. In this picture, the evolution of the qubit is a simple rotation, although in the energy eigenbasis the qubit undergoes complex dynamics. In the nonadiabatic case (b), transitions between Floquet states arise during pulse turn-on and turn-off, characterized by the unitary transformations $U_{F,\mathrm{rise}}$ and $U_{F,\mathrm{fall}}$ respectively, which correspond in general to rotations around axes that are not parallel to $\vec{\Delta}\epsilon(t)$.

$|u_0(A,t)\rangle$ and $|u_1(A,t)\rangle$ the instantaneous driving-amplitude-dependent quasienergy states. The initial values of the coefficients $c_0$ and $c_1$ are determined by the representation of the initial qubit state, which is the ground state, in the basis formed by the states $|u_{0,1}(0,0)\rangle = (|0\rangle \pm |1\rangle)/\sqrt{2}$, with $|0\rangle(|1\rangle)$ the ground/excited state of the qubit (see Appendix D). For slowly varying driving amplitude $A(t)$, the evolution is adiabatic in the Floquet basis, and therefore the coefficients $c_0$ and $c_1$ maintain their initial values. The dynamics of the qubit in this case, using the Bloch sphere representation (see Fig. 5.6(a)), can be understood by the rotation of the pseudo-spin representing the state around a fictitious field determined at any given time by the difference $\Delta\epsilon$ between the quasienergies. Similarly to the weak driving case, the qubit simply undergoes a Rabi rotation between the ground and excited states, with a rotation angle given by $1/2\int_0^t \Delta\epsilon(t)\mathrm{d}t$.

With short rise and fall times, the evolution of the qubit at the beginning and end of the pulse is non-adiabatic in the Floquet representation. Non-adiabatic effects can be

described by unitary transformation $U_{F,\text{rise}}$ and $U_{F,\text{fall}}$ at the beginning and the end of the pulse respectively (see Fig. 5.6(b)). The latter depends periodically on the pulse duration with period $T$, leading to fast oscillations of the final state of the qubit. For a driving amplitude $A_\text{m} = 2\pi \times 1.33$ GHz, the qubit population dynamics is well described by a sum of oscillatory terms at frequencies $\Delta\epsilon$, $2\omega + \Delta\epsilon$, and $2\omega - \Delta\epsilon$. In Fig. 5.5(c) we plot the amplitude of the high-frequency components, at $2\omega \pm \Delta\epsilon$, versus the pulse rise and fall time. The experimental results are in good agreement with values extracted based on numerical simulations of the qubit evolution.

In additional experiments (see Fig. 5.5(b)), we observed the evolution of the qubit with strong pulses and asymmetric rise and fall times. The final state of the qubit displays fast oscillations for pulses with slow rise and fast fall, whereas fast oscillations are absent for pulses with fast rise and slow fall. This observation confirms the asymmetric role of the two rotations, $U_{F,\text{rise}}$ and $U_{F,\text{fall}}$.

## 5.5 Fast quantum operations

We next discuss the use of strong driving for fast quantum gates, specifically qubit state preparation. Starting with the qubit in its ground state, we apply pulses with a driving strength $A_m = 2\pi \times 0.46\,\text{GHz}$ and rise and fall times of approximately 20 ps, defined by the AWG bandwidth. The state $(|0\rangle - i|1\rangle)/\sqrt{2}$ is prepared in 0.48 ns with a fidelity of $0.9996 \pm 0.0006$ (see Appendix C). Similarly, state $|1\rangle$ is prepared in 1.08 ns with a fidelity of $0.9969 \pm 0.0008$. We have performed numerical simulations of state evolution, which predict state preparation fidelities of 0.9997 and 0.9976 for states $(|0\rangle - i|1\rangle)/\sqrt{2}$ and $|1\rangle$ respectively, in good agreement with the experimental result.

## 5.6 Conclusions

Our work demonstrates the feasibility of using strong driving for the control of superconducting artificial atoms. The dynamics was analyzed in the framework of Floquet theory. The consideration of adiabaticity in the Floquet picture provides a valuable viewpoint on dynamics, applicable well beyond the regime where the rotating wave approximation holds. Our experimental demonstration brings very exciting prospect for experiments addressing the interplay between Floquet dynamics and environmental effects [76, 77]. We expect that our results will stimulate new work across a broad range of fields including quantum computing, open system dynamics, quantum simulations, and quantum sensing.

# Chapter 6

# Optimization of single-qubit operations in the strong driving regime

In the previous chapter, we discussed how the fast oscillatory components in the qubit dynamics is related to nonadiabatic transitions between Floquet states. By turning on/off the pulse slowly (or adiabatically), we can suppress the fast components and retain the simple Rabi oscillation between the energy eigenstates. In this chapter, we propose a pulse scheme for fast single-qubit operations, which involves coherent control of the nonadiabatic transitions by pulse shaping.

In the first section, we will introduce the adiabatic perturbation theory as a useful tool to analyze nonadiabatic dynamics in the Floquet picture. In the second section, we will quantitatively determine the nonadiabatic transitions in amplitude-modulated pulses using first order adiabatic perturbation theory. We verify these results by comparing them with numerical simulations. In the third section, we will present a pulse modulation scheme based on coherent suppression of the nonadiabatic transitions between the Floquet states of a driven qubit. This pulse scheme allows for high-fidelity single-qubit operations on a short timescale.

## 6.1 Adiabatic perturbation theory in the Floquet picture

We start from the general Schrödinger equation of a time-dependent Hamiltonian problem:

$$i\frac{d}{dt}|\psi(t)\rangle = H(t)|\psi(t)\rangle. \tag{6.1}$$

Here we consider a Hamiltonian consisting of time-dependent functions with two different time scales: 1. functions varying rapidly and periodically in time; 2. functions depending on parameters varying slowly in time. We can label the slow part of the Hamiltonian as functions of a parameter $A$ which is time dependent. The Hamiltonian can be written as a two-variable operator $\tilde{H}(A,t)$ where $\tilde{H}(A(t),t) = H(t)$. For example, the Hamiltonian of a pulse-driven two-level system at its symmetry point can be written as:

$$H(t) = \tilde{H}(A(t),t) = -\frac{\Delta}{2}\sigma_z + A(t)\cos(\omega t+\phi)\sigma_x, \tag{6.2}$$

where $A(t)$ denotes the slow varying envelope of the pulse and $\cos(\omega t+\phi)$ is the fast periodic part. Before we address the specific Hamiltonian in Eq. (6.2), we will first give a general treatment to this type of problem. Following the treatment in Ref. [71, 78], we introduce a wave function $|\tilde{\psi}(A,t)\rangle$ which depends on the two parameters $A$ and $t$. The physical wavefunction is given by $|\psi(t)\rangle = |\tilde{\psi}(A(t),t)\rangle$.

Using the chain rule, the Schrödinger equation with respect to the new wavefunction $|\tilde{\psi}(A,t)\rangle$ can be written as:

$$i\left(\frac{\partial}{\partial t}|\tilde{\psi}(A,t)\rangle + \frac{\partial}{\partial A}|\tilde{\psi}(A,t)\rangle\frac{dA}{dt}\right) = \tilde{H}(A,t)|\tilde{\psi}(A,t)\rangle. \tag{6.3}$$

With the Floquet Hamiltonian defined as:

$$H_{\mathrm{F}}(A,t) = \tilde{H}(A,t) - i\frac{\partial}{\partial t}, \tag{6.4}$$

Eq. (6.3) becomes:

$$i\frac{\partial}{\partial A}|\tilde{\psi}(A,t)\rangle = K_{\mathrm{F}}(A,t)|\tilde{\psi}(A,t)\rangle, \tag{6.5}$$

where $K_{\mathrm{F}}(A,t) = H_{\mathrm{F}}(A,t)/(dA/dt)$. This equation is exactly in the same form of a Schrödinger equation with $t$ a dynamical variable, $A$ a time-like parameter, and $K_{\mathrm{F}}(A,t)$ a Hamiltonian-like operator. By solving Eq. (6.5), we obtain the wavefunction $|\tilde{\psi}(A,t)\rangle$

and the physical wavefunction $|\psi(t)\rangle$ is calculated by substituting the proper $A(t)$ into $|\tilde{\psi}(A,t)\rangle$, namely $|\psi(t)\rangle = |\tilde{\psi}(A(t),t)\rangle$. This treatment can be understood as elevating time $t$ to the role of a dynamical variable and considering evolution in an extended space with respect to a progress variable $A$. We note that the concept here was also used in developing numerical methods for the simulations of time-dependent Hamiltonians [79].

Because for any given value of the parameter $A$, $\tilde{H}(A,t)$ is periodic in $t$; according to Floquet theory, the eigenvalues of $K_{\rm F}(A,t)$ are functions of the quasienergies $\varepsilon_\alpha(A)$ and the eigenstates are the quasienergy states $|u_\alpha(A,t)\rangle$ of the Hamiltonian $\tilde{H}(A,t)$. The quasienergies and quasienergy states are given by an eigenvalue equation

$$K_{\rm F}(A,t)|u_\alpha(A,t)\rangle = \frac{\varepsilon_\alpha(A)}{dA/dt}|u_\alpha(A,t)\rangle. \tag{6.6}$$

We note that in the Hilbert space $\mathcal{R}$ where the original time-dependent Hamiltonian $H(t)$ is defined, the quasienergy states have a form

$$|u_\alpha(A,t)\rangle = \begin{pmatrix} s_{\alpha,0}(A,t) \\ s_{\alpha,1}(A,t) \\ \vdots \\ s_{\alpha,M-1}(A,t) \end{pmatrix}, \tag{6.7}$$

where $s_{\alpha,m}(A,t)$ are periodic functions of $t$ and $M$ is the dimension of the space $\mathcal{R}$. In this space, the inner product between states is defined as

$$\langle u_\alpha(A,t)|u_\beta(A,t)\rangle = \sum_m s^*_{\alpha,m}(A,t)s_{\beta,m}(A,t). \tag{6.8}$$

In the picture where we elevate time $t$ to the role of a dynamical variable, we consider the composite Hilbert space $\mathcal{R}\otimes\mathcal{T}$ made up of the Hilbert space $\mathcal{R}$ and the space $\mathcal{T}$ of functions which are periodic in $t$ with period $T = 2\pi/\omega$. As the periodic functions $s_{\alpha,m}(A,t)$ can be written as Fourier series where $s_{\alpha,m}(A,t) = \sum_n a_{\alpha,mn}(A)e^{in\omega t}$, the temporal part of the Hilbert space $\mathcal{T}$ is spanned by the orthonormal set of Fourier basis states $\langle t|e^{in\omega t}\rangle = e^{in\omega t}$ and the inner product in $\mathcal{T}$ reads

$$(e^{im\omega t}, e^{in\omega t}) = \frac{1}{T}\int_0^T dt\, \exp[i(n-m)\omega t] = \delta_{n,m}. \tag{6.9}$$

Thus, the inner product on the composite space $\mathcal{R}\otimes\mathcal{T}$ is given by

$$\begin{aligned}\langle\langle u_\alpha(A,t)|u_\beta(A,t)\rangle\rangle =&\frac{1}{T}\int_0^T dt\langle u_\alpha(A,t)|u_\beta(A,t)\rangle\\ =&\frac{1}{T}\int_0^T dt\sum_m s^*_{\alpha,m}(A,t)s_{\beta,m}(A,t)\\ =&\sum_m\sum_n a^*_{\alpha,mn}(A)a_{\beta,mn}(A).\end{aligned}\tag{6.10}$$

The dimension of this extended Hilbert space $\mathcal{R}\otimes\mathcal{T}$ is $M\times N$ where $N\to\infty$ is the total number of the Fourier basis. However, for the numerical calculation of the quasienergies and quasienergy states using Eq. (6.6), we usually truncate $N$ to a finite number.

With Eq. (6.5) and (6.6) together, it is not difficult to find that this problem can be analyzed by the standard adiabatic theory if we treat $A$ as a time-like parameter and $K_{\rm F}(A,t)$ a Hamiltonian-like operator defined on the space $\mathcal{R}\otimes\mathcal{T}$. The general solution of the Schrödinger equation is a superposition of the instantaneous quasienergy states:

$$|\tilde{\psi}(A,t)\rangle=\sum_\alpha c_\alpha(A)|u_\alpha(A,t)\rangle e^{-i\omega_\alpha(A)}e^{i\gamma_\alpha(A)},\tag{6.11}$$

where $\omega_\alpha(A)$ is the dynamic phase defined as

$$\omega_\alpha(A)=\int_{A_0}^A dA'\frac{\varepsilon_\alpha(A')}{v(A')}=\int_0^t\varepsilon_\alpha(t')dt',\tag{6.12}$$

with $v(A)=dA/dt$ and $\gamma_\alpha(A)$ is the geometric phase defined as

$$\gamma_\alpha(A)=i\int_{A_0}^A\langle\langle u_\alpha(A',t)|\frac{\partial}{\partial A'}|u_\alpha(A',t)\rangle\rangle dA'.\tag{6.13}$$

To determine the coefficients $c_\alpha(A)$, we substitute Eq. (6.11) into Eq. (6.5), which gives:

$$\begin{aligned}&i\sum_\alpha\frac{\partial}{\partial A}c_\alpha(A)|u_\alpha(A,t)\rangle e^{-i\omega_\alpha(A)}e^{i\gamma_\alpha(A)}+i\sum_\alpha c_\alpha(A)\left(\frac{\partial}{\partial A}|u_\alpha(A,t)\rangle\right)e^{-i\omega_\alpha(A)}e^{i\gamma_\alpha(A)}\\ &\quad-i\sum_\alpha c_\alpha(A)|u_\alpha(A,t)\rangle e^{-i\omega_\alpha(A)}e^{i\gamma_\alpha(A)}\langle\langle u_\alpha(A,t)|\frac{\partial}{\partial A}|u_\alpha(A,t)\rangle\rangle=0.\end{aligned}\tag{6.14}$$

By taking the scalar product of both sides of the above equation with $\langle u_\alpha(A,t)|$, we reach a set of differential equations with respect to the parameter $A$:

$$\frac{\partial}{\partial A}c_\alpha(A)=-\sum_{\alpha\neq\beta}c_\beta(A)\langle\langle u_\alpha(A,t)|\frac{\partial}{\partial A}|u_\beta(A,t)\rangle\rangle e^{i(\gamma_\beta(A)-\gamma_\alpha(A))}e^{-i(\omega_\beta(A)-\omega_\alpha(A))}.\tag{6.15}$$

Equivalently, we can also write Eq. (6.15) with respect to time $t$ as

$$\frac{\partial}{\partial t}c_\alpha(t) = -\sum_{\alpha\neq\beta} c_\beta(t)\frac{dA}{dt}\langle\langle u_\alpha(A,t)|\frac{\partial}{\partial A}|u_\beta(A,t)\rangle\rangle e^{i(\gamma_\beta(t)-\gamma_\alpha(t))}e^{-i(\omega_\beta(t)-\omega_\alpha(t))}. \tag{6.16}$$

Either of the two equations above can be used for solving coefficients $c_\alpha(A)$ or $c_\alpha(t)$.

We note that the instantaneous quasienergy state $|u_\alpha(A)\rangle$ is only well-defined up to an overall phase, *i.e.* states given by $e^{i\varphi(A)}|u_\alpha(A)\rangle$ are also properly normalized eigenstates with respect to operator $K_{\rm F}(A,t)$, where $\varphi(A)$ is an arbitrary function. We fix these phases, up to an overall phase for each state, by demanding

$$\langle\langle u_\alpha(A,t)|\frac{\partial}{\partial A}|u_\alpha(A,t)\rangle\rangle = 0. \tag{6.17}$$

This choice of the overall phase is convenient in the following calculations since it results that the geometric phase $\gamma_\alpha = 0$.

In the adiabatic limit where the parameter $A$ changes very slowly over time $t$, we have $dA/dt = 0$. According to Eq. (6.16), $c_\alpha(t)$ is a constant. Therefore, the state of the system reduces to

$$|\psi(t)\rangle = \sum_\alpha c_\alpha|u_\alpha(A,t)\rangle e^{-i\int_0^t \varepsilon_\alpha(t)dt}. \tag{6.18}$$

In the nonadiabatic limit, the solutions are given by the differential equations, Eq. (6.15). We note that all the equations are still exact so far. To proceed further analytically, we will employ the adiabatic perturbation theory (APT) [80].

In the first order perturbation theory [71, 80], we have to solve Eq. (6.15) iteratively keeping terms up to the first order in $v(A)$. This is equivalent to replacing $c_\beta(A) \to c_\beta(A_0)$ on the right-hand side of Eq. (6.15). We obtain:

$$c_\alpha(A) = c_\alpha(A_0) - \sum_{\beta\neq\alpha}\int_{A_0}^{A} c_\beta(A_0)\langle\langle u_\alpha(A',t)|\frac{\partial}{\partial A'}|u_\beta(A',t)\rangle\rangle e^{-i(\omega_\beta(A')-\omega_\alpha(A'))}dA'. \tag{6.19}$$

Approximate solutions for $c_\alpha(A)$ can be obtained by evaluating the integral on the right-hand side of Eq. (6.19).

## 6.2 Nonadiabatic transitions between Floquet states in a pulse-driven qubit

In this section, we will apply the APT to calculate nonadiabatic transitions between the Floquet states of a pulse-driven qubit where the amplitude of the pulses varies in time. We

start by calculating the instantaneous quasienergies and quasienergy states of the driven qubit for a certain pulse amplitude $A$. The rotating frame Hamiltonian of the qubit at its symmetry point is given by (see Section 3.1)

$$\tilde{H}_{\mathrm{RF}}(A,t) = -\frac{\Delta-\omega}{2}\sigma_z + A\cos(\omega t+\phi)(\cos(\omega t)\sigma_x + \sin(\omega t)\sigma_y), \tag{6.20}$$

where the frame rotates at the driving frequency $\omega$. Following the same procedure described in Section 3.3, the instantaneous quasienergies $\varepsilon_\alpha(A)$ and quasienergy states $|u_\alpha(A,t)\rangle$ are given by eigenvalues and eigenstates of the Floquet Hamiltonian, Eq. (3.23). Though there are $2N$ eigenvalues and eigenstates for the Floquet Hamiltonian if its dimension is $2N\times 2N$ ($N$ Fourier basis states are considered), only two eigenvalues and two eigenstates are the inequivalent quasienergies and quasienergy states of this problem. All the other solutions are copies correspond to shifting the inequivalent quasienergies by $n\omega$ and multiplying the inequivalent quasienergy states by $e^{in\omega t}$, with $n$ any integer. Hence, the index $\alpha$ that labels a solution to the eigenvalue equation, Eq. (6.6), should be understood as a two-fold index $\alpha=(\alpha',n)$ with $\alpha'=0$ or 1 indicating its corresponding inequivalent solution and $n=0,\pm1,\pm2\ldots$ denoting its energy shift with respect to that inequivalent solution. We have $\varepsilon_{\alpha',n}(A)=\varepsilon_{\alpha',0}(A)+n\omega$ and $|u_{\alpha',n}(A,t)\rangle = e^{in\omega t}|u_{\alpha',0}(A,t)\rangle$.

The state of the system decomposed into the instantaneous quasienergy states can be written as:

$$|\tilde{\psi}(A,t)\rangle = \sum_{\alpha',n} c_{\alpha',n}(A) e^{-i\int_{A_0}^{A}\varepsilon_{\alpha',n}(A')/v(A')dA'}|u_{\alpha',n}(A,t)\rangle. \tag{6.21}$$

If we choose the two inequivalent quasienergies and quasienergy states as $\varepsilon_{\alpha'}(A)=\varepsilon_{\alpha',0}(A)$ and $|u_{\alpha'}(A,t)\rangle = |u_{\alpha',0}(A,t)\rangle$ respectively, the above state can be written as a superposition of the two instantaneous states as follows:

$$|\tilde{\psi}(A,t)\rangle = \sum_{\alpha'} c_{\alpha'}(A) e^{-i\int_{A_0}^{A}\varepsilon_{\alpha'}(A')/v(A')dA'}|u_{\alpha'}(A,t)\rangle \tag{6.22}$$

with $c_{\alpha'}(A)=\sum_n c_{\alpha',n}(A)$. We can solve for the state $|\tilde{\psi}(A,t)\rangle$ by calculating the coefficients $c_{\alpha',n}$ using Eq. (6.19) in the following form:

$$c_{\alpha',n}(A) = c_{\alpha',n}(A_0) - \sum_{\substack{\beta'\neq\alpha'\\ m}}\int_{A_0}^{A} c_{\beta',m}(A_0)\langle\langle u_{\alpha',n}(A',t)|\frac{\partial}{\partial A'}|u_{\beta',m}(A',t)\rangle\rangle e^{-i(\omega_{\beta',m}(A')-\omega_{\alpha',n}(A'))}dA', \tag{6.23}$$

where $\omega_{\alpha',n}(A) = \int_{A_0}^{A} dA'\varepsilon_{\alpha',n}(A')/v(A')$. For the initial coefficients $c_{\beta',m}(A_0)$, we let $c_{\beta',m}(A_0)=c_{\beta'}(A_0)\delta_{m,0}$ without losing generality because it is the sum of coefficients of all

the redundant copies of the Floquet states $c'_\beta = \sum_m c_{\beta',m}$ rather than the actual values of these coefficients that define the states in the eigenbasis of the qubit. We obtained

$$c_{\alpha'}(A) = c_{\alpha'}(A_0) - \sum_{\substack{\beta' \neq \alpha' \\ n}} \int_{A_0}^{A} c_{\beta'}(A_0) \langle\langle u_{\alpha',n}(A',t)| \frac{\partial}{\partial A'} |u_{\beta',0}(A',t)\rangle\rangle e^{-i(\omega_{\beta',0}(A') - \omega_{\alpha',n}(A'))} dA' \tag{6.24}$$

by summing Eq. (6.23) over $n$. The equations above can be generally applied to calculating evolution of a multi-level driven system. In particular for a two-level system where $\alpha' = 0, 1$, we have

$$c_0(A) = c_0(A_0) - c_1(A_0) \sum_n \int_{A_0}^{A} \langle\langle u_{0,n}(A',t)| \frac{\partial}{\partial A'} |u_{1,0}(A',t)\rangle\rangle e^{-i(\omega_{1,0}(A') - \omega_{0,n}(A'))} dA'. \tag{6.25}$$

If we quantify the nonadiabatic transition as the difference in the coefficients $\delta c_0(A_0, A) = c_0(A) - c_0(A_0)$, we know from the equation above that this quantity is proportional to

$$N_{c_0}(A_0, A) = \sum_n \int_{A_0}^{A} \langle\langle u_{0,n}(A',t)| \frac{\partial}{\partial A'} |u_{1,0}(A',t)\rangle\rangle e^{-i(\omega_{1,0}(A') - \omega_{0,n}(A'))} dA'. \tag{6.26}$$

We note that $N_{c_0}(A_0, A)$ depends on the shape of the pulse envelope because the terms $\omega_{\alpha,n}(A)$ in the exponent depend on the varying rate of the pulse amplitude $v(A) = dA/dt$.

Next, we will calculate the nonadiabatic transitions within the amplitude modulated pulses used in experiments discussed in Chapter 5. The amplitude of the pulses is defined as

$$A(t) = \begin{cases} \frac{A_\mathrm{m}}{2}(1 - \cos(\pi t/t_\mathrm{r})) & t \leq t_\mathrm{r} \\ A_\mathrm{m} & t_\mathrm{r} < t \leq t_\mathrm{r} + t_\mathrm{p} \\ \frac{A_\mathrm{m}}{2}(1 + \cos(\pi(t - t_\mathrm{p} - t_\mathrm{r})/t_\mathrm{f})) & t_\mathrm{r} + t_\mathrm{p} < t \leq t_\mathrm{r} + t_\mathrm{p} + t_\mathrm{f} \end{cases}, \tag{6.27}$$

where $A_\mathrm{m}$ is the maximum amplitude of the pulse, $t_\mathrm{p}$ is the maximum amplitude duration of the pulse, and $t_{\mathrm{r,f}}$ the rise/fall time of the pulse. We choose to analyze pulses with the rising/falling edge being a cosine function because it is a modulation scheme that requires a small bandwidth which is commonly used in experiments. Since the nonadiabatic transitions occur both in the rising and falling edge of the pulse, we will deal with these two cases separately in the remaining part of this section. We will consider the case of resonance driving ($\omega = \Delta$) and $\phi = 0$ here but our treatment can be generalized to arbitrary values of $\omega$ and $\phi$.

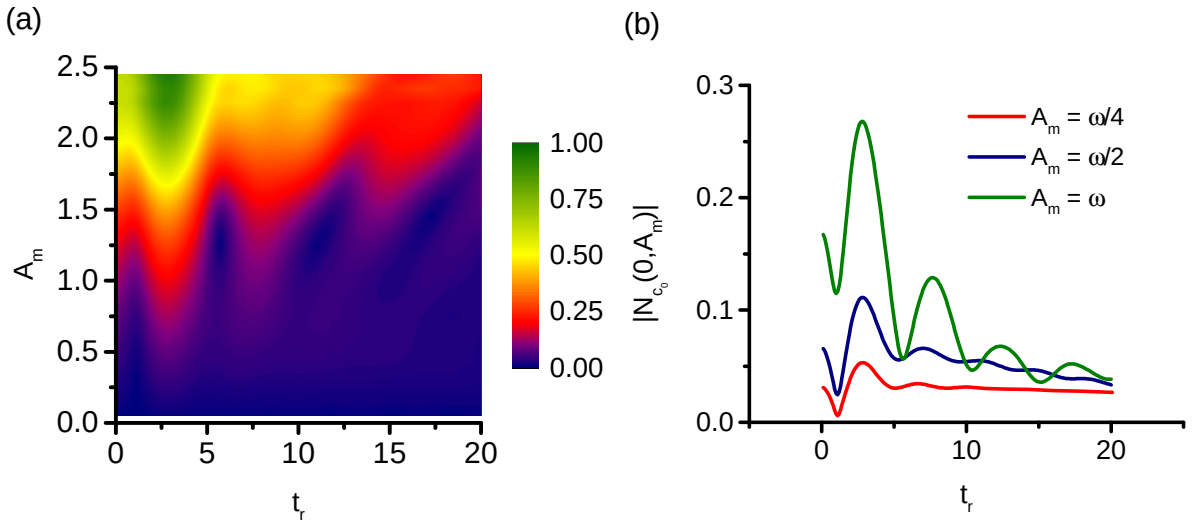



Figure 6.1: **Nonadiabatic transitions between Floquet states during the rising edge.** (a) A color plot of the nonadiabatic transition amplitude $|N_{c_0}(0, A_{\rm m})|$ versus the maximum amplitude $A_{\rm m}$ and the rise time $t_{\rm r}$. (b) A plot of $|N_{c_0}(0, A_{\rm m})|$ versus $t_{\rm r}$ at $A_{\rm m} = \omega/4$ (red line), $A_{\rm m} = \omega/2$ (blue line), and $A_{\rm m} = \omega$ (green line). In the calculation, we assume resonance driving ($\omega = \Delta$) and $\phi = 0$.

## Rising edge

Using the pulse shape defined in Eq. (6.27), we derive the varying rate of the pulse amplitude during the rising edge as

$$v(A) = \frac{\pi A_{\rm m}}{2t_{\rm r}} \sin\left(\arccos\left(1 - \frac{2A}{A_{\rm m}}\right)\right). \tag{6.28}$$

We first numerically calculate all the instantaneous quasienergies and quasienergy states for values of $A$ from $A_0 = 0$ to $A_{\rm m}$ in small steps using parameters $\omega = \Delta$ and $\phi = 0$. We then evaluate the sum and integral in Eq. (6.26) to calculate the nonadiabatic transition amplitude $|N_{c_0}(0, A_{\rm m})|$ after the rising edge of the pulse versus the maximum amplitude $A_{\rm m}$ and the rise time $t_{\rm r}$ (see Figure 6.1(a)). In Figure 6.1(b), we show $|N_{c_0}(0, A_{\rm m})|$ versus $t_{\rm r}$ for a few strong driving pulse amplitude. As expected, for long rise time $t_{\rm r} \gg 1/\omega$ where the evolution should be adiabatic, we have $|N_{c_0}(0, A_{\rm m})| \to 0$. For short rise time $t_{\rm r} \sim 1/\omega$, the nonadiabatic transition amplitude oscillates versus $t_{\rm r}$ due to interference of the transitions between the Floquet states induced by the fast changing pulse amplitude. We notice that for the particular pulse shape analyzed here, $|N_{c_0}(0, A_{\rm m})|$ has a local minimum around $t_{\rm r} = 1/\omega$ regardless the value of $A_{\rm m}$, given $A_{\rm m} \lesssim \omega$. At these points, the nonadiabatic transitions are small as if we were turning the pulse on adiabatically. This suppression of nonadiabatic transitions can be understood as coherent interference of the transitions between the Floquet states.

So far, the above calculations on the nonadiabatic transition amplitude between Floquet states are based on the first order APT (Eq. (6.19)). Since it is only an approximate solution to the problem, we should expect it to break down in the regime where the pulse amplitude is changing very fast. Next, we will compare the solutions given by first order APT to exact numerical simulations. Because the quantity related to the nonadiabatic transition defined as $\delta c_0(0, A_{\rm m}) = c_0(A_{\rm m}) - c_0(0)$ is an initial-state dependent quantity, we will calculate $\delta c_0(0, A_{\rm m})$ for a representative initial state in which $c_0(0) = 1/\sqrt{2}$ and $c_1(0) = -1/\sqrt{2}$ to make the comparison. In the energy eigenstate basis of the qubit, the above chosen state corresponds to the ground state $|0\rangle$. For the exact calculation of $\delta c_0(0, A_{\rm m})$ after the rising edge of the pulse, we use a numerical solver [34] to solve the qubit state $|\psi(t)\rangle$ under the time-dependent Hamiltonian given by Eq. (6.20) with the rising amplitude $A(t)$ defined as Eq. (6.27). We then use Eq. (6.22) to decompose $|\psi(t)\rangle$ into quasienergy states and obtain $c_{0,1}(A_{\rm m})$. In Figure 6.2, we compare $\delta c_0(0, A_{\rm m})$ calculated using the first order APT (Eq. (6.26)) and the exact solutions from the numerics. We find that in the regime where the maximum driving amplitude is not too large ($A_{\rm m} \lesssim \omega$), the solutions of $c_{0,1}(A_{\rm m})$ given by the first order APT are very accurate. The approximation breaks down in the regime where the driving amplitude $A_{\rm m}$ is large compared with the frequency of the qubit.

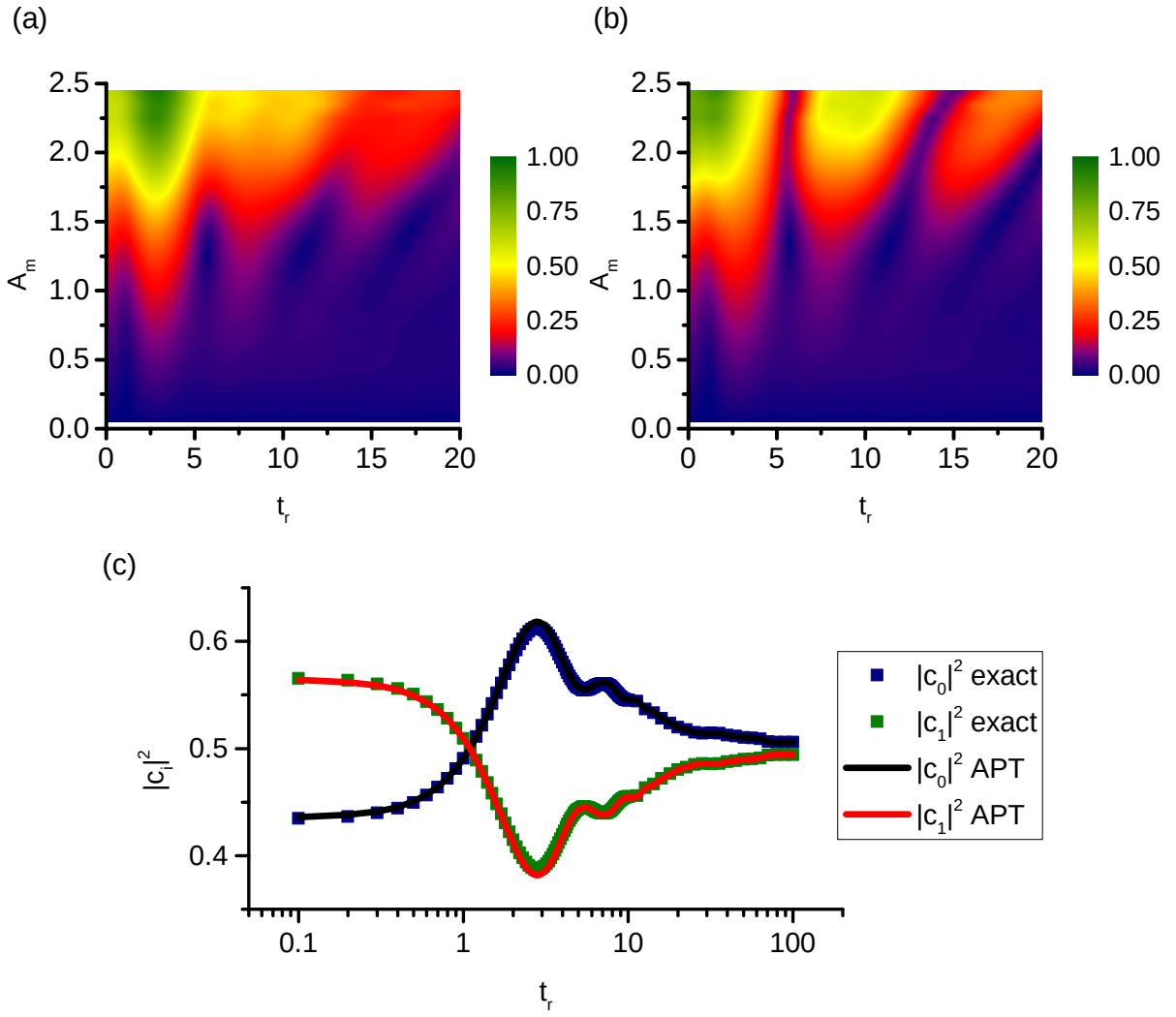



Figure 6.2: **Verification of the adiabatic perturbation theory during the rising edge.** (a), (b) Color plots of the amplitude of the change in the coefficient $|\delta c_0(0, A_\mathrm{m})|$ versus the maximum amplitude $A_\mathrm{m}$ and the rise time $t_\mathrm{r}$ calculated with the first order APT (a) and exact numerical simulations (b). (c) A plot of the probabilities of the Floquet states after the pulse $|c_{0,1}(0, A_\mathrm{m})|^2$ versus $t_\mathrm{r}$ at $A_\mathrm{m} = \omega/2$ to compare the calculations based on the first order APT with the exact solutions.

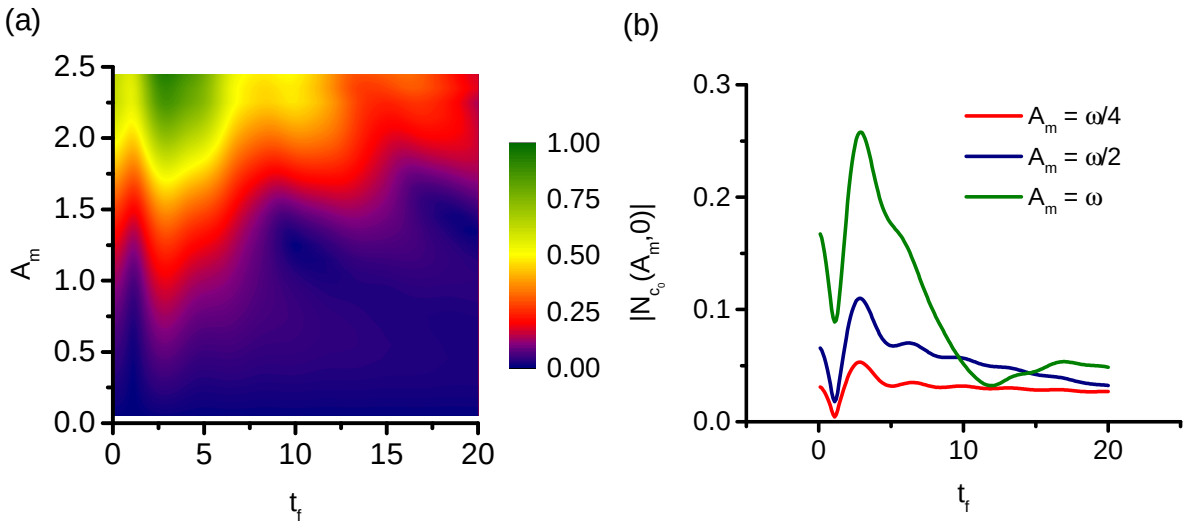



Figure 6.3: **Nonadiabatic transitions between Floquet states during the falling edge.** (a) A color plot of the nonadiabatic transition amplitude $|N_{c_0}(A_{\rm m}, 0)|$ versus the maximum amplitude $A_{\rm m}$ and the fall time $t_{\rm f}$. (b) A plot of $|N_{c_0}(A_{\rm m}, 0)|$ versus $t_{\rm f}$ at $A_{\rm m} = \omega/4$ (red line), $A_{\rm m} = \omega/2$ (blue line), and $A_{\rm m} = \omega$ (green line). In the calculation, we assume resonance driving ($\omega = \Delta$) and $\phi = 0$.

## Falling edge

The nonadiabatic transitions in the falling edge of the pulse can be calculated in a similar way as that of the rising edge. We have

$$v(A) = -\frac{\pi A_{\rm m}}{2t_{\rm f}} \sin\left(\arccos\left(\frac{2A}{A_{\rm m}} - 1\right)\right). \tag{6.29}$$

The relevant quantity to the nonadiabatic transition $N_{c_0}(A_{\rm m}, 0)$ can be found by evaluating the integral in Eq. (6.26) from $A_0 = A_{\rm m}$ to $A = 0$. In Figure 6.3, we show that the nonadiabatic transition amplitude after the falling edge of the pulse, $|N_{c_0}(A_{\rm m}, 0)|$, versus the maximum pulse amplitude $A_{\rm m}$ and the fall time $t_{\rm f}$. In the adiabatic limit $t_{\rm f} \gg 1/\omega$, we have $N_{c_0}(A_{\rm m}, 0) \to 0$ as expected. We also notice coherent suppression of nonadiabatic transitions at $t_{\rm f} = 1/\omega$ where $A_{\rm m} \lesssim \omega$.

Again, we calculate the change of the Floquet state coefficients after the falling edge $\delta c_0(A_{\rm m}, 0) = c_0(0) - c_0(A_{\rm m})$ for an initial state of which $c_0(A_{\rm m}) = 1/\sqrt{2}$ and $c_1(A_{\rm m}) = -1/\sqrt{2}$. The exact numerical calculation is performed in three steps: 1. Calculate the

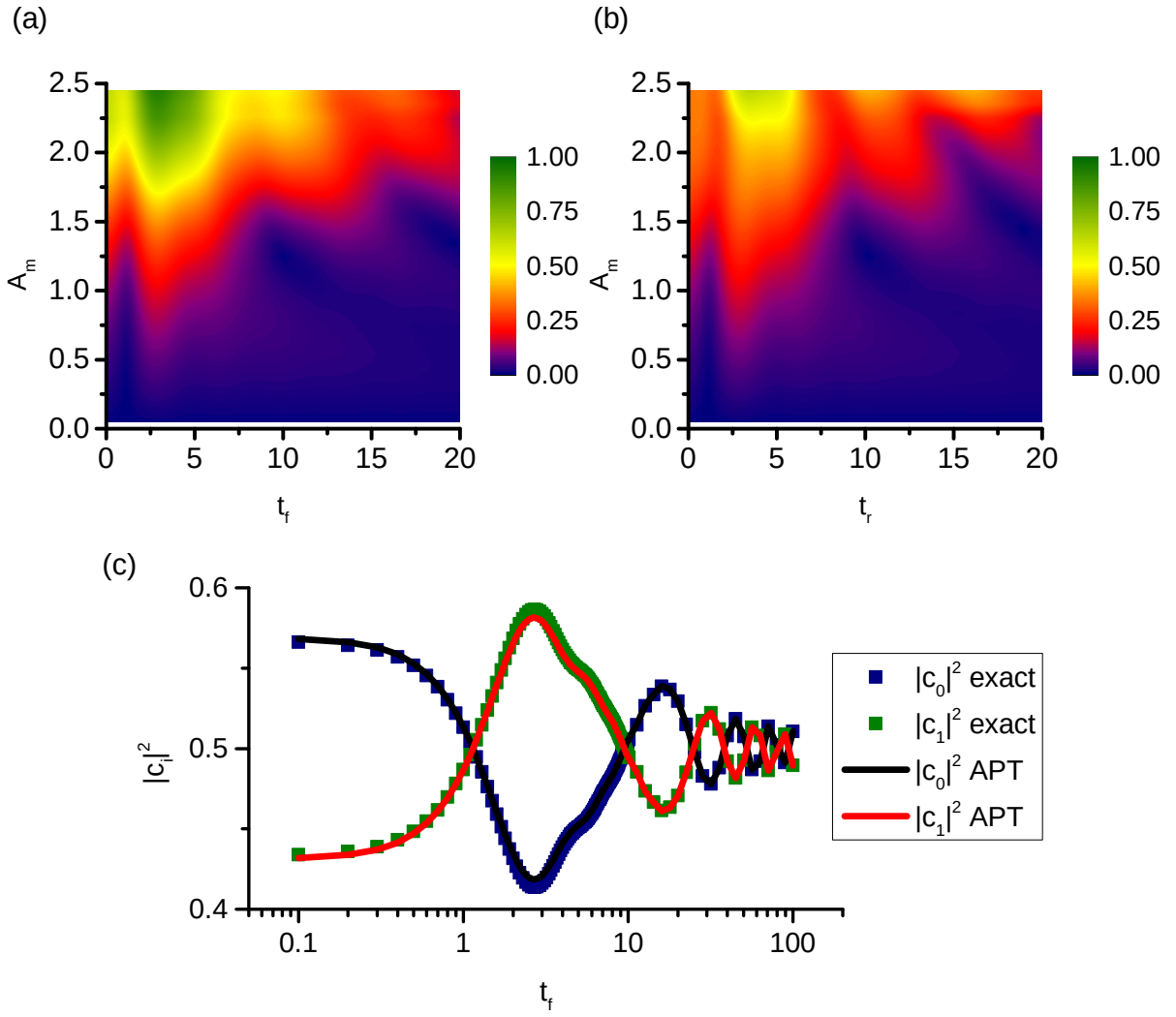



Figure 6.4: **Verification of adiabatic perturbation theory during the falling edge.** (a), (b) Color plots of the amplitude of the change in the coefficient $|\delta c_0(A_\mathrm{m}, 0)|$ versus the maximum amplitude $A_\mathrm{m}$ and the fall time $t_\mathrm{f}$ calculated with the first order APT (a) and exact numerical simulations (b). (c) A plot of the probabilities of the Floquet states after the pulse $|c_{0,1}(A_\mathrm{m}, 0)|^2$ versus $t_\mathrm{f}$ at $A_\mathrm{m} = \omega/2$ to compare the calculations based on APT with exact the solutions.

quasienergy states at the amplitude $A_{\rm m}$ and use Eq. (6.22) to obtain the initial state $|\tilde{\psi}(A_{\rm m},0)\rangle$ in the energy eigenbasis of the qubit. 2. Perform time-dependent Hamiltonian simulations with the given initial state. 3. Decompose the final state into quasienergy states at amplitude $A = 0$, which yields $c_0(0)$ and $c_1(0)$ at the end of the pulse. In Figure 6.4, we show that the solutions from the first order APT is a good approximation to the exact solutions in the regime where $A_{\rm m} \lesssim \omega$.

## 6.3 Optimized pulses for single-qubit operations

As we have discussed in Chapter 5, the absence of nonadiabatic transitions between Floquet states results in smooth and simple Rabi oscillations between energy eigenstates of the qubit. This is a desirable property for implementing arbitrary high-fidelity single-qubit operations in the strong driving regime. Nonadiabatic transitions can be suppressed either by turning the pulse on and off adiabatically or by using the destructive interference of the nonadiabatic transitions as we discussed in Section 6.2. In reality, qubits suffer from decoherence over time thus the fidelity of operations decreases as the operation time increases. For the adiabatic pulse in the strong driving regime, we require $t_{\rm r/f} \gg 1/\omega$, which means the total pulse duration $t_{\rm total} \gg 1/\omega$. In the weak driving regime, we also have the same requirement $t_{\rm total} \gg 1/\omega$ because the pulse duration $t_{\rm total}A_{\rm m} \sim 1$ and $A_{\rm m} \ll \omega$. Therefore, adiabatic pulses in the strong driving regime do not necessarily yield higher operation speed than the weak driving pulses do. However, with coherent suppressions of the nonadiabatic transition which requires careful control of the rise and fall times and the shape of the pulses, we could realize qubit operations in the time scale of $t_{\rm total} \sim 1/\omega$. In this section, we will present simulations of the process fidelity of single-qubit operations with decoherence being taken into account.

### 6.3.1 Quantum process characterization

Characterization of a quantum process can be done by means of quantum process tomography (QPT) [81, 82]. The goal of QPT is to determine the completely positive map $\mathcal{E}$, which represents the process acting on an arbitrary input state $\rho$. There are many representations for a quantum process. Here we adopt the $\chi$-matrix representation. In this representation, any process for a $d$ dimensional system can be written as

$$\mathcal{E}(\rho) = \sum_{m,n=0}^{d^2-1} \chi_{mn} B_m \rho B_n^\dagger \tag{6.30}$$

where $\{B_n\}$ are operators which form a basis in the space of $d \times d$ matrices, and $\chi$ is the process matrix to be characterized. The process matrix $\chi$ acts as a superoperator in the basis operators $\{B_n\}$ for characterization of the process $\mathcal{E}$. By definition the $\chi$ matrix must be Hermitian and the completeness constraint requires that it must satisfy

$$\sum_{mn} \chi_{mn} B_n^\dagger B_m = \mathbb{1}. \tag{6.31}$$

For one qubit ($d = 2$), the process matrix can be defined by the Pauli operator basis $\{B_n\} = \{\mathbb{1}, \sigma_x, \sigma_y, \sigma_z\}$. The $\chi$-matrix can be uniquely defined if all the output states $\rho_{\text{out}} = \mathcal{E}(\rho_{\text{in}})$ for the four linearly independent input state $\rho_{\text{in}}$ is determined.

From the process matrix $\chi$ obtained by QPT and its ideal counterpart $\chi_{\text{ideal}}$, we can directly calculate the process fidelity, defined as $F_{\text{p}} = \text{tr}[\chi_{\text{ideal}}\chi]$. We can also calculate the gate fidelity defined as

$$F_{\text{g}} = \int d\psi \langle\psi|U^\dagger \mathcal{E}(\psi) U|\psi\rangle, \tag{6.32}$$

where $U$ is the ideal implementation of a certain quantum gate. We can understand $F_{\text{g}}$ as the state fidelity of the process output state $\mathcal{E}(\psi)$ with respect to the ideal output state $U|\psi\rangle$ averaged over all possible input states $|\psi\rangle$. According to Ref. [83], there is a simple relation between the process fidelity $F_{\text{p}}$ and gate fidelity $F_{\text{g}}$, namely

$$F_{\text{g}} = (dF_{\text{p}} + 1)/(1 + d). \tag{6.33}$$

### 6.3.2 Simulations of strong driving gates

Universal single-qubit operations require unitaries corresponding to rotations around two axes in the Bloch sphere with arbitrary angles. We will consider implementing operations around the $x$- and $y$-axis (*i.e.* $R_x(\theta)$ and $R_y(\theta)$) since they can be realized with only AC modulation to the qubit parameter. The Hamiltonian under consideration is the rotating frame Hamiltonian of a qubit driven by resonant pulses, given by Eq. (6.20) with $\omega = \Delta$. The shape of the pulse amplitude $A(t)$ is defined in Eq. (6.27). The qubit operations are fully determined by the following pulse parameters: $A_{\text{m}}$, $\phi$, $t_{\text{r}}$, $t_{\text{f}}$, and $t_{\text{p}}$. With decoherence taken into account, we can express it as a quantum process matrix $\chi(A_{\text{m}}, \phi, t_{\text{r}}, t_{\text{f}}, t_{\text{p}})$.

In our simulations of the process matrix, we choose $|0\rangle$, $|1\rangle$, $(|0\rangle + i|1\rangle)/\sqrt{2}$, and $(|0\rangle - |1\rangle)/\sqrt{2}$ as input states and obtain their output states by numerically solving the master equation. We then solve the systems of linear equations defined by Eq. (6.30) for

the elements $\chi_{mn}$ of the process matrix. The output states are obtained from numerical simulations of the master equation in the Lindblad form [40]

$$\dot{\rho}(t) = -i[H(t), \rho(t)] + \sum_n \frac{\kappa_n}{2}(2\hat{L}_n\rho\hat{L}_n^\dagger - \hat{L}_n^\dagger\hat{L}_n\rho - \rho\hat{L}_n^\dagger\hat{L}_n), \tag{6.34}$$

where $\hat{L}_n$ and $\kappa_n$ are the Lindblad operator and the decoherence rate for a certain decoherence source respectively. Here we consider only one decoherence mechanism, energy relaxation, which is commonly regarded as the major limiting factor to the gate fidelity. In this case, the sum in Eq. (6.34) only has one term, where we use $\hat{L} = \sigma_-$ and $\kappa = 1/T_1$. The actual values of the qubit parameters are chosen to be the same as those characterized in the experiments discussed in Chapter 5, where $\Delta = 2\pi \times 2.288$ GHz and $T_1 = 2$ $\mu$s.

We choose the parameters of the pulse in a way that nonadiabatic transitions between Floquet states are suppressed. Whereas the adiabatic evolution given by

$$|\psi(t)\rangle = \sum_\alpha c_\alpha |u_\alpha(A,t)\rangle e^{-i\int_0^t \varepsilon_\alpha(t)dt} \tag{6.35}$$

is a simple rotation around the axis that lies along $|u_\alpha(0,t)\rangle$ in the Bloch sphere. For implementing $R_x(\theta)$, we use a pulse phase $\phi = 0$ which gives quasienergy states, $|u_{0,1}(0,t)\rangle = (|0\rangle \pm |1\rangle)/\sqrt{2}$, lying along the $x$-axis. The rise and fall times of the pulse are chosen to be $t_\mathrm{r} = 1.0/\omega \approx 80$ ps and $t_\mathrm{f} = 1.0/\omega \approx 80$ ps where coherent suppression of the nonadiabatic transition occurs on both the rising and fall edge. The rotation angle $\theta$ of the operation is controlled by the maximum amplitude duration of the pulse $t_\mathrm{p}$ with $\theta = \frac{1}{2}(\varepsilon_1 - \varepsilon_0)\left(t_\mathrm{p} + \frac{t_\mathrm{r}+t_\mathrm{f}}{2}\right)$.

For implementing $R_y(\theta)$, we use the pulses with phase $\phi = \pi/2$ which give quasienergy states, $|u_{0,1}(0,t)\rangle = (|0\rangle \pm i|1\rangle)/\sqrt{2}$, lying along the $y$-axis. The optimal rise and fall times for destructive interference of the nonadiabatic transitions are given by $t_\mathrm{r} = 3.0/\omega \approx 200$ ps and $t_\mathrm{f} = 3.0/\omega \approx 200$ ps, which is calculated by a procedure similar to what is discussed in the previous section.

In Figure 6.5, we plot the calculated gate fidelity of the qubit operations $R_x(\theta)$ and $R_y(\theta)$ implemented by resonant strong pulses where the maximum amplitude $A_\mathrm{m} = \Delta/4 = 2\pi \times 0.572$ GHz. The overall gate fidelity is higher for the pulses whose rising and falling edge is optimized for suppressions of the nonadiabatic transition between the Floquet states. We note that arbitrary rotations around the $x$- and $y$-axis can be completed within a total pulse time of 2 ns and an average gate fidelity higher than 99.8%. In particular for operations $R_x(\pi/2)$ and $R_y(\pi/2)$ in the single-qubit Clifford group [84], a gate fidelity of 99.94% (for the both operations) can be achieved with pulse times of 520 ps and 640 ps

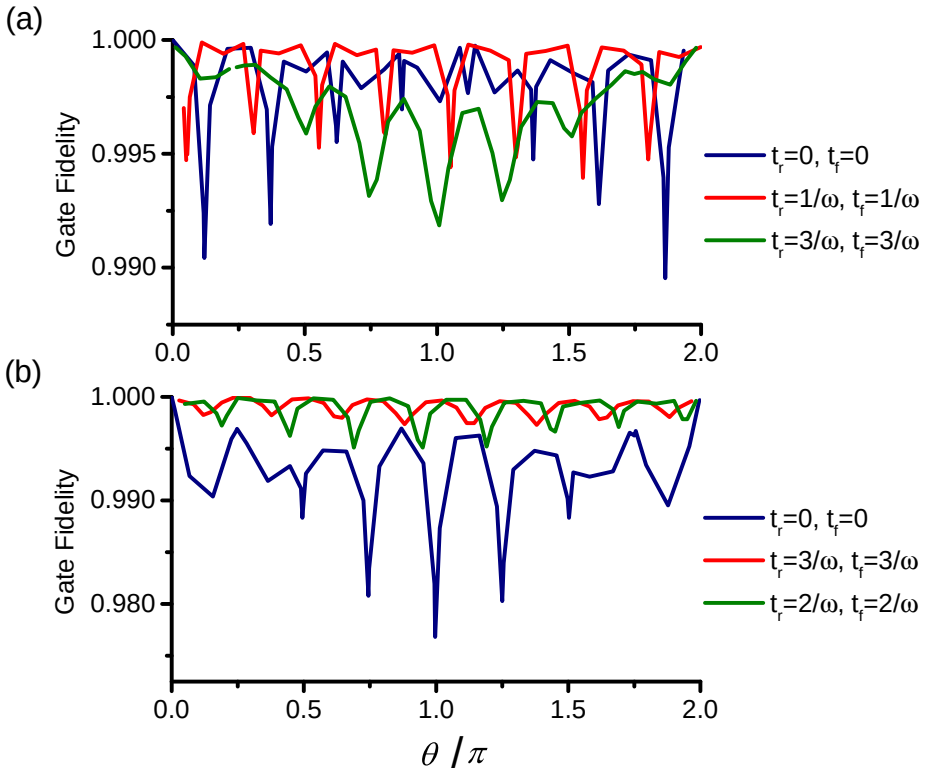



Figure 6.5: **Gate fidelity of optimized pulses for $R_x(\theta)$ and $R_y(\theta)$.** We plot simulated gate fidelity of $R_x(\theta)$ (a) and $R_y(\theta)$ (b) operations versus the rotation angle $\theta$ with different combinations of $t_{\rm r}$ and $t_{\rm f}$. The pulses in the simulation have the frequency $\omega = \Delta$ and the maximum amplitude $A_{\rm m} = \omega/4$. The operations corresponding to pulses with rise and fall times optimized for suppressed nonadiabatic transitions (red lines) have overall higher gate fidelities.

respectively, where a pulse resolution of 40 ps is assumed. We note that thanks to the cosine-function shape of the pulse during the rising and falling edge, this pulse scheme only requires a bandwidth of $2\omega$. For superconducting qubits which usually have a transition frequency of a few GHz, such pulses can be generated by a high-bandwidth AWG directly (see Chapter 5).

## 6.4 Conclusion

In conclusion, we have presented a pulse scheme for high-fidelity arbitrary single-qubit operations with strong driving. We analyze the effects of the rising and falling edge of the pulse with adiabatic perturbation theory in the Floquet picture. By tuning the rise and fall time of the pulse, we coherently suppress the nonadiabatic transition between Floquet states. The absence of nonadiabatic transitions leads to simple rotations of the Bloch vector although the rotating wave approximation is no longer valid. By taking advantage of the fast dynamics with strong driving, high-fidelity single-qubit gates can be realized with ultra-short pulses. Furthermore, our pulse scheme is compliant with the technical specifications of the latest available arbitrary waveform generator, and thus is ready to be implemented in experiments.

# Part II

# Decoherence in superconducting resonators and superconducting qubits

# Chapter 7

# Decoherence in superconducting resonators

Superconducting resonators have a broad range of applications in fields of quantum information processing, microwave engineering, and sensitive detection. In these applications, decoherence of the resonator, normally due to the photon loss, is a major limiting factor on the performance of the devices.

In a circuit QED system, resonators strongly coupled to superconducting qubits are used for qubit state measurement and as quantum buses for qubit-qubit coupling. In this system, spontaneous qubit decay into the resonators, known as the Purcell effect [85], can be a considerable source for the qubit relaxation. The Purcell limited qubit relaxation rate is proportional to the average photon loss rate of the resonator. Therefore, in the effort of making long-lived qubits, it is of great importance to understand and reduce the loss in superconducting resonators.

In addition, the photon loss is often found to be dominated by dielectric loss in superconducting resonators. The internal loss of resonators is a direct measurement of the dielectric loss, where the lossy material forms the dielectric layer of the capacitors in superconducting LC resonators. In this case, superconducting resonators can be used as measurement tools for the studies of dielectric materials. These studies are very relevant

[1]The materials in the first sections of this chapter has been published in J. Appl. Phys. 114, 054504 (2013).

[2]The materials in the second section of this chapter has been published in Appl. Phys. Lett. 104, 043506 (2014).

to superconducting qubits where dielectric loss is an important source of decoherence as well.

In the first section of this chapter, we will describe an analysis method for reliable determination of the resonators' photon loss based on microwave transmission measurements. This method is robust against imperfections in the transmission line which connects the VNA to the resonators being measured, thus it is suitable for analyzing superconducting resonators in cryostats, where the defects in the transmission lines are hard to be characterized at low temperature. In the second section, we will discuss measurements of microwave loss of aluminum oxide which is an important material widely used in superconducting devices. The analysis method discussed in the first section will be used in this characterization.

## 7.1 An analysis method for transmission measurements of superconducting resonators

Measuring the response of a resonator is a generic method for measurements of properties of solids at low temperature, such as surface resistance [86] of superconductors and complex permittivity [87] of dielectrics. It is also very useful for sensitive detection of photons [88], states of superconducting quantum bits [89], and the zero-point motion of mechanical oscillators [90]. Recently, the need for increasing coherence times of superconducting qubits motivated new interest in searching for low-loss dielectric materials as well as understanding their loss mechanism. Internal quality factors of several types of superconducting thin-film resonators [91, 92, 93, 94, 95, 96, 97, 98, 99, 100] have been measured in detail. The most common way to measure the internal quality factor is to measure the S-parameters of resonant circuits. For this purpose, a number of methods were developed to extract the quality factor of a single resonator from reflection or transmission measurements [101]. In order to measure multiple resonators simultaneously, methods [102, 103, 93] based on frequency multiplexing have been developed. However, all the previous methods derive the scattering parameters (S-parameters) [24] by using equivalent coupled circuits in the vicinity of the resonance. In this paper, we present a consistent method to approximate the exact S-parameters by analyzing the algebraic properties of the S-parameter function. We start from a circuit model in which a LC resonator couples to a transmission line both inductively and capacitively. We develop the Closest Pole and Zero Method (CPZM) to reduce the transmission S-parameter $S_{21}(\omega)$, with $\omega$ the excitation frequency, of the circuit to a ratio of complex linear functions. The approximated $S_{21}(\omega)$ only depends on four parameters: resonance frequency $\omega_0$, internal quality factor $Q_i$, external quality factor $Q_e$

and a parameter $Q_\alpha$ which is related to the resonance asymmetry. The internal quality factor $Q_i$ can be extracted from fitting the data to the simplified $S_{21}(\omega)$ function as opposed to the full circuit-dependent form.

We also discuss another important aspect of dielectric loss characterization. In order to understand sources and mechanisms of the loss, the dependence of dielectric loss on energy stored in the resonator is required. The energy dependence of loss can be characterized [91, 95, 104] by measuring $Q_i$ as a function of the voltage $V$ across the capacitor in the LC resonator. However, this is a nontrivial task since one usually does not have precise knowledge of all the circuit parameters needed to calculate $V$. We show that the ratio $V/V_{\text{in}}^+$, where $V_{\text{in}}^+$ is the forward propagating wave amplitude at the excitation port, can be calculated using parameters determined from the fit of the $S_{21}(\omega)$ function and an additional scaling factor. The scaling factor depends on circuit parameters which cannot be directly determined from the fit. However, it can be estimated based on circuit parameter simulations. An important point to note is that the knowledge of the voltage $V$ up to a fixed factor is still valuable for comparing experimental results with theoretical predictions of the loss mechanism.

Although the reduced $S_{21}$ fits the experimental data extremely well, in some measurements the resonance curve shows a pronounced asymmetry, which is inconsistent with realistic values of circuit parameters. We analyze a more complete model which takes the reflection of wire bonds and impedance mismatch into account. We find that for realistic circuits the asymmetric resonance primarily arises from wave reflection by the wire bonds used to connect the device and the measurement apparatus. We show that despite these non-idealities, our procedure for extracting $Q_i$ based on the simplified $S_{21}$ form is still valid.

We note that, in previous work, simplified equivalent circuits were used to obtain a simple expression for the S-parameters in the linear fractional form [105]. However, we develop a systematic approach to reduce the response function of an arbitrary resonator to a linear fractional form by using specifically its algebraic properties.

This section is organized as follows. In Subsection 7.1.1, we approximate the transmission S-parameter $S_{21}$ of the resonance circuit we consider to a linear fractional form by applying the CPZM. In Subsection 7.1.2, we investigate the complex function $v(\omega) = V/V_{\text{in}}^+$, where $V$ is the capacitor voltage and $V_{\text{in}}^+$ is the forward propagating wave voltage. We approximate $v(\omega)$ to a linear fractional form using the same method and we find that $v$ depends on $Q_i$ in general. We derive a formula to transform the points $(V_{\text{in}}^+, Q_i)$ to $(V, Q_i)$. In Subsection 7.1.3, we employ the CPZM to analyze the transmission parameter $S_{21}$ of a circuit where we consider the inductance of the bonding wires and the effect of variation of impedance of different transmission lines. In Subsection 7.1.4, we discuss the

general application of CPZM to the circuit response of both lumped and distributed high-Q resonators.

### 7.1.1 Derivation of resonator transmission

#### Experimental design and circuit model

We consider a LC resonator coupled to a transmission line. In our experiments, the resonator consists of a meander inductor $L$ and a parallel capacitor $C_0$. The transmission line is a coplanar waveguide (CPW) (see Fig. 7.1(a) for the sample design). We use a model circuit similar to that proposed in Ref. [103], as shown in Fig. 7.1(b). The LC resonator couples to the transmission line through a mutual inductance $M$ and a capacitor $C_c$. Dielectric loss is modeled by a resistor $R$ shunting the lumped capacitor $C_0$. Both the input and output transmission lines have characteristic impedance $Z_0$.

#### Exact $S_{21}$ from circuit model

Fig. 7.2 shows the equivalent circuit of the network shown in Fig. 7.1(b). Since the impedance of the source and load match the characteristic impedance of the transmission line, we have $V_g = 2V_{\text{in}}^+$ and $V_{\text{out}}^+ = V_{\text{out}}$ where $V_g$ is the voltage of the source and $V_{\text{out}}$ is the voltage on the output load. We use Kirchhoff's laws to calculate $S_{21} = V_{\text{out}}^+/V_{\text{in}}^+ = 2V_{\text{out}}/V_g$, which gives:

$$S_{21} = \frac{1}{1 + \frac{Z'_{\text{in}}}{Z_0} + j\omega C_c Z'_{\text{in}}} \left(2 + \frac{V}{V_{\text{in}}^+}\left(j\omega C_c Z'_{\text{in}} + \frac{M}{L}\right)\right) \tag{7.1}$$

where

$$\frac{V}{V_{\text{in}}^+} = -2\,\frac{\frac{M}{L} - j\omega C_c Z'_{\text{out}}}{Z'_{\text{out}} + Z'_{\text{in}}} \Bigg/ \left(\frac{1}{j\omega L} + \frac{1}{Z_C} + \frac{j\omega C_c}{j\omega C_c Z_0 + 1} + \frac{(\frac{M}{L} - j\omega C_c Z'_{\text{out}})^2}{Z'_{\text{out}} + Z'_{\text{in}}}\right) \tag{7.2}$$

and

$$Z'_{\text{in}} = Z_0 + j\omega L_1 - j\omega M^2/L, \tag{7.3}$$

$$Z'_{\text{out}} = \frac{Z_0}{1 + j\omega C_c Z_0}, \tag{7.4}$$

$$\text{and} \quad Z_C = \frac{1}{j\omega C_0 + 1/R}. \tag{7.5}$$

Here, the imaginary unit is denoted by $j = \sqrt{-1}$.

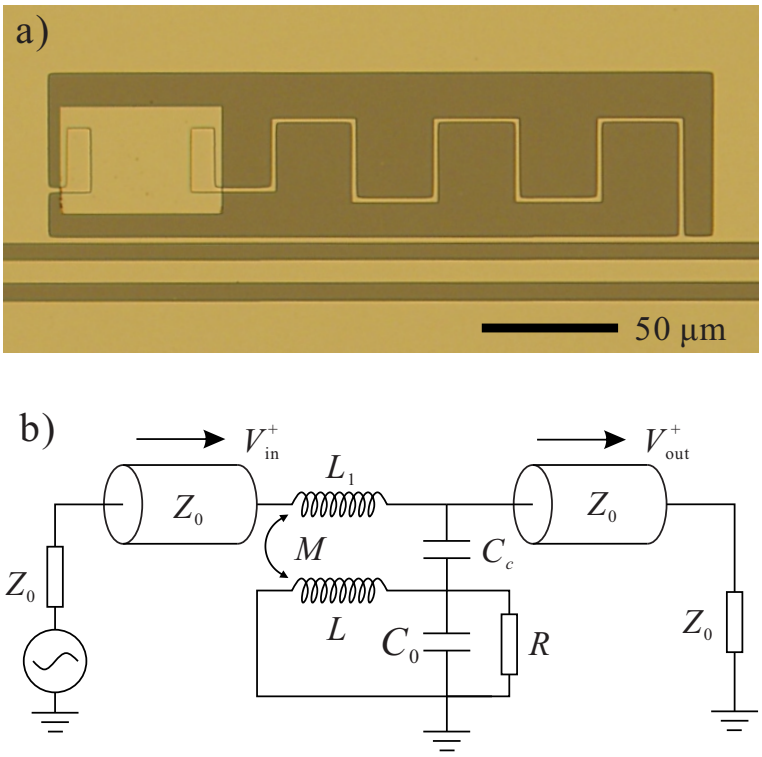



Figure 7.1: **Image of an LC resonator device and its circuit model.** (a) Optical microscope image of an LC resonator coupled to a transmission line, designed for measuring the loss tangent of the dielectric in the parallel-plate capacitor. The device is fabricated using two aluminum layers, patterned with electron-beam lithography. The dielectric is a 5 nm thick layer of $AlO_x$. The oxide is grown by applying oxygen plasma onto the bottom aluminum layer. The nominal capacitance value is 2.5 pF. (b) Lumped element circuit model for the device in (a). The estimated parameters of the lumped circuit elements are given in Table 7.1.

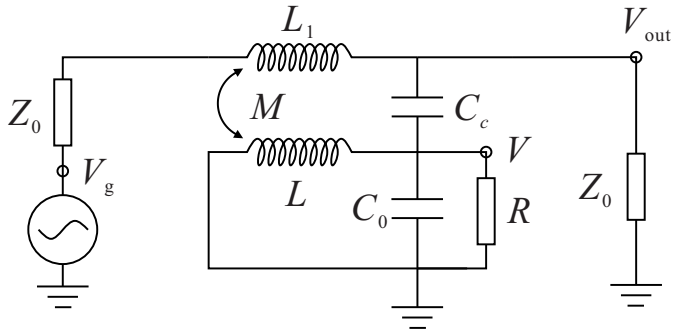



Figure 7.2: Equivalent circuit of the circuit showed in Fig. 7.1(b).

**Reduction of $S_{21}$ to a linear fractional form**

The S-parameter $S_{21}$ in Eq. (7.1) is in a polynomial fractional form of $\omega$. Our goal is to derive, in a systematic manner, a simpler approximate form of the $S_{21}$. Since $S_{21}$ is dimensionless, it is convenient to express it in terms of a set of dimensionless parameters. We choose the following dimensionless parameters:

$$\begin{aligned} \alpha = \frac{M}{L}, \quad \beta = \frac{L_1}{L}, \quad \gamma = \frac{C_c}{C_0}, \quad \xi = \frac{\sqrt{L/C_0}}{Z_0}, \\ q = 1/Q = \frac{1}{R\omega_0' C_0}, \quad \text{and} \quad x = 2R\omega_0' C_0 \left(\frac{\omega}{\omega_0'} - 1\right). \end{aligned} \tag{7.6}$$

Here $\omega_0' = 1/\sqrt{LC_0}$ is the resonance frequency of the uncoupled resonator. Coupling to the transmission line will result in a shift in the resonance frequency from $\omega_0'$. When expressed in terms of the new parameters, the expression for $S_{21}$ becomes:

$$S_{21} = \frac{f(x)}{g(x)} = \frac{a_0 + a_1 qx + a_2 (qx)^2}{b_0 + b_1 qx + b_2 (qx)^2 + b_3 (qx)^3 + b_4 (qx)^4} \tag{7.7}$$

where $f(x)$ and $g(x)$ are polynomial functions of $qx$. The expressions for the coefficients in Eq. (7.7) are given in Appendix E.

The dimensionless parameters in Eq. (7.6) are chosen such that their values are much smaller (i.e. $\alpha$, $\beta$, $\gamma$, and $q$) or comparable (i.e. $x$ and $\xi$) to unity, which allows for developing systematic order expansions. To illustrate this, in Table 7.1, we list realistic values of circuit parameters for a resonator realized in our experiments with an estimated bare

Table 7.1: Parameters of the circuit shown in Fig. 7.2.

| $L_1$ | $M$ | $L$ | $C_c$ | $C_0$ | $Z_0$ | $R$ |
|---|---|---|---|---|---|---|
| 0.71 pH | 12 pH | 290 pH | 5.0 fF | 2.5 pF | 50 Ω | 50 $k\Omega$ |

Table 7.2: Reduced parameters.

| $\alpha$ | $\beta$ | $\gamma$ | $\xi$ | $q$ |
|---|---|---|---|---|
| 0.041 | 0.0025 | 0.0020 | 0.21 | 0.00021 |

resonance frequency $\omega_0' = 2\pi \times 5.9$ GHz. These circuit parameter values are estimated using electromagnetic field simulation tools. Corresponding values of the reduced parameters are shown in Table 7.2. We note that while all the reduced parameters are small, $q$ may be smaller than one by many orders of magnitude (the quality factor of a superconducting resonator often reaches $10^6$ especially when driven at high power). For resonators weakly coupled to the transmission line, we expect that the resonance frequency and the width of the resonance are not perturbed very strongly. For this reason, the relevant range of the variable $x = 2Q\frac{\omega-\omega_0'}{\omega_0'}$ corresponds to $|x| \lesssim 1$.

Since $qx$ is a number much smaller than the rest of the parameters, we can approximate $f(x)$ and $g(x)$ by keeping only the terms up to the first order of $qx$, which gives:

$$\tilde{S}_{21} = \frac{\tilde{f}(x)}{\tilde{g}(x)} = \frac{a_0 + a_1 qx}{b_0 + b_1 qx}. \tag{7.8}$$

Fig. 7.3 illustrates the accuracy of the approximation above by comparing both the amplitude and phase of $S_{21}$ and $\tilde{S}_{21}$ using realistic circuit parameters given in Table 7.1. Noting that both $\tilde{f}(x)$ and $\tilde{g}(x)$ contain terms up to the first order in $x$, we rearrange the terms and write $\tilde{S}_{21}$ in the following linear fractional form:

$$\tilde{S}_{21} = |A_0|e^{j\phi}\frac{a + jx}{b + jx}. \tag{7.9}$$

where $a = \frac{j}{q}\frac{a_0}{a_1}$, $b = \frac{j}{q}\frac{b_0}{b_1}$, $|A_0|e^{j\phi} = a_1/b_1$. We note that the parameter $|A_0|e^{j\phi}$ has a value which is very close to 1. For this reason it would be difficult to distinguish this factor from attenuation and gain factors in the measurement setup. Therefore, we simply drop this factor from now on. The expressions for $a$ and $b$ are ratios of polynomials, depending on all the reduced parameters, given in Appendix E. We rewrite next the parameters $a$ and $b$ in a way which makes the dependence on $q$ explicit. We have:

$$a = A + j\frac{B}{q}, \tag{7.10}$$

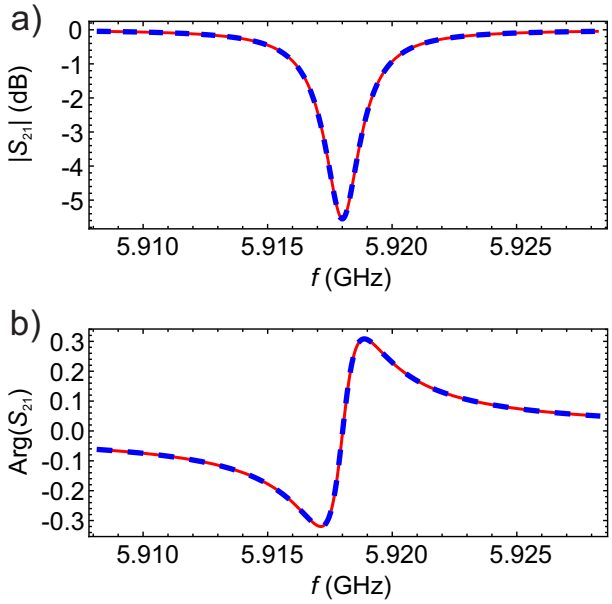



Figure 7.3: **Exact and reduced $S_{21}$ of a resonator.** Amplitude (a) and phase (b) of the exact $S_{21}$ (red solid line) and the reduced linear fractional form $\tilde{S}_{21}$ (blue dashed line). The expressions are defined in Eqs. (7.7) and (7.8), respectively.

and

$$b = C + \frac{D}{q} + j(E + \frac{F}{q}), \tag{7.11}$$

where $A$, $B$, $C$, $D$, $E$ and $F$ depend on the reduced parameters other than $q$.

We simplify the coefficients $A$, $C$, and $E$ by using a Taylor expansion in terms of $\alpha$ and $\gamma$, which characterizes the resonator coupling and are therefore very small. We obtain:

$$A = 1 + O(\alpha, \gamma), \tag{7.12}$$
$$C = 1 + O(\alpha, \gamma), \tag{7.13}$$
$$E = O(\alpha, \gamma). \tag{7.14}$$

For the purpose of order comparisons, we also write down the series expansion of $B$, $D$, and $F$ below:

$$B = \gamma - \alpha\gamma - \gamma^2 + \cdots, \tag{7.15}$$
$$D = \frac{(2 + \beta\xi^2 + \beta^2\xi^2)}{\xi(4 + \beta^2\xi^2)}\gamma^2 + \frac{2\xi}{4 + \beta^2\xi^2}(\alpha^2 - \beta\alpha\gamma) + \cdots, \tag{7.16}$$
$$F = \gamma + \frac{-8 + 2\beta - 3\beta^2\xi^2}{2(4 + \beta^2\xi^2)}\gamma^2 - \frac{4\gamma\alpha + \beta\xi^2\alpha^2}{4 + \beta^2\xi^2} + \cdots. \tag{7.17}$$

These expansions are carried out using *Mathematica* [36]. We find that $B$, $D$, and $F$ are at least in the second order of $\alpha$ and $\gamma$. For high-Q resonators($q \ll \alpha, \gamma$), we only retain the zeroth order terms for $A$, $C$, $E$. First order terms for $A$, $C$, and $E$ are not needed, due to the large $B/q$, $D/q$, and $F/q$ terms. With these approximations, the function $\tilde{S}_{21}$ takes the form:

$$\tilde{S}_{21,\text{red}} = \frac{1 + j\frac{B}{q} + jx}{1 + \frac{D}{q} + j\frac{F}{q} + jx}. \tag{7.18}$$

The resonance curve described by Eq. (7.18) is asymmetric in general. We identify the resonance frequency as the value when $|\tilde{S}_{21,\text{red}}|$ is minimized. The resonance frequency $\omega_0$ depends on the internal loss of the capacitor (details shown in Appendix E). However, for high-Q resonators, this dependence is weak for $q \ll 0$. For simplicity, we take the resonance frequency as the resonance frequency without internal loss ($q = 0$) as the following:

$$\omega_0 = \omega_0'(1 - B/2), \tag{7.19}$$

where

$$B = \frac{\gamma(1 - \alpha)}{1 + \gamma - \alpha\gamma}. \tag{7.20}$$

The internal quality factor is defined as

$$Q_i = \omega_0 R C_0 = \omega_0'(1 - B/2) R C_0 \tag{7.21}$$

$$= \frac{1 - B/2}{q}. \tag{7.22}$$

We rewrite Eq. (7.18), showing specifically the resonance frequency $\omega_0$ and the internal quality factor $Q_i$ to

$$\tilde{S}_{21,\text{red}} = \frac{1 + 2jQ_i\frac{\omega-\omega_0}{\omega_0}}{1 + \frac{Q_i}{Q_e} + j\frac{Q_i}{Q_\alpha} + 2jQ_i\frac{\omega-\omega_0}{\omega_0}}, \tag{7.23}$$

with $Q_\alpha$ and $Q_e$ defined as the following expressions:

$$Q_\alpha = \frac{1 - B/2}{F - B}, \tag{7.24}$$

$$Q_e = \frac{1 - B/2}{D}. \tag{7.25}$$

The reduced $S_{21}$ in Eq. (7.23) is in a form which is similar to a Lorentzian. $Q_\alpha$ is a parameter that characterizes the asymmetry of $S_{21}$ with respect to the resonance frequency. In the limit where $Q_\alpha \to \infty$, $\omega_0(Q_i^{-1}+Q_e^{-1})$ is the width of the transmission signal in the frequency domain. Therefore, $Q_e$ is the external quality factor of the resonator.

Eq. (7.23) is the main result of this section. By fitting Expression (7.23) to $S_{21}$ data, we can uniquely determine the fitting parameters $\omega_0$, $Q_i$, $Q_e$, and $Q_\alpha$. It is also worth to point out that Eq. (7.23) has the same form as to Eq. (3) in Ref. [93] and it can be transformed into Eq. (13) in Ref. [103] by redefining parameters as the following:

$$\begin{aligned}
\widetilde{\omega}_0 &= \omega_0\left(1 - \frac{1}{2Q_\alpha}\right), \\
\widetilde{Q}_i &= Q_i\left(1 - \frac{1}{2Q_\alpha}\right), \\
\widetilde{\hat{Q}}_e^{-1} &= 1/Q_e + j/Q_\alpha, \\
\widetilde{Q}^{-1} &= 1/Q_e + 1/Q_i,
\end{aligned} \tag{7.26}$$

where $\widetilde{\omega}_0$, $\widetilde{Q}_i$, $\widetilde{\hat{Q}}_e$, and $\widetilde{Q}$ are parameters defined in Ref. [103]. The difference in expressions of the resonance frequency is due to the fact that Ref. [103] considers the resonance frequency as the frequency at maximum $|V|$ while we consider it as the frequency at minimum $|S_{21}|$. In Subsection 7.1.4, we discuss the more general arguments that justify our

systematic approach. We show there that this method approximates the S-parameter from a complex function with multiple poles and zeros to a reduced form governed by only one pole and one zero whose real parts are the closest to the resonance frequency. We call this method the Closest Pole and Zero Method (CPZM).

### 7.1.2 Voltage on lumped element capacitor

Characterizing the field dependence of dielectric loss is essential in understanding the loss mechanism of dielectrics. For amorphous dielectric materials, tunneling two-level systems (TTLS) [106, 104] are believed to constitute the dominant source of loss in the quantum regime. The TTLS model has detailed predictions of the loss dependence on the AC electric field in the dielectric. In a LC superconducting resonator, the electric field in the dielectric is proportional to the voltage $V$ on the capacitor.

Using circuit theory, we can determine $V(Q_i, V_{\text{in}}^+)$, with $Q_i$ the resonator internal quality factor and $V_{\text{in}}^+$ the voltage of the forward propagating wave towards the resonator input port. If $Q_i$ is a constant or the circuit is strongly coupled to the transmission line, $V$ is proportional to $V_{\text{in}}^+$. The experimentally measured $(Q_i, V_{\text{in}}^+)$ dependence is transformed into a $(Q_i, V)$ dependence assuming a constant ratio $V/V_{\text{in}}^+$. In this section we develop a systematic method to express the dependence of $V$ on $V_{\text{in}}^+$ in a way which takes into account the voltage dependence of the quality factor. We find that the $(Q_i, V)$ dependence determined in this way is different than the case when $V/V_{\text{in}}^+$ is simply assumed constant. The difference is more than a trivial scaling factor, and has an effect on the exponents appearing in the voltage dependence of the loss for realistic circuits.

Starting from Eq. (7.2), we introduce $v(\omega) = V/V_{\text{in}}^+$ and express it using the dimensionless parameters introduced in Eq. (7.6). In terms of the reduced parameters introduced earlier, $v$ is a high order polynomial fractional form $v = f_v(x)/g_v(x)$ (see Eq. (E.2) in Appendix E for the full expression of $v$). We apply our CPZM to approximate $v$ to $\tilde{v}$, a linear fractional form of $q$:

$$\tilde{v} = \frac{\tilde{f}_v(x)}{\tilde{g}_v(x)} = \frac{c_0 + c_1 q x}{d_0 + d_1 q x}, \tag{7.27}$$

with $\tilde{f}_v(x)$ and $\tilde{g}_v(x)$ containing terms up to first order in $x$. Fig.7.4 illustrates the accuracy of the approximation above by comparing both the amplitude and phase of $v$ and $\tilde{v}$ using realistic circuit parameters given in Table 7.1. We rewrite $\tilde{v}$ as

$$\tilde{v} = \zeta \frac{a' + jx}{b' + jx}, \tag{7.28}$$

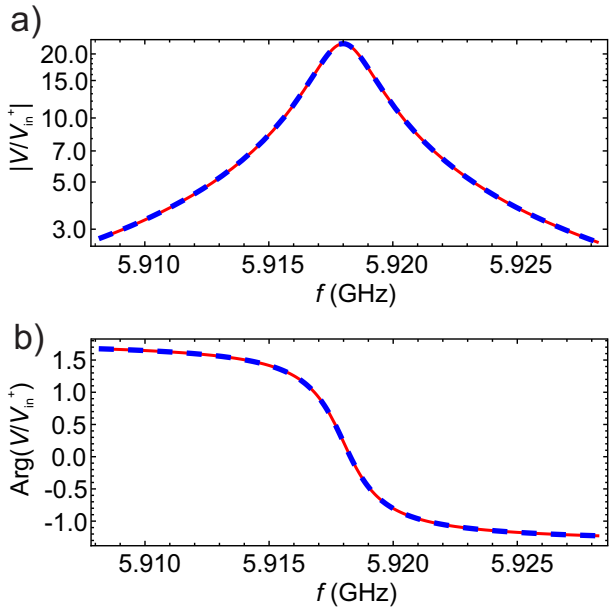



Figure 7.4: **Exact and reduced $V/V_{\mathbf{in}}^{+}$ of a resonator.** Amplitude (a) and phase (b) of the exact $V/V_{\text{in}}^{+}$ (red solid line) and the reduced linear fractional form $\tilde{v}$ (blue dotted line).

where $\zeta = c_1/d_1$, $a' = \frac{j}{q}\frac{c_0}{c_1}$ and $b' = \frac{j}{q}\frac{d_0}{d_1}$. Separating $q$ from the rest of the reduced parameters gives

$$\tilde{v} = \zeta \frac{K/q + jJ/q + jx}{H + N/q + j(O + P/q) + jx}. \tag{7.29}$$

Interestingly, some of the coefficients in the above equation are exactly the same as those in the $\tilde{S}_{21}$ formula given by Eq. (7.23). We have $H = C$, $N = D$, $O = E$, and $P = F$. Since it is the features of the near-resonance transmission that allow one to extract $Q_i$, we calculate the value of $\tilde{v}(\omega)$ for $\omega = \omega_0$. At this frequency, $x = \frac{2}{q}(\omega_0/\omega_0' - 1) = -\frac{B}{q}$. We obtain:

$$\left.\frac{V}{V_{\text{in}}^{+}}\right|_{\omega=\omega_0} \approx \tilde{v}_0 = \frac{\lambda}{q_i + q_e + jq_\alpha} \tag{7.30}$$

where $q_i = 1/Q_i$, $q_e = 1/Q_e$, $q_\alpha = 1/Q_\alpha$ and

$$\lambda = \zeta \frac{K + j(J - B)}{1 - B/2}. \tag{7.31}$$

$\lambda$ is a scaling factor which does not depend on internal quality factor of the resonator. The full form of $\lambda$ is given by Eq. (E.28) in Appendix E.

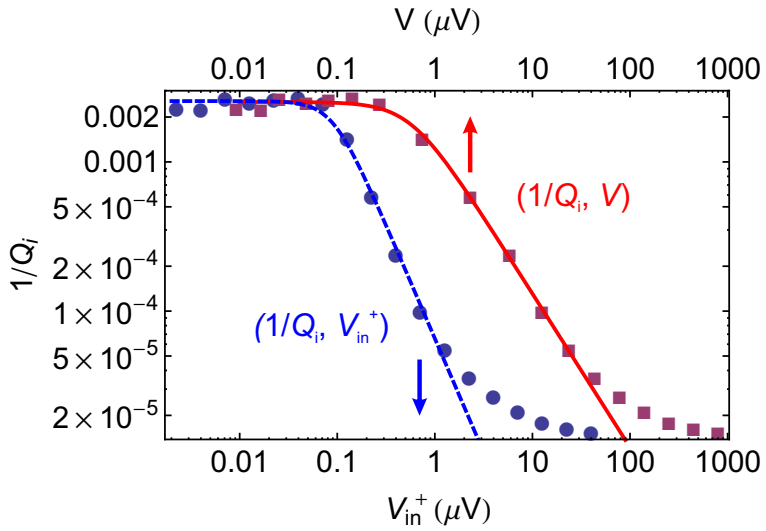



Figure 7.5: **Experimentally measured loss dependence on $V_{\text{in}}^+$ (blue dots) and on $V$ (red squares).** The red line is a result of fitting Eq. (7.33) to $(V, Q_i)$ which yields $\Delta = -0.0613$ and $Q_{i,0} = 397$. The blue dashed line is a result of fitting Eq. (7.33) to $(V_{\text{in}}^+, Q_i)$ which yields $\Delta = -1.05$ and $Q_{i,0} = 391$.

To estimate this scaling factor, we write $\lambda$ as a Taylor series of small numbers $\gamma$, $\alpha$, and $\beta$ to their first orders, which gives

$$\lambda = -\alpha\xi + j\gamma + \cdots , \tag{7.32}$$

where $\xi$ has a quantity which can be comparable to unity. We approximate the expression above further to $\lambda \approx -M\omega_0'/Z_0 + jC_c/C_0 \approx -M\omega_0/Z_0 + jC_c/C_0$. Given that $\omega_0$ can be obtained from fitting the $S_{21}$ data and $Z_0$ is usually assumed to be 50 $\Omega$, we only need to estimate circuit parameters, $M$, $C_c$, and $C_0$, for determining $\lambda$.

In experiments, one measures the $S_{21}$ at various values of $V_{\text{in}}^+$. For each value of $V_{\text{in}}^+$, a corresponding $Q_i$ is obtained from fitting Eq. (7.23) to the $S_{21}$ data. $Q_e$, $Q_\alpha$, and $\omega_0$ are obtained from the fit as well. Then one can use Eq. (7.30) to transform data set $(V_{\text{in}}^+, Q_i)$ into $(V, Q_i)$. To illustrate the difference between the above two data sets, we plot in Fig. 7.5 the experimental $(V_{\text{in}}^+, Q_i)$ data of the parallel plate LC resonator shown in Fig. 7.1(a) and the corresponding $(V, Q_i)$ data transformed with Eq. (7.30) with $Q_e = 1984$, $Q_\alpha = 4128$, $\omega_0 = 2\pi \times 7.665$ GHz, and $\lambda = 0.01146$. The dielectric layer between the paralleled plates is made of aluminum oxide, whose quantum regime loss is believed to be due to the TTLSs.

According to Ref. [104], the TTLS loss at a constant temperature is predicted to be

$$\frac{1}{Q_i} = \frac{1/Q_{i,0}}{\sqrt{1+(V/V_c)^{2-\Delta}}} \tag{7.33}$$

with $\Delta = 0$. We fit Eq. (7.33) to both $(V, Q_i)$ and $(V_{\text{in}}^+, Q_i)$ data. We note that the fit to $(V, Q_i)$ yields $\Delta = -0.0613$, which is a very good agreement with the TTLS model while the fit to $(V_{\text{in}}^+, Q_i)$ yields $\Delta = -1.05$. As a result, the transformation from $V_{\text{in}}^+$ to $V$ with the loss of the resonator taken into account is crucial for determining the voltage dependence of dielectric loss. However, we find from Eq. (7.30) that $V$ is approximately proportional to $V_{\text{in}}^+$ in the over-coupled limit, $Q_i \gg Q_e$. In this case, the fits to $(V, Q_i)$ and $(V_{\text{in}}^+, Q_i)$ will give approximately the same exponents $\Delta$.

### 7.1.3 Explanation of asymmetric transmission

Although the function given in Eq. (7.23) fits the experimental data very well, the amount of transmission asymmetry characterized by $Q_\alpha$ cannot always be explained by the circuit model in Fig. 7.1(b) with a set of realistic parameters. Fig. 7.6 shows two $|S_{21}|$ curves, of LC resonators measured in our experiments, which are highly asymmetric. A similar, large, asymmetry was observed in experiments of Geerlings et al. [92] and Megrant et al [93]. Khalil et al. [103] attribute this effect to an on-chip inductor and transmission line impedance mismatches. Our experiments indicate a very large transmission line impedance mismatch is required to explain the asymmetry transmission, which is unlikely to occur in our setup. Motivated by this observation, we analyze a more complete circuit model, shown in Fig. 7.7. In this model we take into account the connections between transmission lines on chip and outside the chip, implemented with bonding wires. We model these using inductances $L_{\text{in}}$ and $L_{\text{out}}$. These connections act as reflection points for the propagating microwaves. The two parts of the on-chip transmission lines, between the bonding connection and the resonator, are assumed to have characteristic impedance $Z_{\text{in/out}}$ and length $l_{\text{in/out}}$ respectively.

For such a circuit, consisting of several two-port components, it is convenient to use the ABCD transmission matrix method [24]. The ABCD matrix $\mathbf{T}$ of a general 2-port circuit is defined as

$$\begin{pmatrix} V_{\text{in}} \\ I_{\text{in}} \end{pmatrix} = \mathbf{T} \begin{pmatrix} V_{\text{out}} \\ I_{\text{out}} \end{pmatrix} \tag{7.34}$$

where $V_{\text{in/out}}$ and $I_{\text{in/out}}$ are the voltages and currents at the input and output port respectively. We first use Kirchhoff's law to calculate the ABCD transmission matrix of the

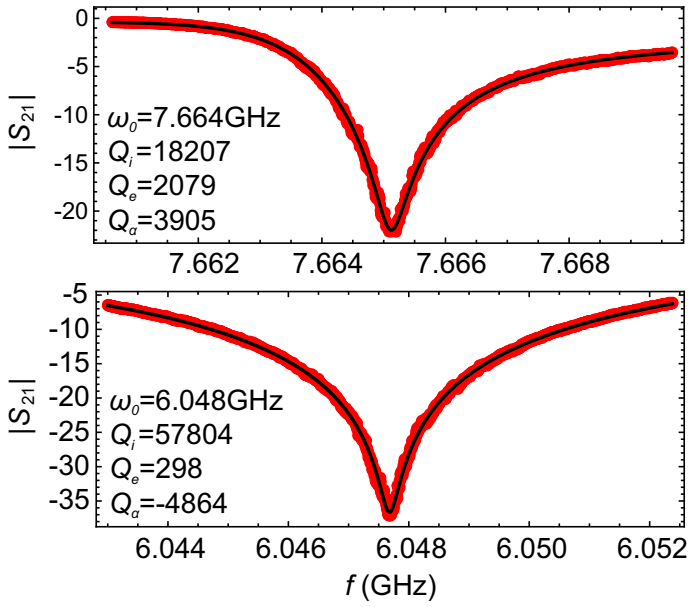



Figure 7.6: **Measured transmission curves with different types of asymmetries**. The Measured transmission curves (red dots) for two resonators on the same chip are fitted by Eq. (7.23) (black lines). The extracted fit parameters are indicated in the graph legends. The asymmetric line shape corresponding to a positive (negative) $Q_\alpha$ is shown in the upper (lower) panel.

resonator part of the circuit (see Fig. 7.7 for the circuit schematics). We write down the circuit equations which relate the voltages, $V_1$ and $V_2$, and the currents, $I_1$ and $I_2$, to the capacitance voltage $V$ as follows:

$$V_1 - V_2 = j\omega L_1 I_1 - j\omega M \frac{V + j\omega M I_1}{j\omega L}, \tag{7.35}$$

$$V_2 - V = -\frac{1}{j\omega C_c}(I_2 - I_1), \tag{7.36}$$

$$\frac{V(j\omega R C_0 + 1)}{R} + \frac{V + j\omega M I_1}{j\omega L} = I_1 - I_2. \tag{7.37}$$

Based on these equations we can derive the ABCD matrix for the circuit

$$\mathbf{T}_{\text{res}} = \begin{pmatrix} T_A & T_B \\ T_C & T_D \end{pmatrix} \tag{7.38}$$

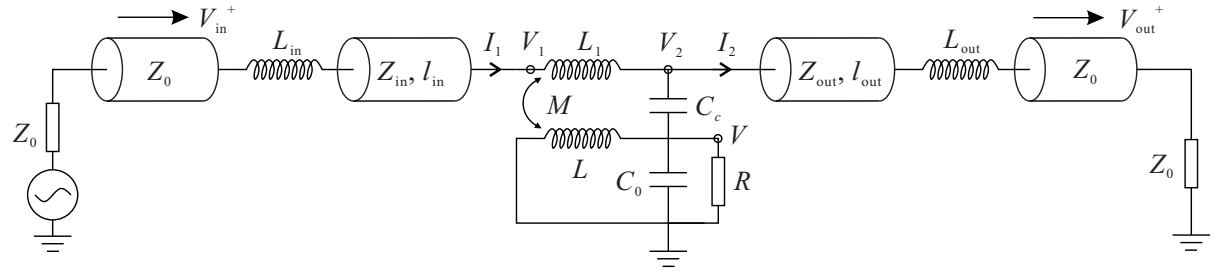



Figure 7.7: **Circuit model of a LC resonator coupled to a non-ideal transmission line.** The on-chip CPW transmission line close to the input/output port has length $l_{\text{in/out}}$ and characteristic impedance $Z_{\text{in/out}}$. They are connected to the input/output port through wire bonds modeled by inductance $L_{\text{in/out}}$. Both the input and output ports are terminated with an impedance $Z_0$.

where

$$T_A = \frac{-j\omega\left(L - C_c L L_1 \omega^2 + C_c M^2 \omega^2\right) + R\left(-1 + \left(C_0 L + C_c(L + L_1 - 2M)\right)\omega^2 + C_0 C_c\left(-L L_1 + M^2\right)\omega^4\right)}{-jL\omega + R\left(-1 + \left((C_0 + C_c)L - C_c M\right)\omega^2\right)}, \tag{7.39}$$

$$T_B = \frac{\omega\left(-jL_1 R + \left(L L_1 - M^2\right)\omega + j(C_0 + C_c)\left(L L_1 - M^2\right)R\omega^2\right)}{-jL\omega + R\left(-1 + \left((C_0 + C_c)L - C_c M\right)\omega^2\right)}, \tag{7.40}$$

$$T_C = \frac{C_c\omega\left(L\omega + jR\left(-1 + C_0 L\omega^2\right)\right)}{-jL\omega + R\left(-1 + \left((C_0 + C_c)L - C_c M\right)\omega^2\right)}, \tag{7.41}$$

$$T_D = \frac{-jL\omega + R\left(-1 + (C_0 + C_c)L\omega^2\right)}{-jL\omega + R\left(-1 + \left((C_0 + C_c)L - C_c M\right)\omega^2\right)}. \tag{7.42}$$

For the other parts of the circuit, the ABCD matrixes of the wire bond inductors are

$$\mathbf{T}_{L_\alpha} = \begin{pmatrix} 1 & j\omega L_\alpha \\ 0 & 1 \end{pmatrix} \tag{7.43}$$

and the ABCD matrixes for the two pieces of the transmission lines between wire bonds and the resonator are

$$\mathbf{T}_{TL_\alpha} = \begin{pmatrix} \cos\beta_\alpha l_\alpha & jZ_\alpha \sin\beta_\alpha l_\alpha \\ j\sin\beta_\alpha l_\alpha / Z_\alpha & \cos\beta_\alpha l_\alpha \end{pmatrix}, \tag{7.44}$$

where $\alpha$ can stand for "in" or "out", $\beta_\alpha = \omega\sqrt{\tilde{L}_\alpha \tilde{C}_\alpha}$, and $\tilde{L}_\alpha$ and $\tilde{C}_\alpha$ are the characteristic inductance and capacitance of the transmission line. We define the time, for microwave to

propagate $l_\alpha$ in distance, as $t_\alpha = l_\alpha\sqrt{\tilde{L}_\alpha\tilde{C}_\alpha}$. Given the width of the resonance $\delta\omega \ll 2\pi/t_\alpha$, we can approximate $\mathbf{T}_{\mathrm{TL}_\alpha}$ to an $\omega$-independent ABCD matrix

$$\tilde{\mathbf{T}}_{\mathrm{TL}_\alpha} = \begin{pmatrix} \cos\omega_0' t_\alpha & jZ_\alpha \sin\omega_0' t_\alpha \\ j\sin\omega_0' t_\alpha / Z_\alpha & \cos\omega_0' t_\alpha \end{pmatrix} \tag{7.45}$$

in the vicinity of $\omega = \omega_0'$. In the end, we obtain the ABCD matrix of the complete circuit by multiplying all the ABCD matrices:

$$\begin{aligned} \mathbf{T}_{\mathrm{all}} =& \mathbf{T}_{L_{\mathrm{in}}}\mathbf{T}_{\mathrm{TL_{in}}}\mathbf{T}\mathbf{T}_{\mathrm{TL_{out}}}\mathbf{T}_{L_{\mathrm{out}}} & (7.46)\\ \approx& \mathbf{T}_{L_{\mathrm{in}}}\tilde{\mathbf{T}}_{\mathrm{TL_{in}}}\mathbf{T}\tilde{\mathbf{T}}_{\mathrm{TL_{out}}}\mathbf{T}_{L_{\mathrm{out}}}. & (7.47)\end{aligned}$$

The scattering matrix element $S_{21}$ can be calculated from the ABCD matrix using the following equation:

$$S_{21}' = \frac{2}{T_{\mathrm{all},A} + T_{\mathrm{all},B}/Z_0 + T_{\mathrm{all},C}Z_0 + T_{\mathrm{all},D}}, \tag{7.48}$$

where $T_{\mathrm{all},a}$ with $a = A$, $B$, $C$, or $D$ is each of the matrix elements of $\mathbf{T}_{\mathrm{all}}$.

In Fig. 7.8, we plot $S_{21}'$ in Eq. (7.48) using $L_{\mathrm{in}} = L_{\mathrm{out}} = 370$ pH, $Z_{\mathrm{in}} = Z_{\mathrm{out}} = 50\ \Omega$, and parameters in Table 7.1. These values of the inductance were determined based on numerical simulations of transmission through wire bonds with a 1 mm length. Fig. 7.8 shows that $S_{21}'$ with different $\theta_{\mathrm{in}} = t_{\mathrm{in}}\omega_0'$ and $\theta_{\mathrm{out}} = t_{\mathrm{out}}\omega_0'$ can have different amount of asymmetry with different signs. In the multiplexed resonator measurement design, a number of resonators are coupled to the same transmission line. Since their positions relative to the reflection points (wire bonds here) and their resonance frequencies are different, the asymmetry feature of their transmission could also be different. This is what we observe in the experiment, which strengthens the hypothesis of our wire bond reflection model. The asymmetry is essentially due to reflections at the connection points which leads to weak standing waves with a length and frequency dependent pattern.

Finally, we apply our approximation procedure shown in Subsection 7.1.1 to this more complicated model and simplify the transmission $S_{21}'$ in Eq. (7.48). We find that we reach a similar form to Eq. (7.18), which is given by

$$\tilde{S}_{21,\mathrm{red}}' = \frac{1 + j\frac{B}{q} + jx}{1 + \frac{D'}{q} + j\frac{F'}{q} + jx}. \tag{7.49}$$

In the equation above, $B$ is exactly the same as in Eq. (7.20). $D'$ and $F'$ are $q$-independent parameters. By using definition $\omega_0 = \omega_0'(1 - B/2)$ and $Q_i = \omega_0 RC_0$ which are the same as

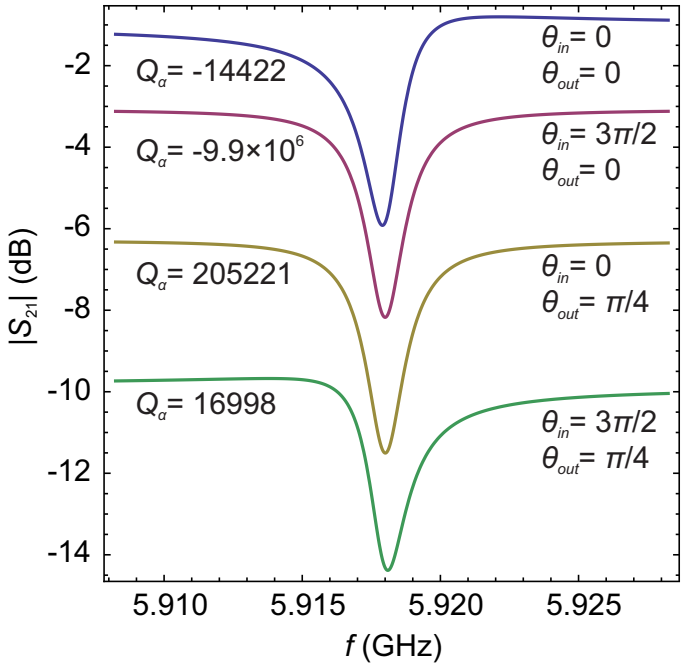



Figure 7.8: **The asymmetric resonance calculated using different values of transmission line electrical length $t_{\mathbf{in/out}}$.** Here $\theta_{\mathrm{in/out}} = \omega_0' t_{\mathrm{in/out}}$. Each curve has an incremental offset of $-3$ dB. The asymmetry degree parameter $Q_\alpha$ is calculated for each curve. The symmetric $|S_{21}|$ case corresponds to $Q_\alpha \to \infty$.

Eq. (7.19) and Eq. (7.21), and definitions $Q'_e = (1-B/2)/(F'-B)$ and $Q'_\alpha = (1-B/2)/D'$ which are similar to Eq. (7.25) and (7.24), we obtain

$$\tilde{S}'_{21,\mathrm{red}} = \frac{1 + 2jQ_i\frac{\omega-\omega_0}{\omega_0}}{1 + \frac{Q_i}{Q'_e} + j\frac{Q_i}{Q'_\alpha} + 2jQ_i\frac{\omega-\omega_0}{\omega_0}} \tag{7.50}$$

which has the same form as Eq. (7.23). The parameters $Q'_e$ and $Q'_\alpha$ here are different from the corresponding $Q_e$ and $Q_\alpha$ in Eq. (7.23). They in general depend on more circuit parameters, i.e. $L_{\mathrm{in/out}}$, $Z_{\mathrm{in/out}}$ and $l_{\mathrm{in/out}}$, in addition to those circuit parameters in Table 7.1. By fitting Eq. (7.50), the intrinsic quality factor $Q_i$ and the resonance frequency $\omega_0$ can be determined reliably.

We emphasize that the same $Q_i$ and $\omega_0$ appear in both Eq. (7.23) and Eq. (7.50) despite different external circuits coupled to the resonator. This shows that the impedance mismatch and wave reflection in the transmission line considered in this case does not compromise the determination of the internal quality factor $Q_i$.

### 7.1.4 Generalization to other resonance circuits

In this section we discuss the general application of CPZM to lumped and distributed resonators. We start with the consideration of lumped resonators. In this case, the response function (be it the transmission, reflection, or the ratio between voltages of any points) can be expressed as a polynomial ratio:

$$R(\omega) = \frac{N(\omega)}{D(\omega)}, \tag{7.51}$$

where $N(\omega)$ and $D(\omega)$ are polynomials, of degree $m$ and $n$ respectively. We can factor both polynomials to obtain

$$R(\omega) = R_0 \times \frac{\prod_{i=0}^{n-1}(\omega - z_i)}{\prod_{j=0}^{m-1}(\omega - p_i)} \tag{7.52}$$

with $R_0$ a complex number and $z_i$ and $p_i$ zeros and poles of the response function $R(\omega)$. The entire resonance behavior of the circuit is described by the positions of the zeros and poles and the complex scaling factor. Let us consider the response of the resonator close to one of its bare resonances, at frequency $\omega'_0$. If the resonator is weakly coupled to its measurement setups, we expect that the resonant behavior will be reflected by a zero

and/or a pole of $R(\omega)$ which are close to $\omega_0'$. We denote the closest zero and pole by $z_0$ and $p_0$. The response function can be expressed in the following form:

$$R(\omega) = \frac{\bar{N}(\omega)(\omega - z_0)}{\bar{D}(\omega)(\omega - p_0)}, \tag{7.53}$$

where $\bar{N}(\omega)$ and $\bar{D}(\omega)$ are polynomials with roots $z_{i\neq 0}$ and $p_{i\neq 0}$ respectively. For the near-resonance response of high-Q resonators, $\bar{N}(\omega)$ and $\bar{D}(\omega)$ are approximately constants within range, $\omega_0' - \delta\omega \lesssim \omega \lesssim \omega_0' + \delta\omega$, where $\delta\omega = \omega_0'/Q$. They can be well approximated with their values at $\omega = \omega_0'$. Therefore, the response function is reduced to

$$\tilde{R}(\omega) = \frac{\bar{N}(\omega_0')}{\bar{D}(\omega_0')} \frac{(\omega - z_0)}{(\omega - p_0)}. \tag{7.54}$$

This approximate response function $\tilde{R}(\omega)$ only depends on the zero and pole $z_0$ and $p_0$ in addition to a complex scaling factor $\frac{\bar{N}(\omega_0')}{\bar{D}(\omega_0')}$. The response function $\tilde{R}(\omega)$ is asymmetric in general while a symmetric response function requires $\Re[z_0] = \Re[p_0]$ (see Fig. 7.9). We note that any experimental measured frequency response, e.g. S-parameters, of a high-Q resonator can be fitted using Eq. (7.54) with three complex numbers, the zero, the pole and the complex scaling factor, as the fitting parameters. We also note that the approximation we applied in Subsections 7.1.1, 7.1.2 and 7.1.3 for reduced expressions for $S_{21}$ and $V/V_{\text{in}}^+$ are equivalent to finding the approximate form of the closest pole $p_0$ and zero $z_0$ in Eq. (7.54).

For distributed resonators such as coplanar waveguide resonators, the response function is not simply a ratio of polynomials of $\omega$ but also depends on a wave propagation term $z = e^{j\omega\tau}$, where $\tau$ corresponds to the electrical length of the waveguide. The general response function can be written as

$$R(\omega) = \frac{N(\omega, z)}{D(\omega, z)}, \tag{7.55}$$

where $N(\omega, z)$ and $D(\omega, z)$ are polynomials of both $\omega$ and $z$. Provided $\delta\omega \times \tau \ll 2\pi$, we can take the first order expansion of $z$ as $z \approx e^{j\omega_0'\tau} + j\tau e^{j\omega_0'\tau}(\omega - \omega_0')$. Thus we approximate the near-resonance response of a certain harmonic of the distributed resonator into a ratio of polynomials. Then, the same procedure to reduce the response function to the linear fractional form in Eq. (7.54) can be applied. As a result, the CPZM is applicable to distributed resonators as well.

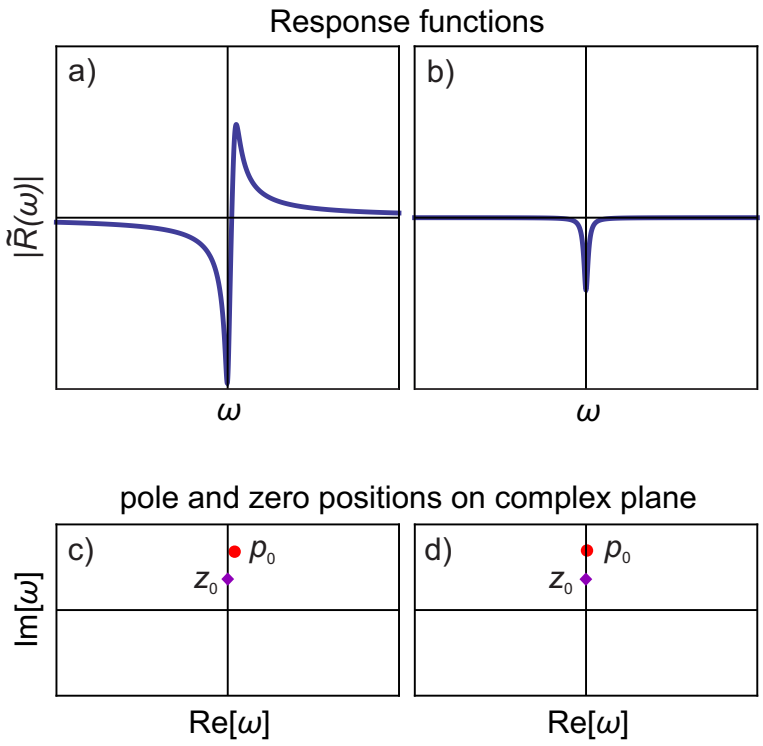



Figure 7.9: **Asymmetric and symmetric response functions.** We show an asymmetric (a) and symmetric (b) response function with its pole and zero plotted in the complex plane in (c) and (d) respectively.

### 7.1.5 Summary

We developed the Closest Pole & Zero Method (CPZM) for analyzing the near-resonance response of superconducting resonators. We showed that in the high-Q limit, the response functions are well described by a linear fractional form. We first considered the transmission S-parameter ($S_{21}$) of a lumped resonator. Using the CPZM, we obtained a linear fractional $S_{21}$ of this circuit. By fitting the linear fractional $S_{21}$, one can extract the resonance frequency, internal quality factor, and external quality factor out of the experimental measured transmission. We then applied the CPZM to analyze the relation between the capacitor voltage $V$ and the excitation voltage $V_{\text{in}}^{+}$ of the same circuit. We found that the ratio between $V$ and $V_{\text{in}}^{+}$ depends on all the fitting parameters of the transmission function, in particular the internal quality factor. Since the internal quality factor depends on $V$ itself due to the microscopic mechanism of the loss, $V$ is not proportional to $V_{\text{in}}^{+}$ in general. We presented a self-consistent method to calculate $V$ from the fitting results to the transmission S-parameter for every given $V_{\text{in}}^{+}$.

Moreover, we studied the case in which imperfections of the transmission lines used for S parameter measurements are modeled by introducing impedance mismatch and inductance from wire bonds. We found that the asymmetric transmission near the resonance is mainly caused by wave reflection on the wire bond positions. Using the CPZM, we showed that our fitting routine for extracting the internal quality factor applies to this non-ideal case as well.

We also discussed the general applications of the CPZM to high-Q resonance circuits. We showed that the response function of an arbitrary lumped or distributed resonator is or can be approximated by a ratio of polynomials. The ratio of polynomials can be approximated further to a linear factional form by finding its pole and zero closest to the bare resonance frequency of the resonator. We described the general procedure for such approximations.

The methods presented here provide a systematic and rigorous treatment of response functions of high quality factor resonators. They allow the reliable determination of the quality factor and electric field in driven resonators. These methods are applicable to a variety of experimental investigations of the mechanisms of dielectric loss in the quantum regime.

## 7.2 Characterization of microwave loss of thin aluminum oxide formed by plasma oxidation using superconducting resonators

Energy loss at microwave frequencies is one of the key aspects of the physics of amorphous dielectrics, a central topic in condensed matter research [107]. In recent years, renewed interest in this topic emerged in the field of superconducting quantum devices [15]. These devices unavoidably contain amorphous dielectrics, which are a significant source of decoherence [104, 108, 109, 98, 91]. Reduction of decoherence due to amorphous dielectrics can be achieved by their partial elimination, using suitably modified microwave circuit designs [93, 92, 96, 95]. However, these designs come at the cost of larger space and more difficult fabrication processes. Since the partial elimination of amorphous dielectrics has drawbacks, it is very relevant to investigate the physics of dielectric loss with the aim of reducing the intrinsic loss in these materials.

In this section, we present results on the fabrication and detailed characterization of microwave loss in thin films of amorphous aluminum oxide. This material is highly relevant in superconducting devices, since it forms the tunnel barrier in Josephson junctions. The films, obtained by plasma oxidation of a deposited aluminum layer, have a thickness of 5 nm. We fabricate overlap capacitors formed by the oxidized aluminum layer and a second aluminum layer. Microwave loss is measured based on lumped resonators which contain these overlap capacitors. Our characterization method is complementary to work on two-level spectroscopy using different types of superconducting qubits [104, 110, 111] and loss measurements based on coplanar waveguide resonators [112]. In addition, comparing microwave loss in plasma-grown aluminum oxide with loss in films fabricated using other methods, *i.e.* low pressure oxidation [104, 110, 111] (the standard method for fabrication of Josephson junctions) and deposition of aluminum in a reactive oxygen atmosphere [112], is relevant for understanding this material. We note that an aluminum oxide growth method similar to the method reported here was demonstrated in Ref. [113]. However, the temperature and power dependence of microwave loss in plasma grown oxide has not been previously characterized. The small thickness and the robustness of the aluminum oxide layers obtained in our work are relevant for microwave circuits with compact capacitors, especially in applications where relatively large loss can be tolerated, such as parametric amplifiers [114].

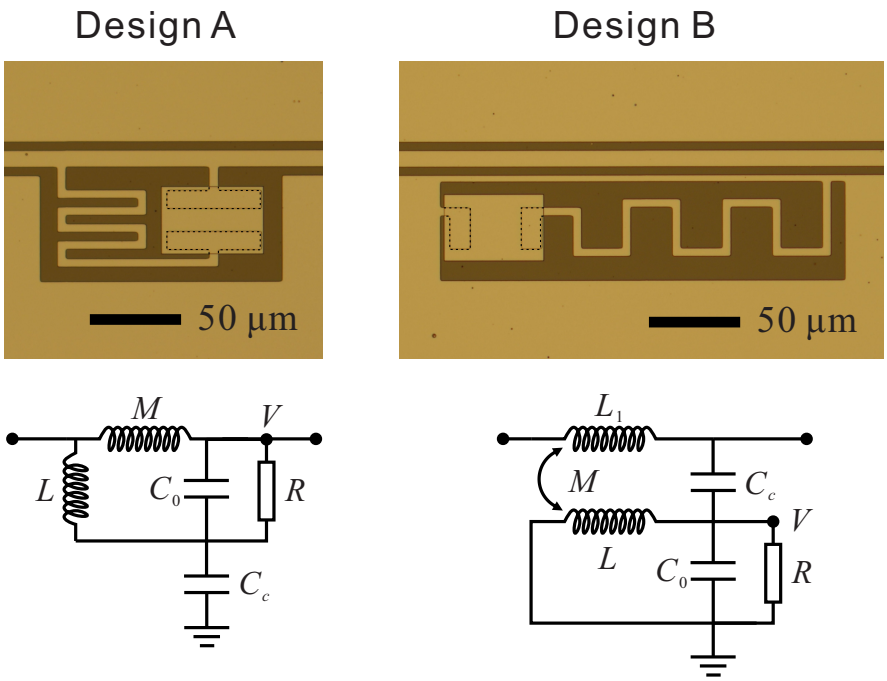



Figure 7.10: **Optical microscope images and circuit schematics of overlap-capacitor resonators with overcoupled (Design A) and undercoupled (Design B) designs.** The dashed lines in the microscope images indicate the contour of the capacitor bottom plates. In design A, the LC resonator is inductively coupled to a transmission line by sharing a part of the resonator loop with the center conductor of the transmission line. The microwave loss of the resonator is dominated by the external loss due to dissipation in the 50 Ω environment of the transmission line. In design B, the resonator is coupled to the transmission line via mutual inductance between the resonator loop and the center conductor of the transmission line. The loss of the resonator is dominated by the internal loss.

### 7.2.1 Experimental methods

We study dielectric loss using superconducting LC resonators formed of a meander inductor and an overlap capacitor containing aluminum oxide as a dielectric (see Fig. 7.10). The resonators are fabricated on thermally-oxidized high-resistivity silicon substrates. The fabrication process has three steps: (1) electron-beam deposition of an 100 nm aluminum layer through a mask defined by optical lithography, followed by lift-off; (2) plasma oxidation, to form an aluminum oxide layer on top of the aluminum film obtained in step 1; (3) electron-beam deposition of an 125 nm aluminum layer through an electron-beam defined mask, followed by lift-off. The plasma oxidation is performed at 200 °C at an oxygen pressure of 0.2 mbar for 5 minutes. With these oxidation parameters, we find a characteristic capacitance of 16 fF/$\mu$m$^2$ at room temperature. Electron-beam deposition and plasma oxidation are performed using a Plassys MEB 550S system.

We fabricated two nominally identical chips. Each chip contains a few lumped resonators, with different resonance frequencies, coupled to a common coplanar waveguide transmission line. We used two designs, A and B (see Fig. 7.10), which are overcoupled and undercoupled respectively. In addition, each chip contains one resonator based on an interdigital capacitor, which is used to determine an upper bound on other sources of loss. The parameters of the resonators are shown in Table 7.3. Transmission measurements are performed in a dilution refrigerator, using the system described in Ref. [32]. The input line has a total of 50 dB attenuation distributed at different temperature stages. The output line is equipped with two isolators and a high electron mobility transistor cryogenic amplifier with a noise temperature of 4 K. Measurements of the $S_{21}$ scattering parameter are performed using a vector network analyzer.

We use the method presented in Ref. [115] to relate the the $S_{21}$ scattering parameter to the resonator quality factors. We have:

$$S_{21}(\omega) = \frac{1 + 2iQ_i\frac{\omega-\omega_0}{\omega_0}}{1 + \frac{Q_i}{Q_e} + i\frac{Q_i}{Q_\alpha} + 2iQ_i\frac{\omega-\omega_0}{\omega_0}}, \tag{7.56}$$

where $Q_i$ is the internal quality factor, $Q_e$ is the external quality factor, $\omega_0$ is the resonance frequency, and $Q_\alpha$ is an asymmetry parameter of the resonator. We fit Eq. (7.56) to the $S_{21}$ data at each excitation voltage. In order to reliably determine the quality factor from the relatively noisy data at low excitation voltages, we first fit Eq. (7.56) to the data at high excitation voltage to determine $Q_e$, $Q_\alpha$, and the transmission baseline for each resonator. These parameters are independent of the loss of the resonators. Then the low power $S_{21}$ data is fitted with only $Q_i$ and $\omega_0$ as free parameters. The quality factor $Q_i$

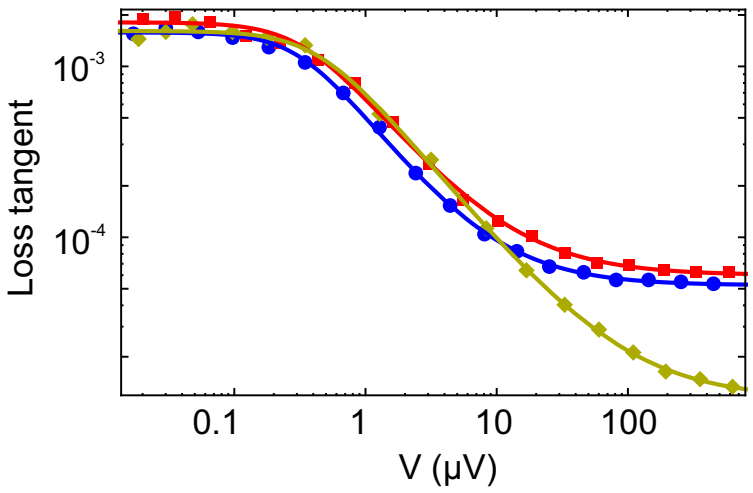



Figure 7.11: **Loss tangent versus voltage on capacitor,** for data of resonators on chip C1: LC1 at 4.9 GHz (blue dots), LC2 at 5.8 GHz (red squares), and LC3 at 6.2 GHz (yellow diamonds) and the fits with TLS model (Eq. (7.58)). The measurements are done at 54 mK.

of overlap capacitor resonators is a measure of the aluminum oxide loss tangent. Indeed, the resonators with interdigital capacitors have quality factors in the $10^5$ range, which is two orders of magnitude higher than that of the overlap capacitor resonators. This shows that sources of loss other than the dielectric in the overlap capacitor are negligible. We determine the loss tangent as a function of the voltage across the capacitor. The capacitor voltage $V$ can be related to the forward propagating voltage $V_{\text{in}}^{+}$ at the input port using the formula

$$V = V_{\text{in}}^{+} \times \frac{\lambda}{1/Q_i + 1/Q_e + i/Q_\alpha}, \tag{7.57}$$

where $\lambda$ is a coupling factor. The coupling factor $\lambda \approx M\omega_0/Z_0$, where $M$ is the mutual inductance between the resonator and the transmission line. The mutual inductance $M$ is 100 pH and 18 pH in design A and B respectively, as determined using numerical simulations.

### 7.2.2 Power dependence of dielectric loss

We first present the measurements of the dependence of dielectric loss on the voltage $V$. Fig. 7.11 shows the loss tangent versus the voltage on the overlap capacitors in different

| Chip | Resonator & design | $f_0$ (GHz) | $Q_e$ | $\tan\delta$ ($\times 10^{-3}$) | $Q_{\text{offset}}$ | $V_c(\mu V)$ |
|---|---|---|---|---|---|---|
| C1 | LC1, A | 4.91 | 336 | 1.54 | 19366 | 0.300 |
| C1 | LC2, A | 5.79 | 380 | 1.72 | 16245 | 0.371 |
| C1 | LC3, B | 6.16 | 3886 | 1.57 | 79194 | 0.534 |
| C2 | LC1, A | 5.03 | 310 | 1.75 | 38462 | 0.256 |
| C2 | LC2, A | 5.75 | 369 | 1.52 | 35397 | 0.424 |
| C2 | LC3, B | 6.08 | 3939 | 1.40 | 16805 | 0.399 |

Table 7.3: Summary of the measurement results of resonators on two different chips at 54 mK.

LC resonators at 54 mK. The loss saturates when the voltage on the capacitor corresponds to <0.1 photons stored in the resonator. The voltage dependence of the loss tangent is fitted to the two-level system (TLS) model [106, 104]:

$$\frac{1}{Q_i} = \frac{1}{Q_{\text{offset}}} + \frac{\tan\delta}{\sqrt{1+(V/V_c)^2}}, \tag{7.58}$$

where $\tan\delta$ is the loss tangent of the dielectric in the sub-single photon regime, $V_c$ is a critical voltage, and $Q_{\text{offset}}$ represents a voltage-independent loss likely due to quasiparticles excited by stray thermal radiation. Table 7.3 is a summary of the measurements of different resonators on the two fabricated chips at 54 mK. The TLS loss model, given in Eq. (7.58), fits all the data very well. We consistently obtain a loss tangent between $1.4 \times 10^{-3}$ and $1.8 \times 10^{-3}$ in the low voltage saturation regime.

### 7.2.3 Temperature dependence of dielectric loss

We next discuss the temperature dependence of the dielectric loss. The voltage-dependent dielectric loss of resonator LC1 on C1 is measured at different temperatures. The data at each temperature is fitted with Eq. (7.58), which yields the low-power loss tangent $\tan\delta$. The TLS model predicts the following depenence of the loss tangent on temperature $T$:

$$\tan\delta = \tan\delta_0 \times \tanh\left(\frac{\hbar\omega_0}{2k_BT}\right), \tag{7.59}$$

with $\tan\delta_0$ the intrinsic TLS loss tangent. In Fig. 7.12(a), we plot $\tan\delta$ versus temperature, and also a fit of the model in Eq. (7.59). The fit yields $\tan\delta_0 = 1.5 \times 10^{-3}$. In Fig. 7.12(b),

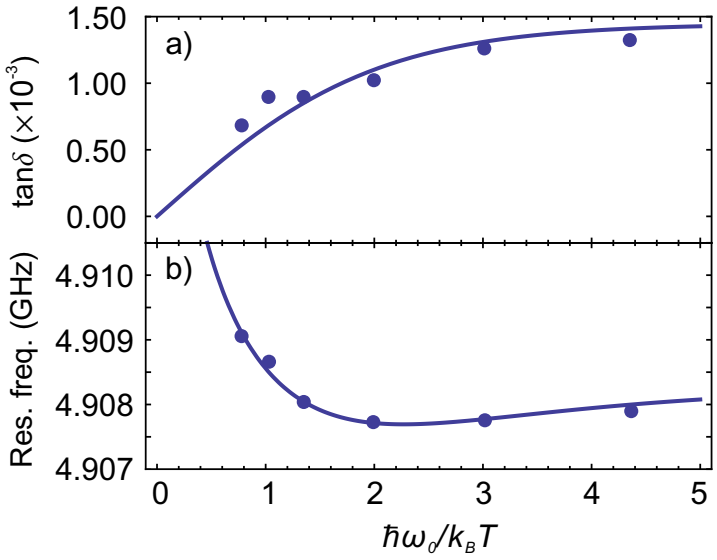



Figure 7.12: **Temperature dependent data of the sub-single photon dielectric loss (a) and the frequency shift (b) of the resonator C1-LC1.** The resonance frequency in (b) is obtained at $V \approx 0.03\,\mu$V. The solid lines are the fits to the TLS model.

we show the resonance frequency at low power versus temperature. We fit this data with a prediction based on TLS theory [106]:

$$f_0(T) = f_{0,i}\left(1 + p\left(\mathrm{Re}\Psi\left(\frac{\hbar\omega_0}{2\pi i k_B T} + \frac{1}{2}\right) - \ln\frac{\hbar\omega_0}{k_B T}\right)\right), \tag{7.60}$$

with $f_{0,i}$ and $p$ as fit parameters. TLS theory gives $\tan\delta_0 = \pi p$, which provides an alternative to determining $\tan\delta_0$; we find a value $\tan\delta_0 = 2\times10^{-3}$ from the fit, in good agreement with the determination based on the variation of low-power loss with temperature.

In the following we discuss the chemical composition of the aluminum oxide films. The films are characterized using X-ray photoelectron spectroscopy (XPS). The plasma oxide has an oxygen-to-aluminum atomic ratio of 1.69. The binding energy (BE) of oxygen $1s$ electron is 531.3 eV. The dependence of the XPS intensity signal on energy for the aluminum $2p$ electrons from the metal and the oxide layer are used to determine the oxide thickness, based on Strohmeier Equation [116]. We determine a thickness of 5.0 nm. For comparison, we measure the O-Al atomic ratio for aluminum oxide films grown by atomic layer deposition (ALD) and exposure to air. We find the ratios 1.52 and 2.08 respectively. The BEs of the oxygen $1s$ electron of the ALD oxide and the native oxide are 531.3 eV and

532.3 eV respectively. With the 5 nm thickness of the plasma oxide and the 16 fF/$\mu$m$^2$ capacitance density obtained from room-temperature measurements of these capacitors, we deduce that the relative permittivity $\epsilon_r = 9.0$. In spite of the small thickness and the high capacitance density, tested plasma oxide capacitors with capacitance ranging from 1.5 pF to 10 pF have a breakdown voltage greater than 10 V at room temperature. The process yield is very high: the specific capacitance of more than 40 capacitors, with areas between 100 and 600 $\mu$m$^2$, fabricated in different runs, had a spread of less than 1%. The 6 resonators measured at low temperatures have resonance frequencies in good agreement with the results of microwave simulations assuming the capacitance as determined at room temperature using a low-frequency measurement.

### 7.2.4 Summary

To summarize, we fabricated aluminum oxide layers using plasma oxidation. This is a high yield process, producing a robust and thin oxide layer. We performed a detailed characterization of the temperature dependence of microwave loss. The results are in good agreement with the tunneling two-level system model. The values of the loss tangent are comparable with values obtained for other types of amorphous aluminum oxide [104, 112]. Our results are relevant for the field of superconducting quantum devices, where aluminum oxide is the tunnel barrier of Josephson junctions used for quantum bits. Plasma oxidation is suitable for compact superconducting resonators where loss is not critical, in applications such as parametric amplifiers.

# Chapter 8

# Decoherence and noise spectroscopy in superconducting flux qubits

A major remaining obstacle to implementing fault-tolerant quantum computation with superconducting qubits is the insufficient coherence time. Due to its macroscopic nature, a superconducting qubit couples strongly to more than one degree of freedom in its environment. Properly isolating a qubit from the environmental noise is the key to achieving a long coherence time. On the other hand, the high noise-sensitivities of superconducting qubits also provide opportunities for investigating the properties and source of noise in superconducting devices. These studies of noise can be useful for future designs of superconducting qubits with longer coherence times.

There are two types of decoherence processes, dephasing and energy relaxation, which are determined by noise in the qubit environment at different frequencies. In the other way round, we can also infer the spectral density of the influential noise by measuring these two processes via dynamical decoupling technique and $T_1$ measurement (see Chapter 4). In addition, we can perform noise spectroscopy by a direct time-domain sampling of fluctuating parameters in the qubit Hamiltonian. This method relies on transferring noise on qubit parameters to qubit state fluctuations and a fast projective readout of the qubit states. In this chapter, we will present extensive studies on the noise spectroscopy of a superconducting flux qubit in circuit QED using a combination of methods.

In the first section of this chapter, we will first present characterization of the coherence of the superconducting flux qubit and the resonator coupled to it. We will then discuss the experimental implementations of the dynamical decoupling technique as well as a noise characterization method based on real-time sampling of the qubit parameter, known as the

Ramsey sampling method. In the second section, we will present the qubit noise spectra in the low-to-intermediate-frequency regime, related to the dephasing of the qubit. The noise spectra, measured by the Ramsey sampling and dynamical decoupling methods, cover a wide frequency range, from $10^{-3}$ to $10^{8}$ Hz. We will also present temperature dependence of the low-to-intermediate-frequency noise and discuss the origin of this noise. In the last section, we will discuss the high-frequency effective noise which is directly related to energy relaxation of the qubit. We will present measurements of the qubit relaxation rate at different operation points and a few temperatures. In the end, we will discuss the possible sources of energy relaxation in this measurement.

## 8.1 Experimental parameters and methods

### 8.1.1 Characterizations of qubit parameters

The qubit which we used to study the noise spectra is a superconducting flux qubit in circuit QED [117, 118, 119, 72, 73]. The device used in the experiments is shown in Figure 8.1(a-c)). The flux qubit is inductively coupled to the transmission line resonator. The first mode of the resonator has a resonant frequency of 6.641 GHz and a quality factor of 28,000 in the single-photon regime. Qubit state control is done using shaped microwave pulses injected into an waveguide terminated by an antenna which is placed near the qubit (see Figure 8.1(b)). Qubit state readout is performed using homodyne measurement on microwaves transmitted through the resonator while the qubit-resonator system is in the dispersive regime [29]. To optimize the readout contrast, the cavity is driven strongly, in the nonlinear regime. A histogram of the homodyne voltage for the qubit readout, averaged over a readout pulse duration of 1.5 $\mu$s, is shown in Figure 8.1(e). The readout contrast for this qubit is 49%, limited mainly by initial state preparation errors due to the thermally-populated excited state.

The qubit Hamiltonian written in the energy eigenbasis at the symmetry point is given by

$$H = \frac{1}{2}(-\Delta\sigma_z + \epsilon\sigma_x) \tag{8.1}$$

with $\epsilon = 2I_{\rm p}(\Phi - \Phi_0/2)$. We write each of the parameters $\lambda = \epsilon, \Delta$ as the sum of its nominal value and a time-dependent fluctuation $\lambda(t) = \lambda^{(0)} + \delta\lambda(t)$. In the energy eigenbasis, the Hamiltonian is written as

$$H = -\frac{\nu}{2}\sigma_z - \frac{1}{2}(\delta\Delta(t)\cos\theta + \delta\epsilon(t)\sin\theta)\sigma_z + \frac{1}{2}(\delta\Delta(t)\sin\theta - \delta\epsilon(t)\cos\theta)\sigma_x \tag{8.2}$$

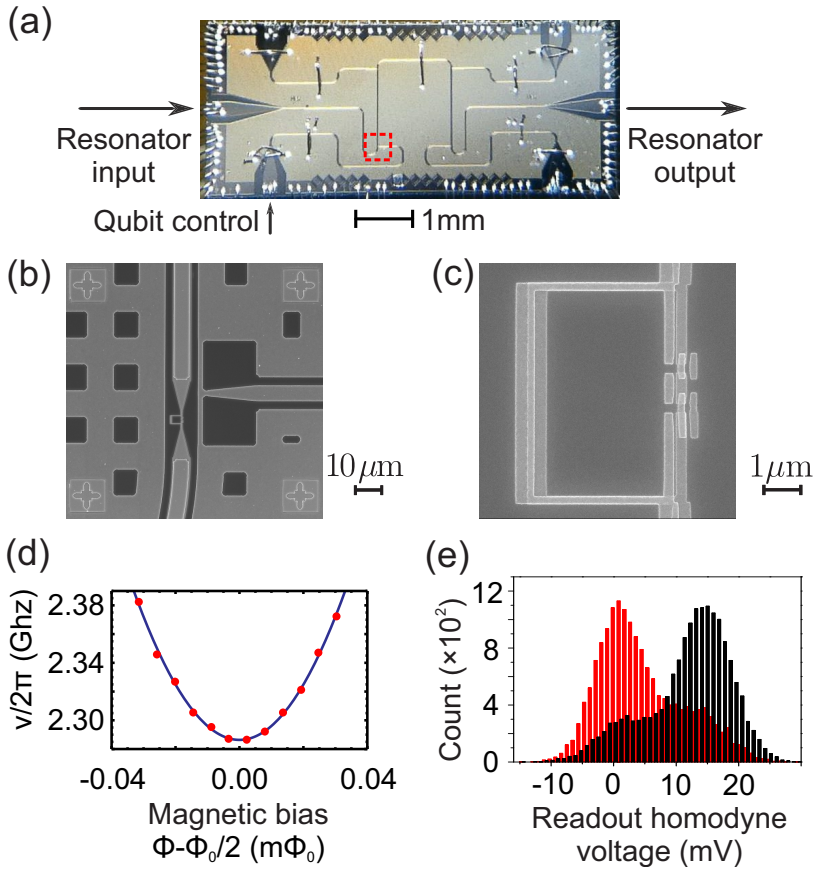



Figure 8.1: **Qubit pictures, spectroscopy, and readout histogram.** (a) Optical image of the device. A transmission line resonator is connected to the input (left) and output (right) port for readout. There are four coplanar waveguides which are present on the chip, but only one is used to couple the qubit to the control pulse (bottom left). The overlaid dashed rectangle indicates the region where the qubit locates. (b) Scanning electron microscope (SEM) image showing a qubit embedded in the resonator. An antenna (right) is used to couple microwave control pulses to the qubit. (c) SEM image of a qubit device nominally identical to that used in this work. (d) Qubit spectroscopy. The transition frequency is plotted versus the applied magnetic flux bias. The continuous line is a fit of the persistent current qubit model, yielding $I_{\mathrm{p}} = 690$ nA and $\Delta = 2.288$ GHz. (e) Readout histograms for the qubit resulting in a readout contrast of 49 %.

with the coupling angle $\theta = \arctan(\epsilon/\Delta)$. We distinguish between the effects of $\delta\epsilon$ and $\delta\Delta$ fluctuations by varying $\theta$ via external magnetic flux, thereby altering the sensitivity of the energy-level splitting $\nu = \sqrt{\Delta^2 + \epsilon^2}$ to fluctuations $D_\lambda = \partial\nu/\partial\lambda = \lambda/\nu$. At the symmetry point of the qubit where $\epsilon = 0$, the dominant contributor to the longitudinal fluctuations in the qubit's energy eigenbasis is the $\Delta$ noise (as the second-order contribution from $\delta\epsilon$ is negligible if $(\delta\epsilon)^2/\Delta \ll \delta\Delta$). While the qubit is biased far away from the symmetry point, where $\epsilon \gg \Delta$, the $\epsilon$ (flux) noise becomes the dominant contributor to the energy-level fluctuation. From the measured qubit spectroscopy versus the external flux $\Phi$ (Figure 8.1(d)), we determined the qubit gap $\Delta = 2.288$ GHz and the persistent current $I_\mathrm{p} = 690$ nA.

The coherence times around the symmetry point of the qubit are characterized at 35 mK. At the symmetry point where the $\epsilon$ noise is suppressed, we measure Ramsey and spin-echo pure dephasing times of 290 and 780 ns respectively and an energy relaxation time $T_1 = 1.84$ $\mu$s (see Figure 8.2(a,b)). The Ramsey and spin-echo decay curves follow an exponential law. We also measure the rate of energy relaxation and the Ramsey and spin-echo pure dephasing rate at various operation points around the symmetry point up to $|\theta| = 0.16$ (see Figure 8.2(c)). We find that all the energy relaxation curves are exponential and the rates have little dependence on the operation point. However, in the Ramsey and spin-echo experiments, we observe non-exponential decays of the coherence function in general. We fit the data to a decay function $\exp\left(-\Gamma_1\tau/2 - (\Gamma_\varphi\tau)^\alpha\right)$, with $\Gamma_1$ the relaxation rate, $\tau$ the free precession time, and $\alpha$ an fitting parameter, to obtain the pure dephasing rate $\Gamma_\varphi$. As we increase the coupling angle $\theta$ by varying the biased magnetic field, the dephasing curve gradually changes from an exponential decay ($\alpha = 1$) to a Gaussian decay ($\alpha = 2$), and the pure dephasing rate $\Gamma_\varphi$ increases shapely. This suggests that the dephasing away from the symmetry point is mainly due to the $\epsilon$ noise. Given that Gaussian decays are observed, we can infer that the $\epsilon$ noise has a non-Markovian noise property.

### 8.1.2 Thermal photons in the resonator and shot noise

In a circuit QED device, the qubit is strongly coupled to a superconducting resonator in the dispersive regime for state readout [27, 28, 29]. The energy eigenstates of the system are the dressed states. The transition frequency of the dressed qubit is given by $\nu + (2n+1)\chi$ where $n$ is the number of photons in the resonator and $\chi = g^2/\delta$ is the dispersive shift (see Section 2.4 and Ref. [27]). Therefore, any fluctuation in the photon number of the resonator will lead to a fluctuation of the qubit transition frequency. This random fluctuation of the photon number, known as the photon shot noise, could become an important source of

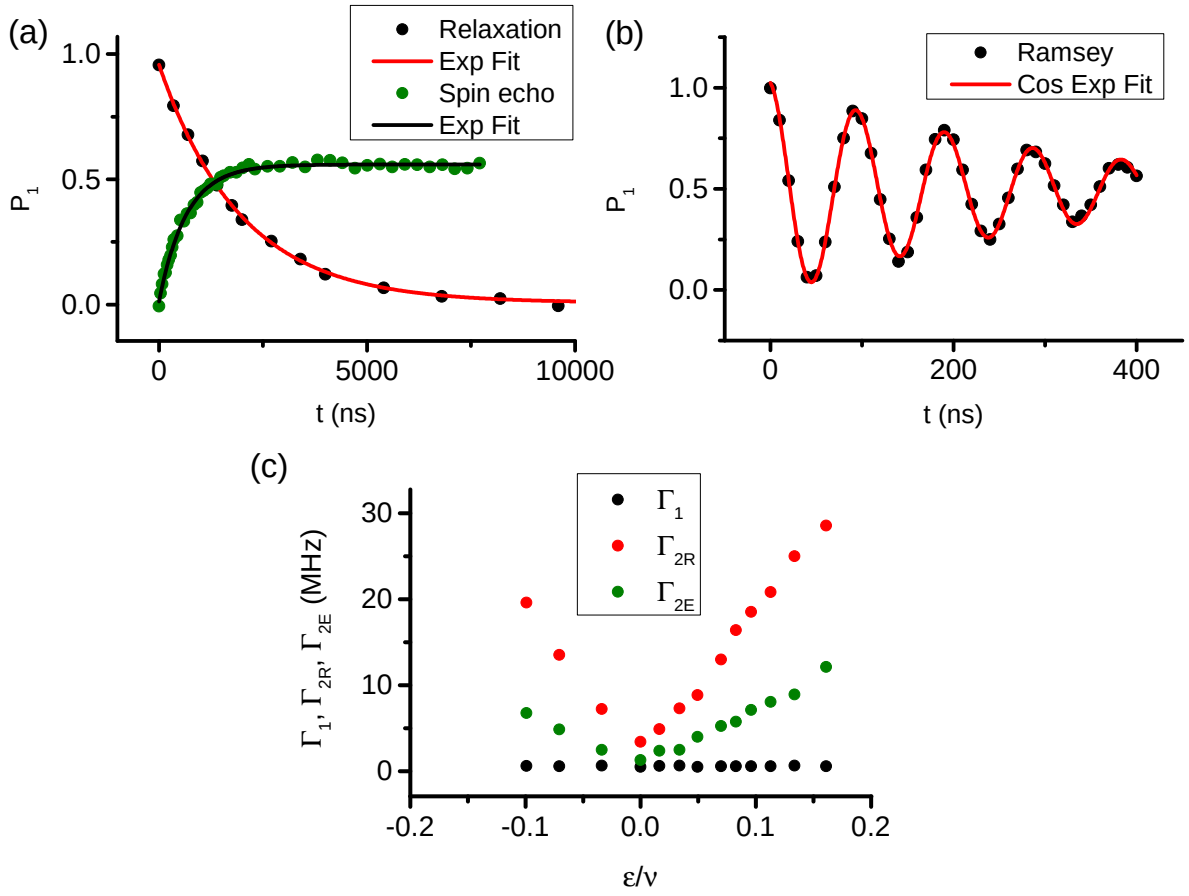



Figure 8.2: **Energy relaxation and dephasing rates around symmetry point.** (a,b) The energy relaxation, spin-echo, and Ramsey decay of the qubit at the symmetry point. The solid lines are fits to exponential decays. The Ramsey experiment is performed with a driving frequency detuned from the qubit frequency by 10 MHz. (c) Energy relaxation and pure dephasing rate of the qubit around the symmetry point. The pure dephasing rate $\Gamma_{2R}$ and $\Gamma_{2E}$ are measured in the Ramsey and spin-echo experiments respectively.

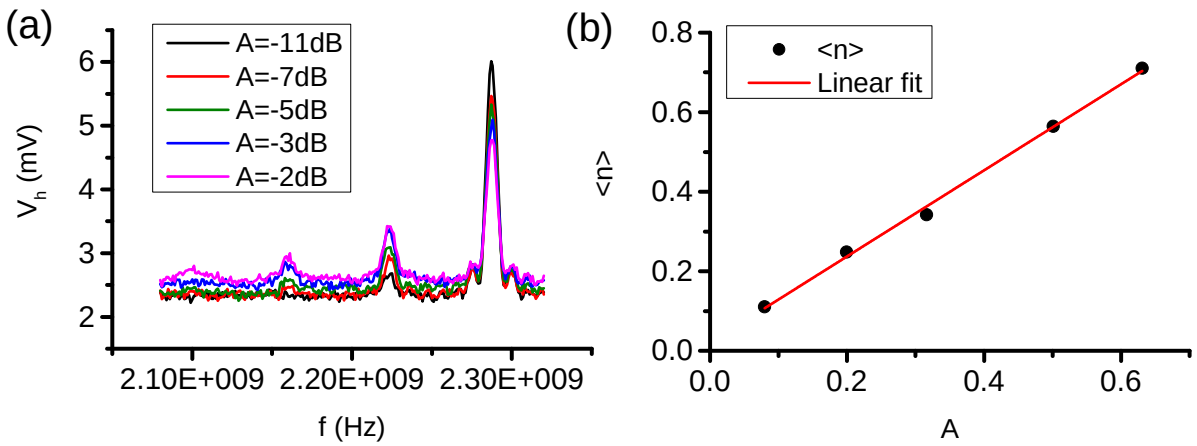



Figure 8.3: **Measurement of thermal photons in the resonator.** (a) Qubit spectroscopy with different average thermal photons injected into the resonator. The average photon number is controlled by adjusting the attenuation factor at the output of the thermal noise source. (b) Average photon numbers obtained from the qubit spectra in (a) versus the attenuation factor. From a linear fit to the data, we determine $\bar{n}_0 = 0.02 \pm 0.01$.

dephasing for a superconducting qubit [120]. Here, we will estimate effects of the photon shot noise on the frequency fluctuation of the qubit.

To understand the influence of photon shot noise on the qubit, we first characterize the qubit's frequency shift $\chi$ by performing a photon number splitting experiment as discussed in Ref. [121]. Here, we generate a thermal state by coupling the output of a wide-band amplifier to the input of the resonator through a tunable attenuator. The photon-number-dependent frequency shift of the qubit is detected by performing spectroscopy measurements on the qubit-resonator system. The measured spectra reveal the quantized nature of the resonator field, containing a separate peak for each photon number state (see Figure 8.3(a)). The frequency difference between two neighboring peaks is the dispersive shift $2\chi = 32.1$ MHz.

The statistics of the thermal photons in the resonator is governed by the rate equations [120]:

$$\frac{dP(N)}{dt} = \Gamma_{N+1\to N}P(N+1) + \Gamma_{N-1\to N}P(N-1) - (\Gamma_{N\to N+1} + \Gamma_{N\to N-1})P(N) \qquad (8.3)$$

where $P(N)$ is the probability of having $N$ photons in the resonator and $\Gamma_{N\to M}$ is the rate of photon jumps from the $N$-photon state to the $M$-photon state. The rates of the photon

jumps are given by

$$\Gamma_{N\to N+1} = \kappa\bar{n}(N+1), \tag{8.4}$$

$$\Gamma_{N\to N-1} = \kappa(\bar{n}+1)N, \tag{8.5}$$

where $\kappa$ is the decay rate of the resonator and $\bar{n}$ is the average photon number. The steady-state probability $P_s(N)$ to Eq. (8.3) is

$$P_s(N) = \frac{1}{1+\bar{n}}\left(\frac{\bar{n}}{1+\bar{n}}\right)^N. \tag{8.6}$$

In a transmission measurement of the resonator, we determine $\omega_\mathrm{r} = 2\pi \times 6.641$ GHz and $\kappa = \omega_\mathrm{r}/Q = 1.49$ MHz in the sub-single-photon regime.

The pulse we use for spectroscopy is a $\pi$-pulse with a pulse width of 109 ns. Since the pulse length is much shorter than the inverse of the photon jumping rate between photon states with small $N$, we can assume that there is no photon jump during the spectroscopy pulse. The photon state peaks in the spectroscopy measurement represent the weight of each Fock state, where the average photon number $\bar{n}$ can be extracted. Assuming the thermal environment around the resonator excites an average of $\bar{n}_0$ photons, the average photon number with extra noise injected from the amplifier is given by

$$\bar{n} = AP_\mathrm{BE}(T)\kappa_\mathrm{in}/\kappa + \bar{n}_0 \tag{8.7}$$

with $P_\mathrm{BE} = 1/(e^{\hbar\omega_\mathrm{r}/kT}-1)$ the Bose-Einstein distribution, $A$ an attenuation factor which is proportional to the value of the tunable attenuator at the output of the amplifier, $\kappa_\mathrm{in}$ the coupling strength to the resonator input, and $\kappa$ the total decay rate of the resonator. In Figure 8.3(b), we show the measured average photon number in the resonator $\bar{n}$ versus the attenuation factor $A$. We determine $\bar{n}_0 = 0.02 \pm 0.01$ by fitting the data to Eq. (8.7).

Since the average photon number of the resonator $\bar{n}_0$ in thermal equilibrium is very close to zero, the photon noise can be approximated by a random telegraph noise fluctuating between the zero photon state and the one photon state. The PSD of the frequency fluctuation of the qubit due to this noise is given by [122]

$$S_\nu(\omega) = 4(1-w_1)w_1(2\chi)^2\frac{\tau}{1+\omega^2\tau^2}, \tag{8.8}$$

where $w_1 \approx \bar{n}_0$ is the probability of finding a photon in the resonator, $2\chi$ is the frequency shift for the one-photon jump, and $\tau^{-1} = \kappa(2\bar{n}+1) \approx \kappa$ is the total transition rate between the two states. In the next section, we will compare the measured noise spectra with an estimation using Eq. (8.8). This will allow us determining the influence of photon shot noise in our device.

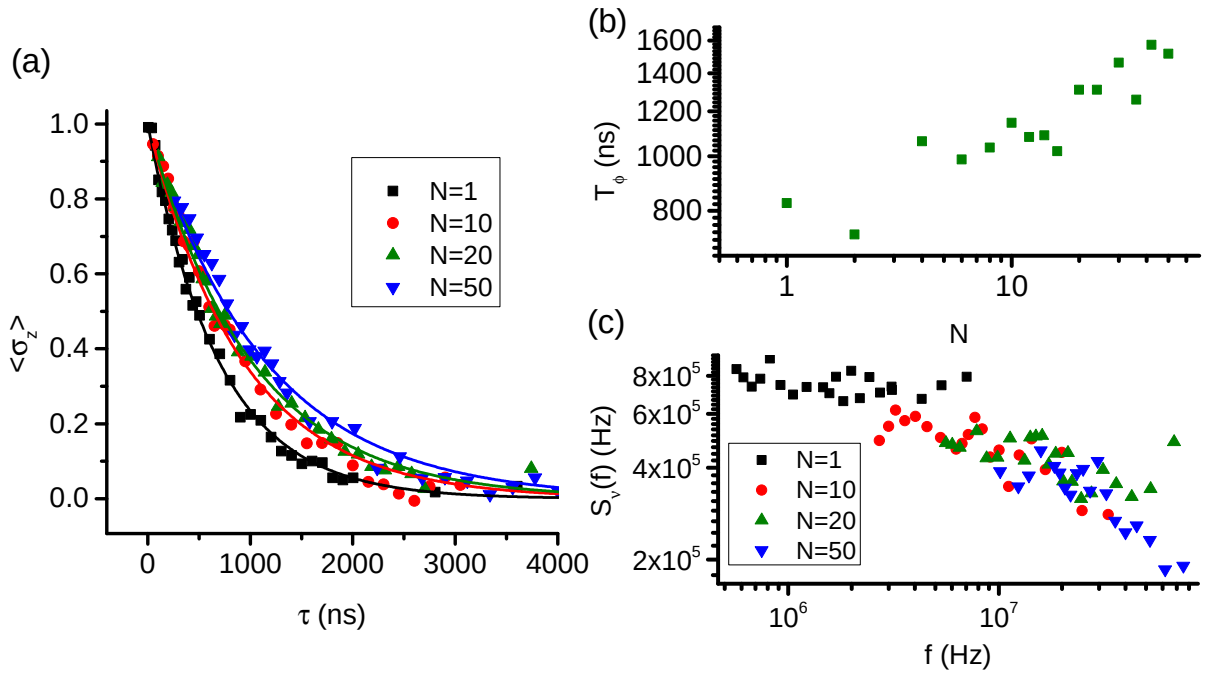



Figure 8.4: **Coherence decay with a CPMG pulse sequence and the calculated noise spectrum.** (a) Measured dephasing process with different number of $\pi$-pulses in the pulse sequence with the qubit biased at the symmetry point. The solid lines are exponential fits to the data. (b) Exacted pure dephasing time from exponential fits in (a) versus the number of $\pi$-pulses. (c) The PSDs of the qubit frequency fluctuation calculated from data in (a).

### 8.1.3 Noise spectroscopy through dynamical decoupling

The noise spectra of the environment can be deduced by measuring dephasing process of the qubit during a dynamical decoupling pulse sequence (see Subsection 4.2.3 for details). Here, we use a Carr-Purcel-Meiboom-Gill (CPMG) pulse protocol [123] which is a modified version of the Carr-Purcel pulse sequence [45] with better tolerance to pulse errors. In Figure 8.4(a), we show an example of coherence decays measured with CPMG pulse sequences with different number of $\pi$-pulse, $N$, at the symmetry point. The decay curves are fitted with an exponential decay function $\exp\left(-\Gamma_1\tau/2 - \Gamma_\varphi\tau\right)$ and the extracted decay time $T_\varphi = 1/\Gamma_\varphi$ is plotted versus $N$ in Figure 8.4(b). We observe an enhancement of the coherence times with an increasing number of $\pi$-pulse.

The power spectral density (PSD) of the longitudinal noise can be calculated from the measured coherence decay $\langle e^{i\varphi_{01}(\tau)}\rangle$ using the filter function method (see Section 4.2.3). By taking energy relaxation and the depolarization during the $\pi$-pulses into account, the PSD can be written into

$$S_z(\omega_0) = \frac{\pi\hbar^2}{\tau^2 \int_0^\infty d\omega F_N(\omega,\tau)} \left( -\ln\langle e^{i\varphi_{01}(\tau)}\rangle - \Gamma_\mathrm{R} N\tau_\pi - \frac{\Gamma_1}{2}(\tau - N\tau_\pi) \right), \tag{8.9}$$

where $F_N(\omega,\tau)$ is the filter function given by Eq. (4.48), $\Gamma_\mathrm{R}$ is the transverse depolarization rate during the $\pi$-pulse, and $\tau_\pi$ is the length of the $\pi$-pulse. We characterize $\Gamma_\mathrm{R} = 0.80$ MHz by measuring the amplitude decay in the Rabi oscillations, and we have $\tau_\pi = 2$ ns in this experiment. In these calculations, for each individual $\tau$ and $N$ in all the decay curves, the integral of the corresponding filter function $F_N(\tau,\omega)$ and its peak position $\omega_0$ are found numerically. In Figure 8.4(c), we show the samples of the noise spectrum calculated from data in Figure 8.4(a).

By varying the total free precession time $\tau$ as well as the number of $\pi$-pulses $N$ in the CPMG pulse sequence, we in principle are able to move the filter function over a wide frequency range thus effectively sample the whole spectrum of the environmental noise. In practice, while the total free precession time is much longer than the dephasing time of the qubit, the coherence function $\langle e^{i\varphi_{01}(\tau)}\rangle$ is close to zero. This makes a determination of the noise amplitude $S(\omega_0)$ at the frequency $\omega_0$, defined by the peak position of the filter function $F_N(\omega,\tau)$, rather unreliable. For the calculation of the PSD, we only include data points with a coherence function $\langle e^{i\varphi_{01}(\tau)}\rangle > 0.1$. This condition corresponds to a free precession time $\tau$ shorter than a timescale of the order of the total dephasing time $T_2$. As a result, with the center frequency of the filter function approximately given by $N/(2\tau)$, the lower frequency limit for noise spectra measured by dynamical decoupling is given by $1/(2T_2)$ limited by $T_2$.

### 8.1.4 Low-frequency noise spectroscopy through Ramsey sampling

In order to explore the noise spectrum in the low-frequency regime, we utilize the Ramsey pulse sequence to encode of low-frequency fluctuations in the qubit transition frequency into measurement results of the qubit state. This method, also explored in Refs. [124, 125, 126], enables measurements of noise spectra down to frequencies limited by the total measurement time and up to frequencies limited by the repetition rate of measurements.

In the regular Ramsey experiment, variations in the precession-frequency lead to a shrinking average polarization, and the influential noise has frequencies spanning from the

inverse of the pulse spacing, $1/\tau$, to the inverse of the total acquisition time $t_{\rm acq}$ (typically a few seconds). However, noise slower than $t_{\rm acq}$ will lead to fluctuations of the qubit frequency at a longer time scale, which will be captured by measuring the average of the qubit state after each of the Ramsey pulse sequences.

Inspired by this mechanism, we use a protocol, based on the Ramsey experiment, to record the time evolution of the qubit frequency. We repeatedly let the qubit undergo free precession by using two $\pi/2$-pulses of the same phase and perform a measurement immediately after the second $\pi/2$-pulse. Instead of varying the pulse separation $\tau$, we fix it at a value $\tau_0$. We also fix the nominal detuning $\delta^{(0)} = \nu^{(0)} - \omega$ between the nominal qubit frequency $\nu^{(0)}$ and the frequency of the applied microwave pulses $\omega$. To maximize the sensitivity of the measurement result to the qubit frequency fluctuations, we choose $\delta^{(0)}/(2\pi) = 1/(4\tau_0)$ so the qubit undergoes a $\pi/2$ rotation around the $X$-$Y$ plane.

In the experiments, this pulse sequence is repeated with a period $t_{\rm rep}$ which is normally 10 to 100 $\mu$s, limited by the energy relaxation time for qubit-state reset. The number of repetitions $N_{\rm rep}$ is normally a large number (typically 16,384), limited by the available memory of the data acquisition module. The total acquisition time for a trace of data is $t_{\rm acq} = t_{\rm rep} N_{\rm rep}$. This data acquisition sequence can be repeated within a time interval of $\Delta t$ where $\Delta t > t_{\rm acq}$ due to overheads for data processing. Given the time evolution of the readout results in each repetition denoted by $r(t)$ ($r(t) = -1$ or 1 representing the ground or excited state in the ideal case) with time $t$ a discrete variable in a step $t_{\rm rep}$, there are two ways to process the data to unveil noise spectra in different frequency regimes.

**Ensemble-averaged scheme**

In the ensemble-averaged scheme, the readings in each trace of the $N_{\rm rep}$ readout results are averaged. The averaged result, denoted as $\bar{r}(t)$, can be understood as the time evolution of the qubit polarization sampled with a time step $\Delta t$. Assuming small fluctuations in the qubit frequency $\nu(t) = \nu^{(0)} + \Delta\nu(t)$, the Ramsey pulse sequence will translate the frequency fluctuation into a fluctuation of the qubit polarization $\langle \sigma_z(t) \rangle = \bar{r}(t)$. The relation between the qubit polarization and the qubit frequency is simply given by the Ramsey interferometry pattern

$$\bar{r} = a(\tau_0) \cos\left((\nu - \omega)\tau_0\right). \tag{8.10}$$

The interference amplitude $a(\tau_0)$ is smaller than the ideal value one due to the presence of dephasing and errors in qubit state readout. We can determine the actual value of $a(\tau_0)$ in the experiments by measuring $\bar{r}$ versus the driving frequency $\omega$ (see Figure 8.5(a)). The

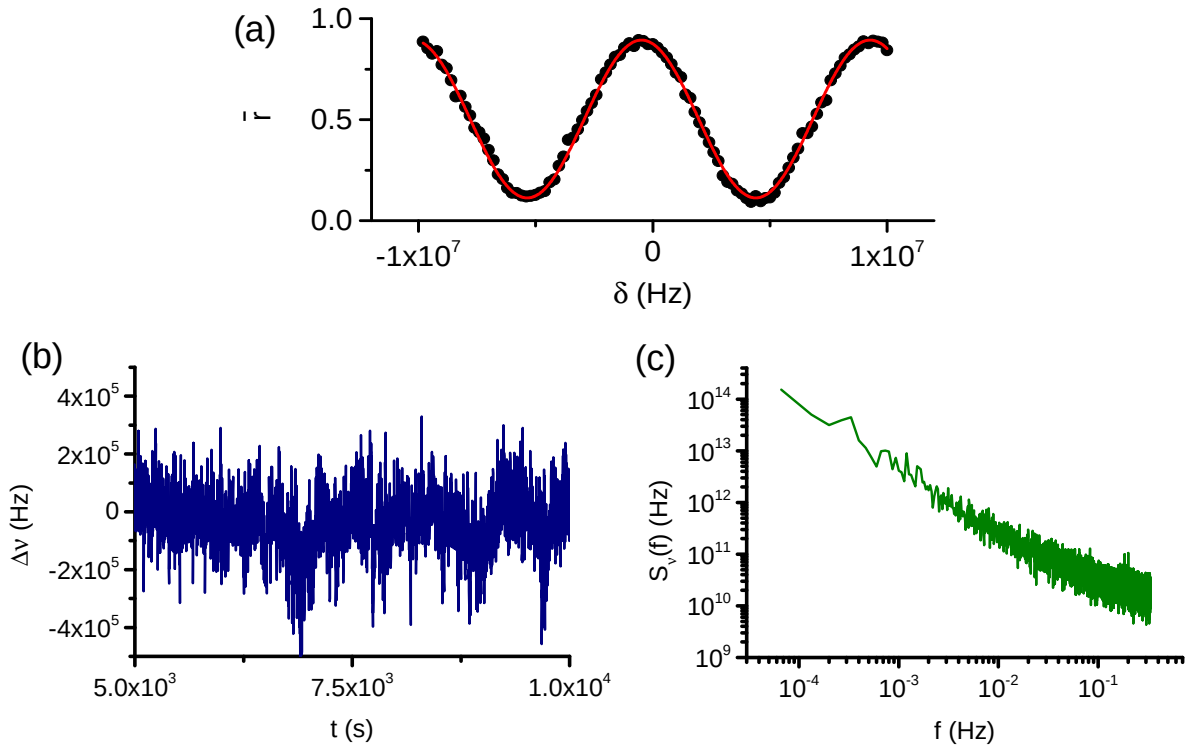



Figure 8.5: **Ensemble-averaged scheme of Ramsey sampling.** (a) Measured dependence of $\bar{r}$ on $\delta^{(0)}$ with $\tau_0 = 100$ ns at the symmetry point. The line is a sinusoidal fit. (b,c) Measured real time frequency fluctuations at the symmetry point and the average PSD.

transfer function between the frequency fluctuation and the fluctuation of $\bar{r}(t)$ is given by an expansion of Eq. (8.10) to the first order:

$$\Delta\bar{r}(t) = -a(\tau_0)\tau_0\Delta\nu(t), \tag{8.11}$$

where we have chosen the nominal detuning $\delta^{(0)} = \pi/(2\tau_0)$ for a maximum sensitivity.

According to the Wiener-Khinchin theorem, the PSD of a fluctuating parameter $\nu(t)$ (here $\nu$ is the frequency of the qubit) is given by the Fourier transform of the autocorrelation function:

$$S_\nu(\omega) = \int_{-\infty}^{\infty} d\tau e^{-i\omega\tau}\langle\nu(t)\nu(t+\tau)\rangle. \tag{8.12}$$

for a long enough acquisition period $T$, the expectation value in the definition above can

be replaced by averaging over $t$. The expression for the PSD becomes

$$S_\nu(\omega) = \lim_{T\to\infty} \int_{-\infty}^{\infty} d\tau e^{-i\omega\tau} \frac{1}{T} \int_{-T/2}^{T/2} dt\, \nu(t)\nu(t+\tau) = \lim_{T\to\infty} \frac{1}{T} |\nu(\omega)|^2, \tag{8.13}$$

where $\nu(\omega)$ is the Fourier transform of $\nu(t)$.

For a discrete set of samples of $\nu(t)$ expressed as $\nu_k$, the PSD is given by

$$S_\nu(\omega_k) = \frac{1}{2\pi T} |\nu_k|^2, \tag{8.14}$$

where $T$ is the total sampling time and the Fourier component $\nu_k$ is given by the Discrete Fourier Transform (DFT):

$$\nu_k = \sum_{n=1}^{N} \nu_n e^{-2\pi i(n-1)k/N}, \tag{8.15}$$

and the discrete frequency $\omega_k$ is defined as $\omega_k = 2\pi k/T$. We then take the statistical average of $L$ traces:

$$\langle S_\nu(\omega_k) \rangle = \frac{1}{L} \sum_{l=1}^{L} S_\nu^{(l)}(\omega_k). \tag{8.16}$$

In Figures 8.5(b), we show the real time frequency fluctuation of the qubit at the symmetry point. The data is obtained from a 10 hour measurement with time interval between neighboring points $\Delta t = 1.5$ s. The entire time-domain data is sliced into 100 traces and the PSD for each individual trace is calculated using Eq. (8.14). The average PSD of the 100 traces are plotted in Figure 8.5(c).

In this ensemble-average scheme, the noise being explored has a frequency span ranging from the inverse of the total sampling time $1/T$ up to the Nyquist frequency $1/(2\Delta t)$.

### Single-shot scheme

In the single-shot scheme, we directly Fourier transform the time evolution of the measurement result $r(t)$ in each trace for the PSD. No time-domain averaging is involved beforehand. The sequence repetition rate $1/t_{\text{rep}}$ is the sampling rate of the time series. The total sampling time in the single-shot scheme is the acquisition time for each trace $t_{\text{acq}} = t_{\text{rep}} N_{\text{rep}}$. The first implementation of this measurement scheme in superconducting qubits was reported in Ref. [126].

Let the series of the measurement result in each repetition $r_n = r(t_n)$, where $t_n$ is the time at which the readout is taken. Each element of the series $\{r_n\}$ is an independent Bernoulli random variable with expectation value given by $\bar{r}_n$. The expectation values $\bar{r}_n$ can be related to the frequency fluctuation of the qubit given by

$$\Delta\bar{r}_n = -a'(\tau_0)\tau_0\Delta\nu_n. \tag{8.17}$$

We note that the equation above is different from Eq. (8.11) for the ensemble-averaged scheme, where we have replaced the Ramsey contrast $a(\tau_0)$ with its ideal value $a'(\tau_0)$ without dephasing. This difference is due to the fact that each value of $\bar{r}_n$ in the single-shot scheme is an independent realization of the frequency fluctuation, while each value of $\bar{r}_n$ in the ensemble scheme is the average of a large number of realizations of noise. In other words, there is no shrinking of the qubit polarization as for each individual measurement result in the single-shot scheme.

The influential noise in the single-shot scheme can be understood as follows: The PSD of $\{r_n\}$, $S_r(\omega_k)$, is equivalent to that of $\{\bar{r}_n\}$, $S_{\bar{r}}(\omega_k)$, except for an additional white noise level resulting form the statistical noise generated by the qubit state readout. We thus can assume $S_r(\omega_k) = S_{\bar{r}}(\omega_k) + S_s$ (see Appendix F). $S_{\bar{r}}(\omega_k)$ is the PSD of the noise of interest which is directly related to the frequency fluctuation of the qubit, and $S_s$ is the PSD of the additional white noise. $S_r(\omega_k)$ can be computed from Eq. (8.14). In order to obtain $S_{\bar{r}}(\omega_k)$, we next eliminate the white noise using the cross-PSD technique. A detail proof of the principle can be found in Ref. [126], while we shall only give the procedure of this technique here.

The cross-PSD technique for the white noise elimination is described by the following steps:

1. Split $\{r_n\}$ into two interleaved time series, $\{r'_n = r_{2n-1}\}$ and $\{r''_n = r_{2n}\}$.

2. Calculate the cross-correlated PSD of $\{r'_n\}$ and $\{r''_n\}$ using

$$S_{r'r''}(\omega_k) = \frac{1}{2\pi T} r'_k r''_k e^{i\omega_k \Delta t}, \tag{8.18}$$

   where the series $r'_k$ and $r''_k$ are the DFTs of $r'_n$ and $r''_n$ respectively and $\omega_k = 2\pi k/T$ are the frequencies of the Fourier components. The term $T$ is the total sampling time. In this case, the total sampling time is given by $T = t_{\text{rep}} N_{\text{rep}}$ and the time interval between neighboring points is given by $\Delta t = t_{\text{rep}}$. The term $e^{i\omega_k \Delta t}$ is added to account for the additional phase introduced by a real-time delay between two interleaved series.

3. The cross-PSD obtained from a single trace $S^{(l)}_{r'r''}(\omega_k)$ is subject to substantial errors and is generally a complex number. The average over multiple traces should be performed on the complex values of the cross-PSDs, namely

$$\langle S_{r'r''}(\omega_k)\rangle = \frac{1}{L}\sum_{l=1}^{L} S^{(l)}_{r'r''}(\omega_k). \tag{8.19}$$

Upon averaging the cross-PSD over a large number of traces $L$, the white-noise part of the PSD can be completely removed while noise with longer correlation time is left. In our case, as long as $\bar{r}_n$ is not a white noise, we have $\langle S_{r'r''}(\omega_k)\rangle \approx S_{\bar{r}_n}(\omega_k)$.

In the end, based on the linear relation between the expectation value of the measurement result $\bar{r}_n$ and the qubit frequency (Eq. (8.17)), we have the PSD of the frequency fluctuation given by

$$S_\nu(\omega_k) = S_{\bar{r}}(\omega_k)/(a'(\tau_0)\tau_0)^2. \tag{8.20}$$

In Figures 8.6, we show the PSD and cross-PSD of frequency fluctuations of the qubit at the symmetry point. The experiment is performed with $t_{\rm rep} = 100$ $\mu$s and $N_{\rm rep} = 16,384$. These PSDs are averaged over $20,000$ traces.

With the single-shot scheme, we are able to reveal a noise spectrum with a frequency up to $1/(4t_{\rm rep})$.

## 8.2 Low-to-intermediate-frequency noise spectroscopy

In this section, we will present low-to-intermediate-frequency-noise spectroscopy of the parameter fluctuations in a flux qubit using the dynamical decoupling as well as the Ramsey sampling methods. With a combination of these two methods together, we are able to probe the PSD of the noise over a wide frequency range, from $10^{-3}$ to $10^8$ Hz, with some relatively minor gaps.

### 8.2.1 Noise spectroscopy at 35 mK

We first study noise spectroscopy of the qubit parameters at 35 mK. In general, frequency fluctuations of a flux qubit have contributions from both the fluctuation of $\Delta$ and $\epsilon$. Their sensitivities, given by $\Delta/\nu$ and $\epsilon/\nu$ can be tuned via changing the nominal biased magnetic flux in the qubit loop. The $\Delta$ noise can be measured by probing transition frequency

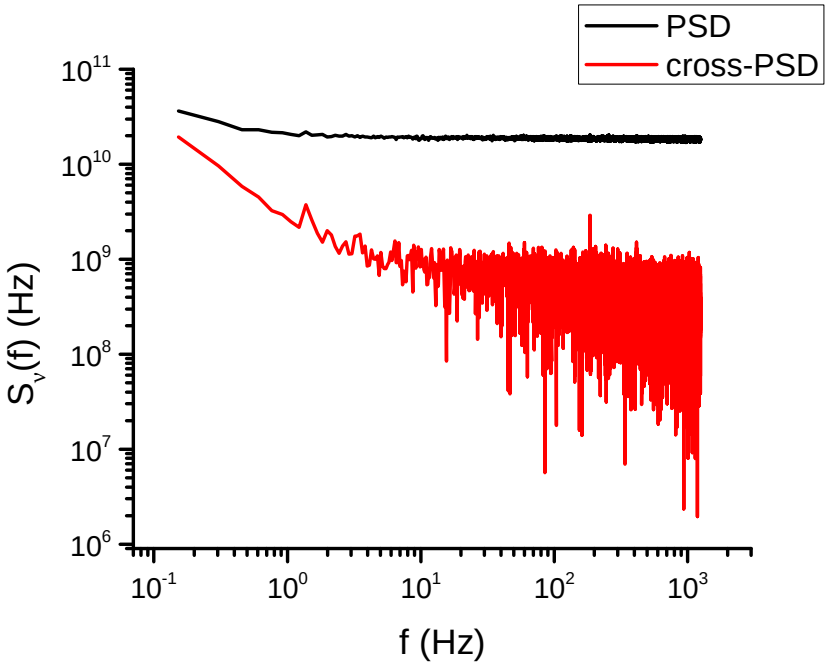



Figure 8.6: **Single-shot scheme of Ramsey sampling.** Measurements are performed at the symmetry point of the qubit with a Ramsey free precession time $\tau_0 = 100$ ns. The PSD and cross-PSD of the series of the single-shot readout results are the black and red lines respectively.

fluctuations of the qubit at the symmetry point where $\epsilon = 0$, and the $\epsilon$ noise can be measured in the same way by moving the qubit far away from the symmetry point, where $\epsilon \gg \Delta$.

In practice, we find that the Ramsey and spin-echo dephasing rates increase dramatically with increasing values of $\epsilon/\nu$ (see Figure 8.2(c)). At an operation point, where $\epsilon/\nu = 0.25$, the dephasing rate is about one order of magnitude larger than at the symmetry point, which suggests that the $\epsilon$ noise is the dominant contributor to the qubit transition frequency fluctuation. Thus, the PSD of the $\epsilon$ noise $S_\epsilon(\omega)$ can be calculated from the PSD of the qubit frequency fluctuation $S_\nu(\omega)$ using $S_\epsilon(\omega) = (\nu/\epsilon)^2 S_\nu(\omega)$.

In Figure 8.7, we present detailed measurements of the PSD of the $\Delta$ and $\epsilon$ noise of the flux qubit. The PSDs between $10^{-3}$ and $10^{-1}$ Hz are obtained using the ensemble-average scheme Ramsey sampling, which has a sampling rate in the order of 1 Hz. The PSDs

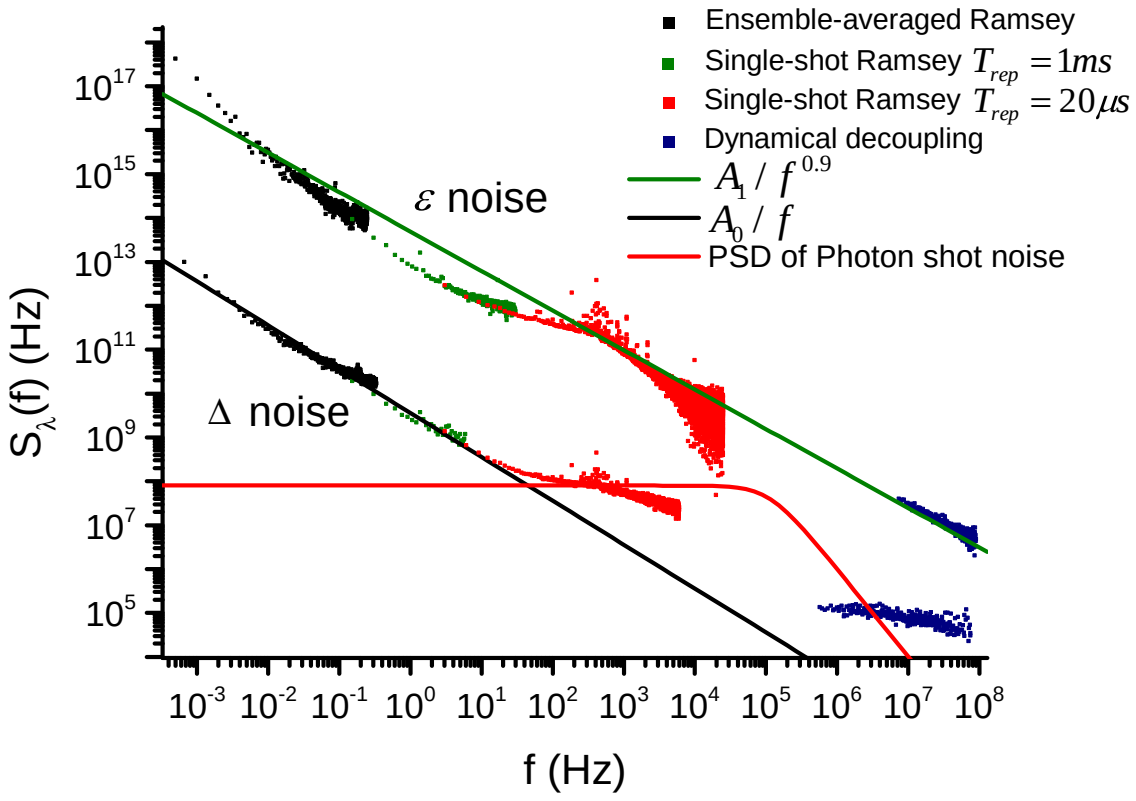



Figure 8.7: **A summary of the $\Delta$ and $\epsilon$ noise at 35 mK.** The $\Delta$ noise (dots on the lower branch) is measured at the symmetry point and the $\epsilon$ noise (dots on the higher branch) is measured where $\epsilon/\nu = 0.25$. To explore the PSD with a wide frequency range, we performed Ramsey sampling experiments with the ensemble-averaged scheme (black dots) and the single-shot scheme with repetition times of 1 ms (green dots) and 20 $\mu$s (red dots). We also perform dynamical decoupling experiments to probe the noise PSD with frequencies in the MHz range (blue dots). The black and green lines are $S(f) = A_1/f^{0.9}$ and $S(f) = A_0/f$ respectively. The red line is the calculated PSD due to the photon shot noise with a Lorentzian shape.

between $10^{-1}$ and $10^4$ Hz are given by the cross-PSD from the single-shot scheme Ramsey sampling with two different repetition times, 1 ms and 20 $\mu$s, with the later one limited by the reset time of the qubit and the resonator. The spectra with frequencies higher than 1 MHz are obtained using the dynamical decoupling method.

We find that the $\Delta$ noise has an spectrum which is consistent with $1/f$ noise at frequencies between $10^{-3}$ and 10 Hz. This noise might originate from slow variations of the background charge [127, 128] or critical current fluctuations [129, 130, 131]. If we parameterize the low-frequency $\Delta$ noise as an effective, normalized critical-current noise with $I_c = 1.3$ $\mu$A in a Josephson junction with area $A = 0.062$ $\mu$m$^2$, we obtain a magnitude of the critical-current noise $(26pA)^2$/Hz at 1 Hz. The PSD in the relatively weak frequency dependent regime, between 10 and $10^4$ Hz, qualitatively agrees with the plateau of the Lorentzian spectrum of the photon shot noise (calculated by Eq. (8.8)). The PSD of the $\Delta$ noise in the MHz frequency regime is almost flat but on a much lower level than the Lorentzian plateau. However, we note that, in the noise processing procedure for the dynamical decoupling experiments, we assume Gaussian noise (see Section 4.2.3), where the photon shot noise might not be taken into account properly.

The $\epsilon$ noise is about three orders of magnitude larger than the $\Delta$ noise at almost all frequencies. At frequencies between $10^{-3}$ and 10 Hz, the $\epsilon$ noise has a $1/f^\alpha$ spectrum with $\alpha \approx 1.2$. At the frequency regime where 1 MHz$< f <$ 100 MHz, the PSD follows the $1/f^\alpha$ law with $\alpha \approx 0.9$. There is a "bump-like" feature on the $1/f^\alpha$ spectrum of the $\epsilon$ noise around $f = 300$ Hz and the cause of this feature is unclear.

### 8.2.2 Temperature dependence of the $\epsilon$ flux noise

We next present measurements on temperature dependence of the $\epsilon$ flux over the temperature range $35 - 130$ mK. The $\epsilon$ noise is measured at the operation point where $\epsilon/\nu = 0.25$ for all the temperatures.

Due to thermal excitation at higher temperatures, the initial qubit state is an incoherent mixture state with a higher excited state population. This initial state preparation error results in reduced Ramsey contrasts $a(\tau_0)$ and $a'(\tau_0)$ for the ensemble-averaged and the single-shot scheme respectively. The reduced Ramsey contrasts lead to increasing difficulties to resolve the noise of interest $S_{\bar{\tau}}(f)$ from the white noise floor given by the statistical-sampling noise $S_s$. In principle, the white noise could be eliminated by the cross-PSD method but this would require a very large number of traces to average the data while the Ramsey contrasts are poor. To eliminate the white noise floor more efficiently, we interleave the Ramsey pulse sequence with another pulse sequence containing

only a $\pi/2$-pulse followed by a readout. We collect all the readout results in both pulse sequences. The PSD calculated from the readout of the $\pi/2$-pulse sequence is a measurement of the statistical-sampling noise $S_s$ (see Appendix F). Therefore, we obtain the PSD of the frequency fluctuation by subtracting the noise floor measured with the $\pi/2$-pulse sequence from the noise measured by the Ramsey pulse sequence. We note that there is another important advantage of our noise substraction method over the cross-PSD method which is designed for white-noise elimination. Our noise substraction method works for any types of noise on the qubit frequency, while the cross-PSD method is not applicable if the noise of interest is dominated by white noise.

After subtracting the white noise floor, the spectra of the frequency fluctuation can still be very noisy. In order to emphasize the trend of the spectra, we smooth the PSDs by performing moving averages, where we take window size of $6 \times 10^{-3}$ and 30 Hz for the ensemble-scheme and the single-shot scheme respectively. In Figure 8.8, we show the $\epsilon$ noise measured at different temperatures. Using the Ramsey sampling and the dynamical decoupling methods, we cover the frequency ranges of $10^{-3}$ to $10^{3}$ Hz and $10^{7}$ to $10^{8}$ Hz. We find that the $\epsilon$ noise has no temperature dependence over the temperature range of $35 - 130$ mK in the above frequency range.

The $\epsilon$ noise can arise from flux noise or critical current noise. Experiments [129, 131, 132] have shown that the critical-current noise has an $1/f$ spectrum and a magnitude proportional to $T^2$. Since we do not observe temperature dependence on the $\epsilon$ noise, we can infer that the flux noise is the dominant contributor and it has no temperature dependence over the temperature range of our measurements. We then convert the PSD of the $\epsilon$ noise to the PSD of the flux noise using $S_\Phi(f) = S_\epsilon(f)/(2I_\mathrm{p}/h)^2$. We obtain a magnitude of the flux noise $(4.5 \times 10^{-7}\Phi_0)^2/\mathrm{Hz}$ at 1 Hz. We note that the flux noise we measured here is consistent with the other measurements using superconducting qubits [133, 134, 126] and SQUIDs [135, 136]. The magnitude of the flux noise we measured at 1 Hz is at the lower end of what has been reported before.

## 8.3 Qubit energy relaxation: a probe of high-frequency effective noise

The energy relaxation process can be thought of as a consequence of noise transversely coupled to the qubit. In Section 4.1.1, we shown that the rate of energy relaxation is proportional to the noise PSD at the qubit frequency. In this section, we will present experiments on the the energy relaxation of the flux qubit at different operation points

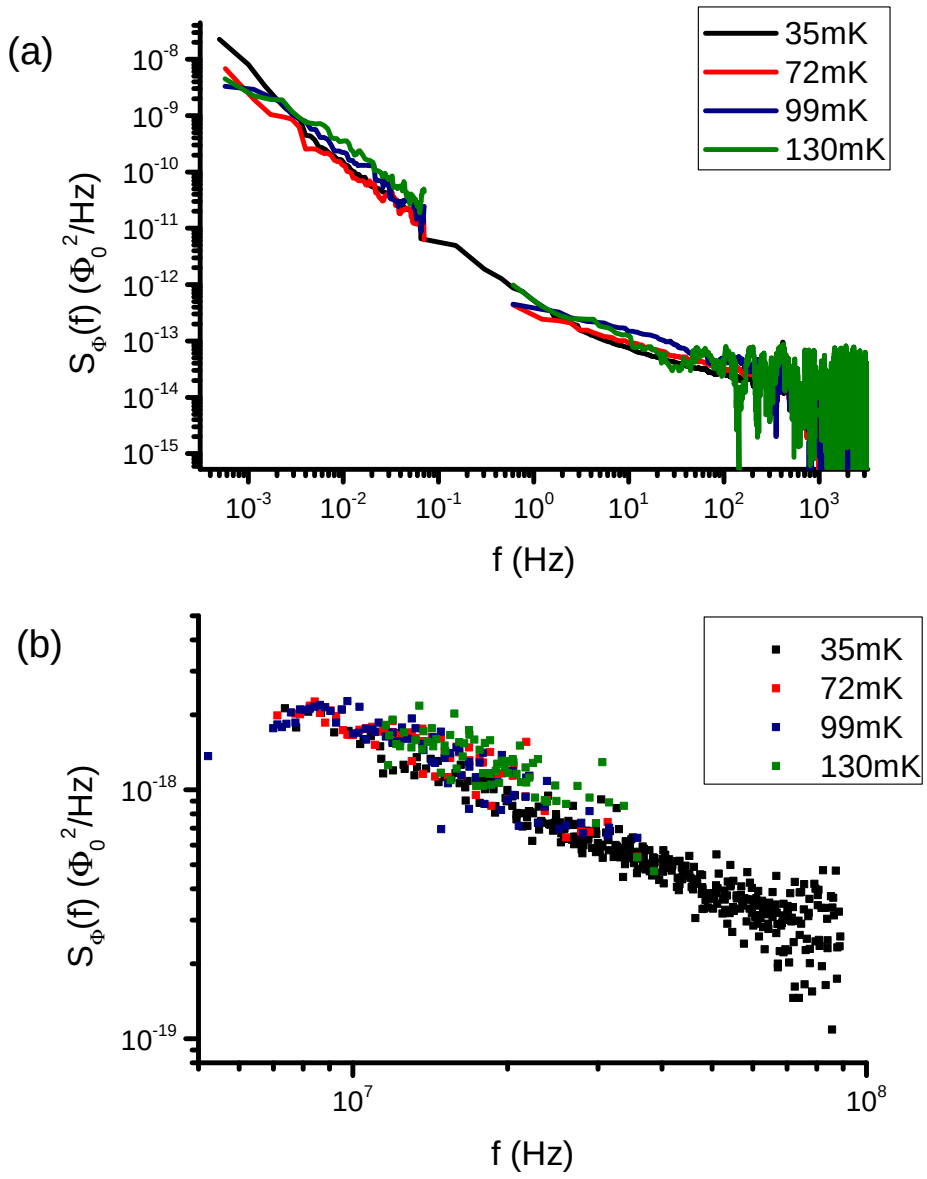



Figure 8.8: **Temperature dependence of the $\epsilon$ flux noise.** (a) PSDs of the $\epsilon$ flux noise measured with the Ramsey sampling method at various temperatures. The spectra have been smoothed by performing moving averages with window size of $6 \times 10^{-3}$ and 30 Hz for the ensemble-scheme and the single-shot scheme respectively. (b) PSDs of the $\epsilon$ flux noise measured by the dynamical decoupling method at various temperatures.

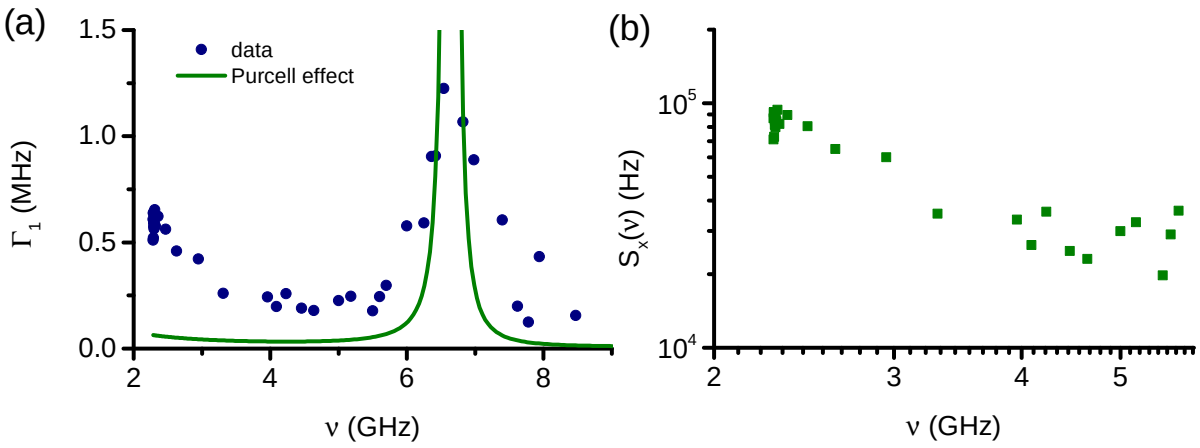



Figure 8.9: **Energy relaxation, Purcell effect, and effective high-frequency noise.** (a) Energy relaxation rates of the qubit measured at different operation points. The solid line is the calculated energy relaxation rates due to the resonator according to the Purcell model. (b) PSD of the effective transversal noise $S_x(\nu)$ calculated from the energy relaxation rate. The influence of the Purcell effect has been subtracted from the measured relaxation rate.

and various temperatures as measurements of the effective high-frequency noise.

### 8.3.1 Energy relaxation at different operation points

At 35 mK, we measure energy relaxation rates of the qubit versus its operation point by changing the biased magnetic field in the qubit loop. In Figure 8.9(a), we show the energy relaxation rate $\Gamma_1$ versus the frequency of the qubit $\nu$ over a broad range, together with a plot of the calculated rate induced by the Purcell effect [137].

The calculations of the Purcell relaxation rate take into account relaxation due to the first 3 modes of the resonator, where the rate for each mode is given by $\Gamma_k = \kappa_k g_k'^2/(k\omega_r - \nu)^2$ with $\kappa_k = k^2\kappa$ the decay rate [137] and $g_k' = g_k\Delta/\nu$ the effective coupling to the $k$-th mode of the resonator. From the distance $\chi = 32.1$ MHz between neighboring photon peaks in the qubit spectroscopy, we determine $g_1 = 537$ MHz by numerically calculating the dispersive shift of the qubit by multiple modes of the resonator. The coupling $g_k$ to the other modes using in the calculations can be related to $g_1$ using Eq. (2.41).

We find that the relaxation rate of the qubit sharply increase in the vicinity of the cavity frequency at 6.641 GHz, where the qubit is the most likely to relax due to photon

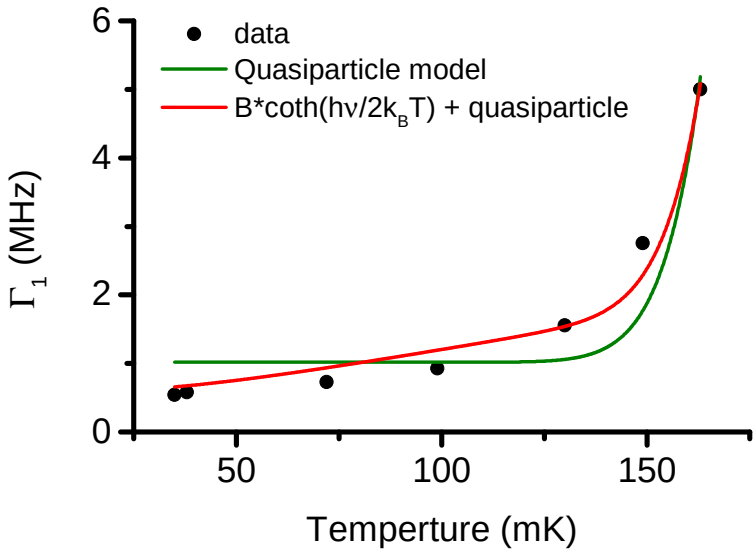



Figure 8.10: **Temperature dependence of the energy relaxation measured at the symmetry point.** The green line is a fit to the quasiparticle loss model. The red line is a fit to the model which takes both the quasiparticle tunneling and the Johnson-Nyquist noise into account. In these models, we assume the superconducting gap of aluminum $\Delta_s = 60$ GHz.

loss in the resonator. Outside this regime, the energy relaxation rates of this qubit are not limited by the Purcell effect.

In Figure 8.9(b), we show the PSD of the effective transversal noise coupled to the qubit versus the qubit frequency. The calculated Purcell relaxation rate has been subtracted from the data. This effective noise could originate from quasi-particle tunneling.

### 8.3.2 Temperature dependence of the energy relaxation

We also measure the temperature dependence of the energy relaxation rate over 35 − 160 mK. In Figure 8.10, we show the energy relaxation rate of the qubit measured at different temperatures at the symmetry point.

The measured rate is then compared with a theoretical prediction which considers energy relaxation due to quasiparticle tunneling. As discussed in Ref. [138, 139, 140, 141, 142],

the relaxation rate of a superconducting qubit is proportional to the quasiparticle density $x_{\rm qp}$ in the superconductor. In thermal equilibrium, the quasiparticle density generated by thermal fluctuations is given by $x_{\rm th}(T) = \sqrt{2\pi k_B T/\Delta_s} e^{-\Delta_s/k_B T}$, with $\Delta_s$ the superconducting gap and $T$ the temperature. In addition, nonequilibrium quasiparticles can also be generated by various sources such as high-frequency stray radiation, which has a temperature independent contribution to the energy relaxation rate. Therefore, the relaxation rate can be expressed as

$$\Gamma_1(T) = \Gamma_{1,0} + A x_{\rm th}(T), \tag{8.21}$$

where $\Gamma_{1,0}$ represents losses due to the nonequilibrium quasiparticles as well as other temperature independent mechanisms. The experimental data is fitted by Eq. (8.21) (see Figure 8.10). Although the sharp increase on the relaxation rate at temperatures $T > 130$ mK is consistent with loss due to thermal excited quasiparticles which is active at the temperature $T \gtrsim \Delta_s/k_B$, the agreement between this model and the data is imperfect.

To account for the temperature dependence of the relaxation rate at low temperatures, we consider another relaxation rate model given by $\Gamma_1(T) = \Gamma_{1,0} + A x_{\rm th}(T) + B \coth(\hbar\nu/(2k_B T))$, where we added an additional term $B \coth(\hbar\nu/(2k_B T))$ into the quasiparticle loss model. This additional term has the form of the relaxation rate due to the Johnson-Nyquist noise. A better fitting curve to the data yields $B = 0.6$ MHz (see Figure 8.10). However, a calculation of the Johnson-Nyquist flux noise generated by the qubit control line gives a relaxation rate of 0.018 MHz at 35 mK, which is one order of magnitude smaller than the measured rate. This suggests that the Johnson-Nyquist noise coupled through the qubit control line is not a limiting factor for the energy relaxation. The genuine source of the qubit energy relaxation at low temperatures is still not clear.

## 8.4 Summary

We have presented experimental studies of decoherence and noise spectroscopy in a superconducting flux qubit. By using the Ramsey sampling and dynamical decoupling methods, we study the $\Delta$ and flux noise of the qubit, which is responsible for dephasing. At 35 mK, we perform detailed measurements on the power spectral density of both noise over a wide range of frequencies, from $10^{-3}$ to $10^{8}$ Hz. In addition, we also measure temperature dependence of the flux noise. We find that the measured flux noise has a spectrum which is consistent with $1/f^{\alpha}$ noise and no temperature dependence over $35 - 130$ mK. The properties of the flux noise we measured is consistent with measurements done by the other groups using either qubits or SQUIDs.

We also measure the energy relaxation of the qubit at various bias points and its temperature dependence at the symmetry point. The measured rates are compared with calculated relaxation rates due to the Purcell effect. We determine that the Purcell effect is not a limiting factor of relaxation when the qubit is detuned from the resonator. The measured temperature dependence of relaxation rates is consistent with quasiparticle tunneling loss at temperatures at $T > 100$ mK.

Here, we have presented extensive characterization of decoherence in a flux qubit. On some other similar devices, longer energy relaxation and dephasing times are found [72]. The causes of this variation in coherence times between devices are still under investigation. Nevertheless, the decoherence and noise characterization tools which we present here are ready to be applied to more devices. Extending these decoherence studies to multiple devices with varying parameters is expected to provide key information about the decoherence mechanisms in superconducting flux qubits.

# APPENDICES

# Appendix A

# Fabrication of qubit devices

The device is fabricated on a high-resistivity silicon substrate, in two steps. Firstly, the resonator and the control lines are defined by optical lithography, followed by evaporation of a 190 nm thick aluminum layer and liftoff. In the second step, a bilayer resist is patterned by electron-beam lithography. After an argon milling step, shadow evaporation of two aluminum layers, 40 and 65 nm thick respectively, followed by liftoff, defines the qubit.

# Appendix B

# Pulse calibration for quantum state tomography

The quantum state tomography experiments are performed by applying pre-rotation pulses to the qubit before the readout. We use pre-rotation pulses denoted by unitary operations including identity $I$ and $\pi/2$ rotations around the $x$- and $y$-axis, denoted by $R_x(\pi/2)$ and $R_y(\pi/2)$ respectively. The pre-rotation pulses $R_x(\pi/2)$ and $R_y(\pi/2)$ are defined with $t_\mathrm{r} = t_\mathrm{f} = 0.2$ ns and $A_\mathrm{m} = 2\pi \times 130$ MHz, where the dynamics are well described by the RWA. The length and the phase of these pulses are chosen so that their rotation angles, as well as the angle between their rotation axes, are calibrated to $\pi/2$. To calibrate the rotation angles and the rotation axes of these pulses, we manipulate the qubit with a pulse sequence consisting of the pre-rotation pulses and then measure the final state of the qubit. For calibrating the rotation angle $\theta$ of pulse $R_{x(y)}(\theta)$, we use a pulse sequence corresponding to a unitary operation $\left[R_{x(y)}\left(\theta\right)\right]^{2n+1}$ which amplifies the rotation angle error by $2n+1$ times and projects this angle error to the measurement basis. Using the above pulse sequence with $n = 5$, we determine an optimized pulse length of $t_\mathrm{p} = 1.9$ ns and an upper bound of 0.003 rad on the error of the rotation angles around both axes. For calibrating the rotation axes, we use a pulse sequence corresponding to unitary operation $R_{y'}\left(\frac{\pi}{2}\right)\left\{\left[R_x\left(\frac{\pi}{2}\right)\right]^2\left[R_{y'}\left(\frac{\pi}{2}\right)\right]^2\right\}^n R_x\left(\frac{\pi}{2}\right)$, where $R_{y'}\left(\frac{\pi}{2}\right)$ denotes the rotation around the axis $y'$ to be calibrated. Using pulse sequence with $n = 5$ which amplifies the error in the rotation axis by $2n$ times, we determine an upper bound of 0.002 rad on the error of the rotation axis $y'$. These rotation-angle and rotation-axis errors lead to an error less than 0.003 for each Bloch vector component $\sigma_i$. These errors are much smaller than the statistical errors from the measurements which will be discussed in the next section.

# Appendix C

# Quantum state preparation with strong pulse

The density matrices of states are reconstructed from the quantum state tomography data using maximum likelihood estimation. A direct comparison between the reconstructed state $\rho$ from experimental results and the ideal state $\rho_{\text{ideal}}$ is given by the state fidelity $F = \text{Tr}\left(\sqrt{\sqrt{\rho}_{\text{ideal}}\rho\sqrt{\rho}_{\text{ideal}}}\right)$. Statistical errors of the reconstructed states and their fidelities are determined by the parametric bootstrapping method [143]. The procedure is described as follows: 1. Calculations of the standard deviation $\sigma$ of the Bloch vector $\vec{\sigma} = (\sigma_x, \sigma_y, \sigma_z)$ obtained from the tomography experiments using the measurement statistics. According to the central limit theorem, the average of the random variables $\bar{\sigma}_i = \sum_n \sigma_{i,n}/n$ $(i = x, y, z)$ has a normal distribution with a mean of $\langle\sigma_i\rangle$ and a standard deviation of $\sigma(\sigma_i)/\sqrt{n}$ with $n$ the number of repeated experiments. 2. Generation of random data of the Bloch vector from the normal distributions above. The size $B$ of the random data need to be large, usually $B > 100$. 3. For each random data, the maximum likelihood estimation is used to estimate the quantum state $\rho$ and the state fidelity $F$ with respect to the target state is calculated. Finally, statistics for all the data of size $B$ is collected. The variance of data serves as an estimator of the standard error.

Using pulses with $A_{\text{m}} = 2\pi \times 0.46$ GHz and rise and fall times about 20 ps, we prepare states targeting $|-Y\rangle = (|0\rangle - i|1\rangle)/\sqrt{2}$ and $|1\rangle$ from the ground state $|0\rangle$ with a total pulse length of 0.48 ns and 1.08 ns respectively. The reconstructed density matrices of the

actual states are determined to be:

$$\rho_{|-Y\rangle} = \begin{pmatrix} 0.511048 & -0.0145217 + 0.499667i \\ -0.0145217 - 0.499667i & 0.488952 \end{pmatrix},$$
$$\rho_{|1\rangle} = \begin{pmatrix} 0.00590452 & -0.0709229 + 0.0289758i \\ -0.0709229 - 0.0289758i & 0.994095 \end{pmatrix},$$

of which the fidelities are $0.9996 \pm 0.0006$ and $0.9969 \pm 0.0008$ respectively.

# Appendix D

# Choice of quasienergies and quasienergy states

Although the eigenvalue problem in Eq. (3.26) has an infinite number of solutions, there are only two inequivalent solutions and all the other solutions are copies obtained by shifting an integer number of quanta $n\omega$ between the quasienergy and the periodic part of the Floquet states. We take the two eigenvalues of which difference corresponds to the Rabi frequency $\Omega_{\mathrm{R}} = |\Delta - \omega|$ in the $A \to 0$ limit as the two inequivalent solutions. The consideration of evolution in the Floquet picture requires the decomposition of qubit states into quasienergy states at $A = 0$ and $t = 0$. While any two orthogonal states are a proper choice of Floquet states at $A = 0$, we chose $|u_{0,1}\rangle = (|0\rangle \pm |1\rangle)/\sqrt{2}$. This choice corresponds to assuming a finite value of $A$ and then taking the limit $A \to 0$.

# Appendix E

# Notations and approximations used the Closest Pole and Zero Method

This appendix contains the notation definitions and details of approximations of $S_{21}$ and $V/V_{\text{in}}^{+}$ in Subsec. 7.1.1 and 7.1.2.

We first consider the response functions, $S_{21}$ and $V/V_{\text{in}}^{+}$ (Eq. (7.56) and (7.2)), of the circuit model shown in Fig. 7.1 b) and replace the circuit parameters in these expressions with the reduced parameters using Eq. (7.6). After performing parameter replacements and expression simplifications in *Mathematica* [36], we obtain the following polynomial factional forms for $S_{21}$ and $v = V/V_{\text{in}}^{+}$:

$$S_{21} = \frac{a_0 + a_1 qx + a_2 (qx)^2}{b_0 + b_1 qx + b_2 (qx)^2 + b_3 (qx)^3 + b_4 (qx)^4}, \tag{E.1}$$

$$v = \frac{c_0 + c_1 qx + c_2 (qx)^2}{d_0 + d_1 qx + d_2 (qx)^2 + d_3 (qx)^3 + + d_4 (qx)^4}. \tag{E.2}$$

Their coefficients are defined as

$$a_0 = +\,32(-iq + \gamma - \alpha\gamma)\xi \tag{E.3}$$

$$a_1 = +\,32(1 + \gamma - \alpha\gamma)\xi \tag{E.4}$$

$$a_2 = +\,8(1 + \gamma - \alpha\gamma)\xi \tag{E.5}$$

$$c_0 = +\,32\xi(\gamma - \alpha\gamma + i\alpha\xi) \tag{E.6}$$

$$c_1 = +\,16\xi(-2(-1 + \alpha)\gamma + i\alpha\xi) \tag{E.7}$$

$$c_2 = -\,8(-1 + \alpha)\gamma\xi \tag{E.8}$$

and

$$b_0 = d_0 = -16i\left(iq\gamma + \left(i(2+(-2+\alpha)\alpha)\gamma + q\left(2+\alpha^2\gamma-\beta\gamma\right)\right)\xi + \left(i\beta(q+i\gamma)+\alpha^2(1-iq+\gamma)\right)\xi^2\right) \tag{E.9}$$

$$b_1 = d_1 = +8\left(2i\gamma + 4\xi + 2(2+2(-1+\alpha)\alpha-\beta)\gamma\xi - i\left(3\alpha^2(1+\gamma)-\beta(2+3\gamma)\right)\xi^2\right) \tag{E.10}$$

$$b_2 = d_2 = +4\left(3i\gamma + \left(2+\left(2-2\alpha+6\alpha^2-5\beta\right)\gamma\right)\xi - 3i\left(\alpha^2-\beta\right)(1+\gamma)\xi^2\right) \tag{E.11}$$

$$b_3 = d_3 = +2i\gamma + 8\left(\alpha^2-\beta\right)\gamma\xi - 2i\left(\alpha^2-\beta\right)(1+\gamma)\xi^2 \tag{E.12}$$

$$b_4 = d_4 = +\left(\alpha^2-\beta\right)\gamma\xi. \tag{E.13}$$

We then extract the coefficients of the zeroth and first order $qx$ terms from the corresponding numerator and denominator of each response function, which allows us to rewrite the approximate response function in the linear factional form. We obtain:

$$\tilde{S}_{21} = \eta \times \frac{a+jx}{b+jx}, \tag{E.14}$$

$$\text{and } \tilde{v} = \zeta \times \frac{a'+jx}{b'+jx}, \tag{E.15}$$

where

$$a = \frac{q - j(-1+\alpha)\gamma}{q(1+\gamma-\alpha\gamma)}, \tag{E.16}$$

$$a' = \frac{2j(-1+\alpha)\gamma + 2\alpha\xi}{2q(-1+\alpha)\gamma - jq\alpha\xi}, \tag{E.17}$$

and

$$b = b' = \frac{-2q\gamma + 2\left(-(2+(-2+\alpha)\alpha)\gamma + jq\left(2+\alpha^2\gamma-\beta\gamma\right)\right)\xi + 2\left(-\beta(q+j\gamma)+\alpha^2(q+j(1+\gamma))\right)\xi^2}{q\left(-2\gamma + 2j(2+(2+2(-1+\alpha)\alpha-\beta)\gamma)\xi + \left(3\alpha^2(1+\gamma)-\beta(2+3\gamma)\right)\xi^2\right)}, \tag{E.18}$$

$$\zeta = \frac{-4i(-1+\alpha)\gamma\xi - 2\alpha\xi^2}{-2\gamma + 2i(2+(2+2(-1+\alpha)\alpha-\beta)\gamma)\xi + \left(3\alpha^2(1+\gamma)-\beta(2+3\gamma)\right)\xi^2}. \tag{E.19}$$

We rewrite the linear factional $\tilde{S}_{21}$ and $\tilde{v}$ by separating $q$ from the other reduced parameters, which gives:

$$\tilde{S}_{21} = \eta\frac{A + j\frac{B}{q} + jx}{C + \frac{D}{q} + j(E+\frac{F}{q}) + jx}, \tag{E.20}$$

and

$$\tilde{v} = \zeta \frac{\frac{K}{q} + j\frac{J}{q} + jx}{C + \frac{D}{q} + j(E + \frac{F}{q}) + jx}. \tag{E.21}$$

By Taylor expanding the coefficients $A$, $C$, and $E$ in terms of small parameters $\alpha$ and $\gamma$, we find that $A \approx 1$, $C \approx 1$, and $E \approx 0$. We identify the resonance frequency as the minimum value of $|\tilde{S}_{21}|$. By taking the first order derivative of $|\tilde{S}_{21}|$ with $A = 1$, $C = 1$, and $E = 0$, we find the extrema:

$$x_0' = \frac{-B^2 + D^2 + F^2 + 2Dq \pm \sqrt{(D^2 + (B-F)^2)((B-F)^2 + (D+2q)^2)}}{2(B-F)q}. \tag{E.22}$$

Only the extremum with "$-$" sign corresponds to the minimum position. As a result, the true resonance frequency of the circuit is

$$\omega_0 = \omega_0' \left(1 + \frac{-B^2 + D^2 + F^2 + 2Dq - \sqrt{(D^2 + (B-F)^2)((B-F)^2 + (D+2q)^2)}}{2(B-F)}\right). \tag{E.23}$$

We take the resonance frequency as the resonance frequency without internal loss ($q = 0$) as $\omega_0 = \omega_0'(1 - B/2)$. Therefore, the response functions $\tilde{S}_{21}$ and $\tilde{v}$ can be rewrite in reduced forms in terms of the resonance frequency $\omega_0$ and internal quality factor $Q_i = \frac{1}{q_i} = \omega_0 R C_0 = \frac{1-B/2}{q}$ as

$$\tilde{S}_{21,\mathrm{red}} = \eta \frac{1 + 2j\frac{\omega-\omega_0}{\omega_0 q_i}}{1 + \frac{D}{q_i(1-B/2)} + j\frac{F-B}{q_i(1-B/2)} + 2j\frac{\omega-\omega_0}{\omega_0 q_i}} \tag{E.24}$$

and

$$\tilde{v}_{\mathrm{red}} = \zeta \frac{\frac{K}{q_i(1-B/2)} + \frac{j(J-B)}{q_i(1-B/2)} + 2j\frac{\omega-\omega_0}{\omega_0 q_i}}{1 + \frac{D}{q_i(1-B/2)} + j\frac{F-B}{q_i(1-B/2)} + 2j\frac{\omega-\omega_0}{\omega_0 q_i}}. \tag{E.25}$$

In the end, we calculate the quantity of the reduced response function $\tilde{v}_{\mathrm{red}}$ for $\omega = \omega_0$. We obtain:

$$\tilde{v}_0 = \zeta \frac{\frac{K}{q_i(1-B/2)} + \frac{j(J-B)}{q_i(1-B/2)}}{1 + \frac{D}{q_i(1-B/2)} + \frac{j(F-B)}{q_i(1-B/2)}}. \tag{E.26}$$

The quantity of $\tilde{v}_0$ depends on the values of the parameters which appear in the expression of $\tilde{S}_{21,\mathrm{red}}$ and a linear scaling factor $\lambda$. We define $\lambda$ as

$$\lambda = \zeta \frac{K + j(J-B)}{1 - B/2}. \tag{E.27}$$

The full expression of $\lambda$ in terms of the reduced parameters is given below:

$$\lambda = \frac{4j\xi(2\alpha\xi - (-1+\alpha)\gamma(-2j+\alpha\xi))}{(-2+(-1+\alpha)\gamma)\left(-2\gamma+2j(2+(2+2(-1+\alpha)\alpha-\beta)\gamma)\xi+(3\alpha^2(1+\gamma)-\beta(2+3\gamma))\,\xi^2\right)}. \tag{E.28}$$

The calculations involving replacing parameters, simplifying expressions, extracting coefficients from polynomials, and expanding expressions into Taylor series in this appendix are performed in *Mathematica* [36].

# Appendix F

# Statistical-sampling noise in the Ramsey sampling measurements

We assume the measurement results in the Ramsey pulse sequence is given by $r_n$. The expected value of each measurement result, which reflects the actual qubit frequency fluctuations, is given by $\bar{r}_n$. Following the treatment given by Fei Yan [144], we first investigate the autocorrelation function $C_r(m) = \langle r_n r_{n+m} \rangle$ and $C_{\bar{r}}(m) = \langle \bar{r}_n \bar{r}_{n+m} \rangle$ for the series $\{r_n\}$ and $\{\bar{r}_n\}$ respectively. For $m$-th autocorrelation term with $m \neq 0$, we have

$$C_r(m) = C_{\bar{r}}(m). \tag{F.1}$$

This is because the results of statistical-sampling in different trials are independent and taking the expectation value averages out their randomness. For $m = 0$, the autocorrelation functions become $C_r(0) = \langle r^2 \rangle$ and $C_{\bar{r}}(0) = \langle \bar{r}^2 \rangle$ and their difference is give by $\delta C(0) = \langle r^2 \rangle - \langle \bar{r}^2 \rangle$. Since $\langle r \rangle = \langle \bar{r} \rangle$, we have

$$\delta C(0) = \sigma_r^2 - \sigma_{\bar{r}}^2 \tag{F.2}$$

where $\sigma_\lambda^2 = \langle \lambda^2 \rangle - \langle \lambda \rangle^2$ is the variance.

The power spectral density (PSD) is the Fourier transform of the autocorrelation function. The difference in the PSD of $\{r_n\}$ and $\{\bar{r}_n\}$ is given by

$$S_s = S_r(f_k) - S_{\bar{r}}(f_k) = \sum_m \delta C(m) e^{-i2\pi f_k m} \Delta t = \delta C(0) \Delta t = (\sigma_r^2 - \sigma_{\bar{r}}^2) \Delta t. \tag{F.3}$$

Therefore, the added noise $S_s$ is a frequency independent white noise.

We note that the above result is applicable to both the single-shot and the ensemble-average scheme of the Ramsey sampling. In the single-shot scheme, the statistical-sampling noise is a Bernoulli process with $\sigma_r^2 \approx 4P_1^{(0)}(1-P_1^{(0)}) \gg \sigma_{\bar{r}}^2$, where $P_1^{(0)}$ is the nomial probability of measuring the excited state. In the ensemble-average scheme, since each measurement result $r_{n,\mathrm{ems}} = \bar{\sigma}_z$ is an average of a large number of results, the statistical-sampling noise is a Gaussian process, whose variance is much narrower than $\sigma_{\bar{r}}^2$. Therefore the variance of the measurement $\sigma_{r,\mathrm{ems}}^2 \approx \sigma_{\bar{r}}^2$.

If the contrast of the Ramsey interferometry is low, where $\sigma_r \gg \sigma_{\bar{r}}$, the PSD of the added noise is given by $S_s \approx \sigma_r^2 \Delta t$. We find that this added noise purely consists of the statistical sampling noise and noise induced by imperfect measurements. We can measure this noise by preparing the qubit into a state which has the same $z$-polarization as the average polarization after the Ramsey pulse, and calculating the PSD of the measurement results. In experiments, since the Ramsey pulse and the qubit bias are normally setup to have $\langle \sigma_z \rangle = 0$ for a maximum sensitivity, the added noise can be measured from a pulse sequence consisting of a $\pi/2$-pulse immediately followed by readout.

# References


[1] Richard P. Feynman. Simulating physics with computers. *International Journal of Theoretical Physics*, 21(6-7):467–488, 1982.

[2] Seth Lloyd. Universal quantum simulators. *Science*, 273(5278):1073–1078, 1996.

[3] Peter W. Shor. Polynomial-time algorithms for prime factorization and discrete logarithms on a quantum computer. *SIAM J. Comput.*, 26(5):1484–1509, October 1997.

[4] Lov K. Grover. A fast quantum mechanical algorithm for database search. In *Proceedings of the Twenty-eighth Annual ACM Symposium on Theory of Computing*, STOC '96, pages 212–219, New York, NY, USA, 1996. ACM.

[5] David P. DiVincenzo. The physical implementation of quantum computation. *arXiv preprint quant-ph/0002077*, 2000.

[6] T. D. Ladd, F. Jelezko, R. Laflamme, Y. Nakamura, C. Monroe, and J. L. OBrien. Quantum computers. *Nature*, 464(7285):45–53, 2010.

[7] J. Bardeen, L. N. Cooper, and J. R. Schrieffer. Microscopic theory of superconductivity. *Phys. Rev.*, 106:162–164, Apr 1957.

[8] J. Bardeen, L. N. Cooper, and J. R. Schrieffer. Theory of superconductivity. *Phys. Rev.*, 108:1175–1204, Dec 1957.

[9] Caspar H. van der Wal, A. C. J. ter Haar, F. K. Wilhelm, R. N. Schouten, C. J. P. M. Harmans, T. P. Orlando, Seth Lloyd, and J. E. Mooij. Quantum superposition of macroscopic persistent-current states. *Science*, 290(5492):773–777, 2000.

[10] Y. Nakamura, Yu. A. Pashkin, and J. S. Tsai. Coherent control of macroscopic quantum states in a single-cooper-pair box. *Nature*, 398(6730):786–788, 1999.

[11] William D. Oliver, Yang Yu, Janice C. Lee, Karl K. Berggren, Leonid S. Levitov, and Terry P. Orlando. Mach-zehnder interferometry in a strongly driven superconducting qubit. *Science*, 310(5754):1653–1657, 2005.

[12] P. Forn-Diaz, J. Lisenfeld, D. Marcos, J. J. Garcia-Ripoll, E. Solano, C. J. P. M. Harmans, and J. E. Mooij. Observation of the bloch-siegert shift in a qubit-oscillator system in the ultrastrong coupling regime. *Phys. Rev. Lett.*, 105:237001, Nov 2010.

[13] T. Niemczyk, F. Deppe, H. Huebl, E. P. Menzel, F. Hocke, M. J. Schwarz, J. J. Garcia-Ripoll, D. Zueco, T. Hummer, E. Solano, A. Marx, and R. Gross. Circuit quantum electrodynamics in the ultrastrong-coupling regime. *Nature Physics*, 6(10):772–776, October 2010.

[14] J. Q. You and Franco Nori. Atomic physics and quantum optics using superconducting circuits. *Nature*, 474(7353):589–597, June 2011.

[15] M. H. Devoret and R. J. Schoelkopf. Superconducting circuits for quantum information: An outlook. *Science*, 339(6124):1169–1174, 2013.

[16] Michael A. Nielsen and Isaac L. Chuang. *Quantum Computation and Quantum Information: 10th Anniversary Edition*. Cambridge University Press, 10 anv edition, 1 2011.

[17] B. D. Josephson. Possible new effects in superconductive tunnelling. *Physics Letters*, 1(7):251 – 253, 1962.

[18] P. A. M. Dirac. The fundamental equations of quantum mechanics. *Proceedings of the Royal Society of London A: Mathematical, Physical and Engineering Sciences*, 109(752):642–653, 1925.

[19] Yang Yu, Siyuan Han, Xi Chu, Shih-I Chu, and Zhen Wang. Coherent temporal oscillations of macroscopic quantum states in a josephson junction. *Science*, 296(5569):889–892, 2002.

[20] V Bouchiat, D Vion, P Joyez, D Esteve, and M H Devoret. Quantum coherence with a single cooper pair. *Physica Scripta*, 1998(T76):165, 1998.

[21] Jens Koch, Terri M. Yu, Jay Gambetta, A. A. Houck, D. I. Schuster, J. Majer, Alexandre Blais, M. H. Devoret, S. M. Girvin, and R. J. Schoelkopf. Charge-insensitive qubit design derived from the cooper pair box. *Phys. Rev. A*, 76:042319, Oct 2007.

[22] J. E. Mooij, T. P. Orlando, L. Levitov, Lin Tian, Caspar H. van der Wal, and Seth Lloyd. Josephson persistent-current qubit. *Science*, 285(5430):1036–1039, 1999.

[23] T. P. Orlando, J. E. Mooij, Lin Tian, Caspar H. van der Wal, L. S. Levitov, Seth Lloyd, and J. J. Mazo. Superconducting persistent-current qubit. *Phys. Rev. B*, 60:15398–15413, Dec 1999.

[24] David M. Pozar. *Microwave Engineering*. Wiley, 4 edition, 11 2011.

[25] C. J. Hood, T. W. Lynn, A. C. Doherty, A. S. Parkins, and H. J. Kimble. The atom-cavity microscope: Single atoms bound in orbit by single photons. *Science*, 287(5457):1447–1453, 2000.

[26] J. M. Raimond, M. Brune, and S. Haroche. Manipulating quantum entanglement with atoms and photons in a cavity. *Rev. Mod. Phys.*, 73:565–582, Aug 2001.

[27] Alexandre Blais, Jay Gambetta, A. Wallraff, D. I. Schuster, S. M. Girvin, M. H. Devoret, and R. J. Schoelkopf. Quantum-information processing with circuit quantum electrodynamics. *Phys. Rev. A*, 75:032329, Mar 2007.

[28] A. Wallraff, D. I. Schuster, A. Blais, L. Frunzio, R.-S. Huang, J. Majer, S. Kumar, S. M. Girvin, and R. J. Schoelkopf. Strong coupling of a single photon to a superconducting qubit using circuit quantum electrodynamics. *Nature*, 431(7005):162–167, September 2004.

[29] A. Wallraff, D. I. Schuster, A. Blais, L. Frunzio, J. Majer, M. H. Devoret, S. M. Girvin, and R. J. Schoelkopf. Approaching unit visibility for control of a superconducting qubit with dispersive readout. *Phys. Rev. Lett.*, 95:060501, Aug 2005.

[30] J. Majer, J. M. Chow, J. M. Gambetta, Jens Koch, B. R. Johnson, J. A. Schreier, L. Frunzio, D. I. Schuster, A. A. Houck, Andreas Wallraff, Blais A., Devoret M. H., Girvin S. M., and Schoelkopf R. J. Coupling superconducting qubits via a cavity bus. *Nature*, 449(7161):443–447, 2007.

[31] E. T. Jaynes and F. W. Cummings. Comparison of quantum and semiclassical radiation theories with application to the beam maser. *Proceedings of the IEEE*, 51(1):89–109, Jan 1963.

[32] Florian R. Ong, Jean-Luc Orgiazzi, Arlette de Waard, Giorgio Frossati, and Adrian Lupascu. Insertable system for fast turnaround time microwave experiments in a dilution refrigerator. *Review of Scientific Instruments*, 83(9):–, 2012.

[33] F. Bloch. Nuclear induction. *Phys. Rev.*, 70:460–474, Oct 1946.

[34] J. R. Johansson, P. D. Nation, and Franco Nori. Qutip 2: A python framework for the dynamics of open quantum systems. *Computer Physics Communications*, 184(4):1234 – 1240, 2013.

[35] Jon H. Shirley. Solution of the Schrödinger equation with a hamiltonian periodic in time. *Phys. Rev.*, 138:B979–B987, May 1965.

[36] Wolfram Research, Inc. *Mathematica*. Wolfram Research Inc., 2012.

[37] Howard Carmichael. *An Open Systems Approach to Quantum Optics: Lectures Presented at the Universit Libre de Bruxelles, October 28 to November 4, 1991 (Lecture Notes in Physics Monographs)*. Springer, 1993 edition, 12 2013.

[38] Ryogo Kubo, Morikazu Toda, and Natsuki Hashitsume. *Statistical Physics II: Nonequilibrium Statistical Mechanics (Springer Series in Solid-State Sciences, 31)*. Springer-Verlag, 2 edition, 11 1995.

[39] Lorenza Viola, Emanuel Knill, and Seth Lloyd. Dynamical decoupling of open quantum systems. *Phys. Rev. Lett.*, 82:2417–2421, Mar 1999.

[40] Crispin Gardiner and Peter Zoller. *Quantum noise: a handbook of Markovian and non-Markovian quantum stochastic methods with applications to quantum optics*, volume 56. Springer Science & Business Media, 2004.

[41] G. Ithier, E. Collin, P. Joyez, P. J. Meeson, D. Vion, D. Esteve, F. Chiarello, A. Shnirman, Y. Makhlin, J. Schriefl, and G. Schön. Decoherence in a superconducting quantum bit circuit. *Phys. Rev. B*, 72:134519, Oct 2005.

[42] Lorenza Viola and Seth Lloyd. Dynamical suppression of decoherence in two-state quantum systems. *Phys. Rev. A*, 58:2733–2744, Oct 1998.

[43] D. Vitali and P. Tombesi. Using parity kicks for decoherence control. *Phys. Rev. A*, 59:4178–4186, Jun 1999.

[44] Michael J. Biercuk, Hermann Uys, Aaron P. VanDevender, Nobuyasu Shiga, Wayne M. Itano, and John J. Bollinger. Optimized dynamical decoupling in a model quantum memory. *Nature*, 458(7241):996–1000, 2009.

[45] H. Y. Carr and E. M. Purcell. Effects of diffusion on free precession in nuclear magnetic resonance experiments. *Phys. Rev.*, 94:630–638, May 1954.

[46] E. L. Hahn. Spin echoes. *Phys. Rev.*, 80:580–594, Nov 1950.

[47] Gtz S Uhrig. Exact results on dynamical decoupling by $\pi$ pulses in quantum information processes. *New Journal of Physics*, 10(8):083024, 2008.

[48] Łukasz Cywiński, Roman M. Lutchyn, Cody P. Nave, and S. Das Sarma. How to enhance dephasing time in superconducting qubits. *Phys. Rev. B*, 77:174509, May 2008.

[49] Jonas Bylander, Simon Gustavsson, Fei Yan, Fumiki Yoshihara, Khalil Harrabi, George Fitch, David G. Cory, Yasunobu Nakamura, Jaw-Shen Tsai, and William D. Oliver. Noise spectroscopy through dynamical decoupling with a superconducting flux qubit. *Nature Physics*, 7(7):565–570, 2011.

[50] H. Wang, M. Hofheinz, M. Ansmann, R. C. Bialczak, Erik Lucero, M. Neeley, A. D. O'Connell, D. Sank, M. Weides, J. Wenner, A. N. Cleland, and John M. Martinis. Decoherence dynamics of complex photon states in a superconducting circuit. *Phys. Rev. Lett.*, 103:200404, Nov 2009.

[51] D.F. Walls and Gerard J. Milburn. *Quantum Optics*. Springer, 2nd edition, 1 2008.

[52] L. M. K. Vandersypen and I. L. Chuang. NMR techniques for quantum control and computation. *Rev. Mod. Phys.*, 76:1037–1069, Jan 2005.

[53] F. Bloch and A. Siegert. Magnetic resonance for nonrotating fields. *Phys. Rev.*, 57:522–527, Mar 1940.

[54] Simon Gustavsson, Olger Zwier, Jonas Bylander, Fei Yan, Fumiki Yoshihara, Yasunobu Nakamura, Terry P. Orlando, and William D. Oliver. Improving quantum gate fidelities by using a qubit to measure microwave pulse distortions. *Phys. Rev. Lett.*, 110:040502, Jan 2013.

[55] Fumiki Yoshihara, Yasunobu Nakamura, Fei Yan, Simon Gustavsson, Jonas Bylander, William D. Oliver, and Jaw-Shen Tsai. Flux qubit noise spectroscopy using rabi oscillations under strong driving conditions. *Phys. Rev. B*, 89:020503, Jan 2014.

[56] W. M. Griffith, Michael W. Noel, and T. F. Gallagher. Phase and rise-time dependence using rf pulses in multiphoton processes. *Phys. Rev. A*, 57:3698–3704, May 1998.

[57] N. Goldman and J. Dalibard. Periodically driven quantum systems: Effective hamiltonians and engineered gauge fields. *Phys. Rev. X*, 4:031027, Aug 2014.

[58] M. H. Devoret and R. J. Schoelkopf. Superconducting circuits for quantum information: An outlook. *Science*, 339(6124):1169–1174, 2013.

[59] G. G. Paulus, F. Lindner, H. Walther, A. Baltuška, E. Goulielmakis, M. Lezius, and F. Krausz. Measurement of the phase of few-cycle laser pulses. *Phys. Rev. Lett.*, 91:253004, Dec 2003.

[60] G. D. Fuchs, V. V. Dobrovitski, D. M. Toyli, F. J. Heremans, and D. D. Awschalom. Gigahertz dynamics of a strongly driven single quantum spin. *Science*, 326(5959):1520–1522, 2009.

[61] Y. Nakamura, Yu. A. Pashkin, and J. S. Tsai. Rabi oscillations in a josephson-junction charge two-level system. *Phys. Rev. Lett.*, 87:246601, Nov 2001.

[62] S. Saito, M. Thorwart, H. Tanaka, M. Ueda, H. Nakano, K. Semba, and H. Takayanagi. Multiphoton transitions in a macroscopic quantum two-state system. *Phys. Rev. Lett.*, 93:037001, Jul 2004.

[63] Mika Sillanpää, Teijo Lehtinen, Antti Paila, Yuriy Makhlin, and Pertti Hakonen. Continuous-time monitoring of landau-zener interference in a cooper-pair box. *Phys. Rev. Lett.*, 96:187002, May 2006.

[64] C. M. Wilson, T. Duty, F. Persson, M. Sandberg, G. Johansson, and P. Delsing. Coherence times of dressed states of a superconducting qubit under extreme driving. *Phys. Rev. Lett.*, 98:257003, Jun 2007.

[65] A. Izmalkov, S. H. W. van der Ploeg, S. N. Shevchenko, M. Grajcar, E. Il'ichev, U. Hübner, A. N. Omelyanchouk, and H.-G. Meyer. Consistency of ground state and spectroscopic measurements on flux qubits. *Phys. Rev. Lett.*, 101:017003, Jul 2008.

[66] Guozhu Sun, Xueda Wen, Yiwen Wang, Shanhua Cong, Jian Chen, Lin Kang, Weiwei Xu, Yang Yu, Siyuan Han, and Peiheng Wu. Population inversion induced by landauzener transition in a strongly driven rf superconducting quantum interference device. *Applied Physics Letters*, 94(10):–, 2009.

[67] M. P. Silveri, K. S. Kumar, J. Tuorila, J. Li, A. Vepsäläinen, E. V. Thuneberg, and G. S. Paraoanu. Stückelberg interference in a superconducting qubit under periodic latching modulation. *arXiv preprint arXiv:1412.3982*, dec 2014.

[68] A.V. Shytov, D.A. Ivanov, and M.V. Feigelman. Landau-zener interferometry for qubits. *The European Physical Journal B - Condensed Matter and Complex Systems*, 36(2):263–269, 2003.

[69] S. Ashhab, J. R. Johansson, A. M. Zagoskin, and Franco Nori. Two-level systems driven by large-amplitude fields. *Phys. Rev. A*, 75:063414, Jun 2007.

[70] S.N. Shevchenko, S. Ashhab, and Franco Nori. Landauzenerstckelberg interferometry. *Physics Reports*, 492(1):1 – 30, 2010.

[71] K. Drese and M. Holthaus. Floquet theory for short laser pulses. *The European Physical Journal D - Atomic, Molecular, Optical and Plasma Physics*, 5(1):119–134, 1999.

[72] J.-L. Orgiazzi, C. Deng, D. Layden, R. Marchildon, F. Kitapli, F. Shen, M. Bal, F. R. Ong, and A. Lupascu. Flux qubits in a planar circuit quantum electrodynamics architecture: quantum control and decoherence. *arXiv preprint arXiv:1407.1346*, January 2014.

[73] M. Stern, G. Catelani, Y. Kubo, C. Grezes, A. Bienfait, D. Vion, D. Esteve, and P. Bertet. Flux qubits with long coherence times for hybrid quantum circuits. *Phys. Rev. Lett.*, 113:123601, Sep 2014.

[74] C.E. Creffield. Location of crossings in the floquet spectrum of a driven two-level system. *Phys. Rev. B*, 67:165301, Apr 2003.

[75] Chunqing Deng, Jean-Luc Orgiazzi, Feiruo Shen, Sahel Ashhab, and Adrian Lupascu. Observation of floquet states in a strongly driven artificial atom. *submitted*, 2015.

[76] Milena Grifoni and Peter Hnggi. Driven quantum tunneling. *Physics Reports*, 304(56):229 – 354, 1998.

[77] M. Moskalets and M. Büttiker. Floquet scattering theory of quantum pumps. *Phys. Rev. B*, 66:205320, Nov 2002.

[78] H.P. Breuer and M. Holthaus. Adiabatic processes in the ionization of highly excited hydrogen atoms. *Zeitschrift fr Physik D Atoms, Molecules and Clusters*, 11(1):1–14, 1989.

[79] Uri Peskin and Nimrod Moiseyev. The solution of the time-dependent schrdinger equation by the (t,t) method: Theory, computational algorithm and applications. *The Journal of Chemical Physics*, 99(6):4590–4596, 1993.

[80] Gustavo Rigolin, Gerardo Ortiz, and Victor Hugo Ponce. Beyond the quantum adiabatic approximation: Adiabatic perturbation theory. *Phys. Rev. A*, 78:052508, Nov 2008.

[81] Isaac L. Chuang and M. A. Nielsen. Prescription for experimental determination of the dynamics of a quantum black box. *Journal of Modern Optics*, 44(11-12):2455–2467, 1997.

[82] J. F. Poyatos, J. I. Cirac, and P. Zoller. Complete characterization of a quantum process: The two-bit quantum gate. *Phys. Rev. Lett.*, 78:390–393, Jan 1997.

[83] Michael A. Nielsen. A simple formula for the average gate fidelity of a quantum dynamical operation. *Physics Letters A*, 303(4):249 – 252, 2002.

[84] A. R. Calderbank, E. M. Rains, P. W. Shor, and N. J. A. Sloane. Quantum error correction and orthogonal geometry. *Phys. Rev. Lett.*, 78:405–408, Jan 1997.

[85] E. M. Purcell. Proceedings of the american physical society. *Phys. Rev.*, 69:674–674, Jun 1946.

[86] D. E. Oates, A. C. Anderson, and P. M. Mankiewich. Measurement of the surface resistance of $yba_2cu_3o_{7-x}$ thin films using stripline resonators. *Journal of Superconductivity*, 3(3):251–259, 1990.

[87] J. Krupka, K. Derzakowski, M. Tobar, J. Hartnett, and R. G. Geyer. Complex permittivity of some ultralow loss dielectric crystals at cryogenic temperatures. *Measurement Science and Technology*, 10(5):387, 1999.

[88] P. K. Day, H. G. LeDuc, B. A. Mazin, A. Vayonakis, and J. Zmuidzinas. A broadband superconducting detector suitable for use in large arrays. *Nature*, 425:817–821, 2003.

[89] R. Vijay, D. H. Slichter, and I. Siddiqi. Observation of quantum jumps in a superconducting artificial atom. *Physical review letters*, 106(11):110502, 2011.

[90] C. A. Regal, J. D. Teufel, and K. W. Lehnert. Measuring nanomechanical motion with a microwave cavity interferometer. *Nature Physics*, 4(7):555–560, 2008.

[91] Hanhee Paik and Kevin D Osborn. Reducing quantum-regime dielectric loss of silicon nitride for superconducting quantum circuits. *Appl. Phys. Lett.*, 96(7):072505, January 2010.

[92] K. Geerlings, S. Shankar, E. Edwards, L. Frunzio, R. J. Schoelkopf, and M. H. Devoret. Improving the quality factor of microwave compact resonators by optimizing their geometrical parameters. *Applied Physics Letters*, 100(19):192601, 2012.

[93] A. Megrant, C. Neill, R. Barends, B. Chiaro, Yu Chen, L. Feigl, J. Kelly, Erik Lucero, Matteo Mariantoni, P. J. J. O'Malley, D. Sank, A. Vainsencher, J. Wenner, T. C. White, Y. Yin, J. Zhao, C. J. Palmstrøm, John M. Martinis, and A. N. Cleland. Planar superconducting resonators with internal quality factors above one million. *Applied Physics Letters*, 100(11):113510, 2012.

[94] A.D. O'Connell, M. Ansmann, R. C. Bialczak, M. Hofheinz, N. Katz, E. Lucero, C. McKenney, M. Neeley, H. Wang, E. M. Weig, et al. Microwave dielectric loss at single photon energies and millikelvin temperatures. *Applied Physics Letters*, 92(11):112903–112903, 2008.

[95] S. J. Weber, K. W. Murch, D. H. Slichter, R. Vijay, and I. Siddiqi. Single crystal silicon capacitors with low microwave loss in the single photon regime. *Applied Physics Letters*, 98, February 2011.

[96] Katarina Cicak, Dale Li, Joshua A Strong, Michael S Allman, Fabio Altomare, Adam J Sirois, Jed D Whittaker, John D Teufel, and Raymond W Simmonds. Low-loss superconducting resonant circuits using vacuum-gap-based microwave components. *Appl. Phys. Lett.*, 96(9):093502, January 2010.

[97] M. R. Vissers, J. Gao, D. S. Wisbey, D. A. Hite, C. C. Tsuei, A. D. Corcoles, M. Steffen, and D. P. Pappas. Low loss superconducting titanium nitride coplanar waveguide resonators. *Applied Physics Letters*, 97(23):232509–232509, 2010.

[98] P. Macha, S. H. W. van der Ploeg, G. Oelsner, E. Ilichev, H.-G. Meyer, S. Wnsch, and M. Siegel. Losses in coplanar waveguide resonators at millikelvin temperatures. *Applied Physics Letters*, 96(6):–, 2010.

[99] J. Gao, J. Zmuidzinas, B. A. Mazin, H. G. LeDuc, and P. K. Day. Noise properties of superconducting coplanar waveguide microwave resonators. *Applied Physics Letters*, 90(10):102507–102507, 2007.

[100] R. Barends, N. Vercruyssen, A. Endo, P. J. De Visser, T. Zijlstra, T. M. Klapwijk, P. Diener, S. J. C. Yates, and J. J. A. Baselmans. Minimal resonator loss for circuit quantum electrodynamics. *Applied Physics Letters*, 97(2):023508–023508, 2010.

[101] J. Zmuidzinas. Superconducting microresonators: Physics and applications. *Annu. Rev. Condens. Matter Phys.*, 3(1):169–214, 2012.

[102] D. S. Wisbey, J. Gao, M. R. Vissers, F. da Silva, J. S. Kline, L. Vale, and D. P. Pappas. Effect of metal/substrate interfaces on radio-frequency loss in superconducting coplanar waveguides. *Journal of Applied Physics*, 108(9):093918–093918, 2010.

[103] M. S. Khalil, M. J. A. Stoutimore, F. C. Wellstood, and K. D. Osborn. An analysis method for asymmetric resonator transmission applied to superconducting devices. *Journal of Applied Physics*, 111(5):054510–054510, 2012.

[104] John M. Martinis, K. B. Cooper, R. McDermott, Matthias Steffen, Markus Ansmann, K. D. Osborn, K. Cicak, Seongshik Oh, D. P. Pappas, R. W. Simmonds, and Clare C. Yu. Decoherence in josephson qubits from dielectric loss. *Phys. Rev. Lett.*, 95:210503, Nov 2005.

[105] D. Kajfez. Linear fractional curve fitting for measurement of high q factors. *Microwave Theory and Techniques, IEEE Transactions on*, 42(7):1149–1153, 1994.

[106] W. A. Phillips. Two-level states in glasses. *Reports on Progress in Physics*, 50(12):1657, 1987.

[107] W.A. Phillips, A.C. Anderson, B. Golding, J.E. Graebner, S. Hunklinger, J. Jäckle, R.O. Pohl, v Schickfus, and D.L. Weaire. *Amorphous Solids: Low-Temperature Properties*. Topics in Current Physics. Springer London, Limited, 2011.

[108] Jiansong Gao, Miguel Daal, Anastasios Vayonakis, Shwetank Kumar, Jonas Zmuidzinas, Bernard Sadoulet, Benjamin A Mazin, Peter K Day, and Henry G Leduc. Experimental evidence for a surface distribution of two-level systems in superconducting lithographed microwave resonators. *Appl. Phys. Lett.*, 92(15):152505, January 2008.

[109] R. Barends, H. L. Hortensius, T. Zijlstra, J. J. A. Baselmans, S. J. C. Yates, J. R. Gao, and T. M. Klapwijk. Contribution of dielectrics to frequency and noise of nbtin superconducting resonators. *Applied Physics Letters*, 92(22):–, 2008.

[110] Z. Kim, V. Zaretskey, Y. Yoon, J. F. Schneiderman, M. D. Shaw, P. M. Echternach, F. C. Wellstood, and B. S. Palmer. Anomalous avoided level crossings in a cooper-pair box spectrum. *Phys. Rev. B*, 78:144506, Oct 2008.

[111] A. Lupaşcu, P. Bertet, E. F. C. Driessen, C. J. P. M. Harmans, and J. E. Mooij. One- and two-photon spectroscopy of a flux qubit coupled to a microscopic defect. *Phys. Rev. B*, 80:172506, Nov 2009.

[112] David P. Pappas, Michael R. Vissers, David S. Wisbey, Jeffrey S. Kline, and Jiansong Gao. Two level system loss in superconducting microwave resonators. *Applied Superconductivity, IEEE Transactions on*, 21(3):871–874, 2011.

[113] Cornelis Pieter Heij. *Single - charge transport in coupled nanostructures*. PhD thesis, Delft University of Technology, 2001.

[114] M. Hatridge, R. Vijay, D. H. Slichter, John Clarke, and I. Siddiqi. Dispersive magnetometry with a quantum limited squid parametric amplifier. *Phys. Rev. B*, 83:134501, Apr 2011.

[115] Chunqing Deng, Martin Otto, and Adrian Lupascu. An analysis method for transmission measurements of superconducting resonators with applications to quantum-regime dielectric-loss measurements. *Journal of Applied Physics*, 114(5):054504, 2013.

[116] Brian R. Strohmeier. An esca method for determining the oxide thickness on aluminum alloys. *Surface and Interface Analysis*, 15(1):51–56, 1990.

[117] Abdufarrukh A. Abdumalikov, Oleg Astafiev, Yasunobu Nakamura, Yuri A. Pashkin, and JawShen Tsai. Vacuum Rabi splitting due to strong coupling of a flux qubit and a coplanar-waveguide resonator. *Phys. Rev. B*, 78:180502, Nov 2008.

[118] K. Inomata, T. Yamamoto, P.-M. Billangeon, Y. Nakamura, and J. S. Tsai. Large dispersive shift of cavity resonance induced by a superconducting flux qubit in the straddling regime. *Phys. Rev. B*, 86:140508, Oct 2012.

[119] M. Jerger, S. Poletto, P. Macha, U. Hbner, E. Ilichev, and A. V. Ustinov. Frequency division multiplexing readout and simultaneous manipulation of an array of flux qubits. *Applied Physics Letters*, 101(4):–, 2012.

[120] A. P. Sears, A. Petrenko, G. Catelani, L. Sun, Hanhee Paik, G. Kirchmair, L. Frunzio, L. I. Glazman, S. M. Girvin, and R. J. Schoelkopf. Photon shot noise dephasing in the strong-dispersive limit of circuit qed. *Phys. Rev. B*, 86:180504, Nov 2012.

[121] D. I. Schuster, A. A. Houck, J. A. Schreier, A. Wallraff, J. M. Gambetta, A. Blais, L. Frunzio, J. Majer, B. Johnson, M. H. Devoret, S. M. Girvin, and R. J. Schoelkopf. Resolving photon number states in a superconducting circuit. *Nature*, 445(7127):515–518, February 2007.

[122] Y. Yuzhelevski, M. Yuzhelevski, and G. Jung. Random telegraph noise analysis in time domain. *Review of Scientific Instruments*, 71(4):1681–1688, 2000.

[123] S. Meiboom and D. Gill. Modified spin-echo method for measuring nuclear relaxation times. *Review of Scientific Instruments*, 29(8):688–691, 1958.

[124] Daniel Sank, R. Barends, Radoslaw C. Bialczak, Yu Chen, J. Kelly, M. Lenander, E. Lucero, Matteo Mariantoni, A. Megrant, M. Neeley, P. J. J. O'Malley, A. Vainsencher, H. Wang, J. Wenner, T. C. White, T. Yamamoto, Yi Yin, A. N. Cleland, and John M. Martinis. Flux noise probed with real time qubit tomography in a josephson phase qubit. *Phys. Rev. Lett.*, 109:067001, Aug 2012.

[125] D. H. Slichter, R. Vijay, S. J. Weber, S. Boutin, M. Boissonneault, J. M. Gambetta, A. Blais, and I. Siddiqi. Measurement-induced qubit state mixing in circuit qed from up-converted dephasing noise. *Phys. Rev. Lett.*, 109:153601, Oct 2012.

[126] Fei Yan, Jonas Bylander, Simon Gustavsson, Fumiki Yoshihara, Khalil Harrabi, David G. Cory, Terry P. Orlando, Yasunobu Nakamura, Jaw-Shen Tsai, and William D. Oliver. Spectroscopy of low-frequency noise and its temperature dependence in a superconducting qubit. *Phys. Rev. B*, 85:174521, May 2012.

[127] O. Astafiev, Yu. A. Pashkin, Y. Nakamura, T. Yamamoto, and J. S. Tsai. Quantum noise in the josephson charge qubit. *Phys. Rev. Lett.*, 93:267007, Dec 2004.

[128] Neil M. Zimmerman and William H. Huber. Microscope of glassy relaxation in femtogram samples: Charge offset drift in the single electron transistor. *Phys. Rev. B*, 80:195304, Nov 2009.

[129] F. C. Wellstood, C. Urbina, and John Clarke. Flicker (1/f) noise in the critical current of josephson junctions at 0.094.2k. *Applied Physics Letters*, 85(22):5296–5298, 2004.

[130] D. J. Van Harlingen, T. L. Robertson, B. L. T. Plourde, P. A. Reichardt, T. A. Crane, and John Clarke. Decoherence in josephson-junction qubits due to critical-current fluctuations. *Phys. Rev. B*, 70:064517, Aug 2004.

[131] Michael Muck, Matthias Korn, C. G. A. Mugford, J. B. Kycia, and John Clarke. Measurements of 1/f noise in josephson junctions at zero voltage: Implications for decoherence in superconducting quantum bits. *Applied Physics Letters*, 86(1):–, 2005.

[132] J. Eroms, L. C. van Schaarenburg, E. F. C. Driessen, J. H. Plantenberg, C. M. Huizinga, R. N. Schouten, A. H. Verbruggen, C. J. P. M. Harmans, and J. E. Mooij. Low-frequency noise in josephson junctions for superconducting qubits. *Applied Physics Letters*, 89(12):–, 2006.

[133] F. Yoshihara, K. Harrabi, A. O. Niskanen, Y. Nakamura, and J. S. Tsai. Decoherence of flux qubits due to $1/f$ flux noise. *Phys. Rev. Lett.*, 97:167001, Oct 2006.

[134] Radoslaw C. Bialczak, R. McDermott, M. Ansmann, M. Hofheinz, N. Katz, Erik Lucero, Matthew Neeley, A. D. O'Connell, H. Wang, A. N. Cleland, and John M. Martinis. $1/f$ flux noise in josephson phase qubits. *Phys. Rev. Lett.*, 99:187006, Nov 2007.

[135] Frederick C. Wellstood, Cristian Urbina, and John Clarke. Low-frequency noise in dc superconducting quantum interference devices below 1 k. *Applied Physics Letters*, 50(12):772–774, 1987.

[136] S. M. Anton, J. S. Birenbaum, S. R. O'Kelley, V. Bolkhovsky, D. A. Braje, G. Fitch, M. Neeley, G. C. Hilton, H.-M. Cho, K. D. Irwin, F. C. Wellstood, W. D. Oliver, A. Shnirman, and John Clarke. Magnetic flux noise in dc squids: Temperature and geometry dependence. *Phys. Rev. Lett.*, 110:147002, Apr 2013.

[137] A. A. Houck, J. A. Schreier, B. R. Johnson, J. M. Chow, Jens Koch, J. M. Gambetta, D. I. Schuster, L. Frunzio, M. H. Devoret, S. M. Girvin, and R. J. Schoelkopf. Controlling the spontaneous emission of a superconducting transmon qubit. *Phys. Rev. Lett.*, 101:080502, Aug 2008.

[138] John M. Martinis, M. Ansmann, and J. Aumentado. Energy decay in superconducting josephson-junction qubits from nonequilibrium quasiparticle excitations. *Phys. Rev. Lett.*, 103:097002, Aug 2009.

[139] G. Catelani, J. Koch, L. Frunzio, R. J. Schoelkopf, M. H. Devoret, and L. I. Glazman. Quasiparticle relaxation of superconducting qubits in the presence of flux. *Phys. Rev. Lett.*, 106:077002, Feb 2011.

[140] G. Catelani, R. J. Schoelkopf, M. H. Devoret, and L. I. Glazman. Relaxation and frequency shifts induced by quasiparticles in superconducting qubits. *Phys. Rev. B*, 84:064517, Aug 2011.

[141] D. Ristè, C. C. Bultink, M. J. Tiggelman, R. N. Schouten, K. W. Lehnert, and L. DiCarlo. Millisecond charge-parity fluctuations and induced decoherence in a superconducting transmon qubit. *Nature communications*, 4:1913, 2013.

[142] M. Bal, M. H. Ansari, J.-L. Orgiazzi, R. M. Lutchyn, and A. Lupascu. Dynamics of parametric fluctuations induced by quasiparticle tunneling in superconducting flux qubits. *Phys. Rev. B*, 91:195434, May 2015.

[143] Bradley Efron and R.J. Tibshirani. *An Introduction to the Bootstrap (Chapman & Hall/CRC Monographs on Statistics & Applied Probability)*. Chapman and Hall/CRC, 5 1994.

[144] Fei Yan. *Coherence characterization with a superconducting flux qubit through NMR approaches*. PhD thesis, Massachusetts Institute of Technology, 2013.